# Wake Geometry Measurements and Analytical Calculations on a Small-Scale Rotor Model

*Terence A. Ghee, John D. Berry, Laith A. J. Zori, and Joe W. Elliott*

# Wake Geometry Measurements and Analytical Calculations on a Small-Scale Rotor Model

*Terence A. Ghee*
*Analytical Services & Materials, Inc.* • *Hampton, Virginia*

*John D. Berry*
*Joint Research Program Office*
*Aeroflightdynamics Directorate*
*U.S. Army Aviation and Troop Command*
*Langley Research Center* • *Hampton, Virginia*

*Laith A. J. Zori*
*Iowa State University* • *Ames, Iowa*

*Joe W. Elliott*
*Joint Research Program Office*
*Aeroflightdynamics Directorate*
*U.S. Army Aviation and Troop Command*
*Langley Research Center* • *Hampton, Virginia*

August 1996

The use of trademarks or names of manufacturers in this report is for accurate reporting and does not constitute an official endorsement, either expressed or implied, of such products or manufacturers by the National Aeronautics and Space Administration or the U.S. Army.

# Abstract

*An experimental investigation was conducted in the Langley 14- by 22-Foot Subsonic Tunnel to quantify the rotor wake behind a scale model helicopter rotor in forward level flight at one thrust level. The rotor system in this test consisted of a four-bladed fully articulated hub with blades of rectangular planform and an NACA 0012 airfoil section. A laser light sheet, seeded with propylene glycol smoke, was used to visualize the vortex geometry in the flow in planes parallel and perpendicular to the free-stream flow. Quantitative measurements of wake geometric properties, such as vortex location, vertical skew angle, and vortex particle void radius, were obtained as well as convective velocities for blade tip vortices. Comparisons were made between experimental data and four computational method predictions of experimental tip vortex locations, vortex vertical skew angles, and wake geometries. The results of these comparisons highlight difficulties of accurate wake geometry predictions.*

## Introduction

The rotor wake geometry is affected by various rotor flight parameters (e.g., tip-path plane (TPP) angle of attack, thrust, and advance ratio) and blade characteristics (e.g., twist, number of blades, and planform). The effects of the rotor wake are recognized as paramount to accurate prediction of rotor loads and, hence, overall rotor performance. (See ref. 1.) For this reason, accuracy of rotor wake geometric models and validation of these models with experimental data are important.

The wake of a helicopter rotor in forward flight consists of sheets of vorticity that are shed from the rotor blades and roll up at the outboard edge into strong tip vortices. A cycloidal pattern is formed by these tip vortices as the blades move forward. This pattern of tip vortices rolls up behind the rotor into a pair of apparent far-field disk vortices. These apparent disk vortices appear to an observer situated in the far field like the wingtip vortices created by a fixed-wing aircraft. These flow features are not true vortices but are tight spiraling of the tip vortices. Another feature of the wake is the roll-up of the outer edge of the vortex sheet trailing from the rotor blade into a discrete vortex that rotates in the opposite sense of the tip vortex.

Early rotor performance models were developed for propellers and used blade element theory or momentum theory methods. (See ref. 2.) However, accurate blade load calculations necessitated more refined methods that also modeled the rotor wake geometry. Reference 1 extensively catalogs early rotor performance models.

Since the advent of the digital computer, empirical results from studies that characterized the rotor wake geometry were joined with predictions by the Biot-Savart law. (See refs. 3–6.) Such prescribed wake computational methods are efficient, but the effect of small-scale rotor wake geometry data to characterize the wake distortion on a full-scale vehicle has not been fully determined.

Free-wake models provide a more sophisticated and computationally intensive method to predict the rotor wake geometry. (See refs. 7–10.) A force-free condition is imposed on the vortex position, and the wake geometry is solved iteratively rather than determined from empirical data.

More recently, Navier-Stokes methods (e.g., refs. 11 and 12) have been used to model the rotor flow field. These models have the advantage of accounting for the wake in the governing fluid flow equations and developing the wake as part of the solution without having to model the near or far wake. However, the wake diffuses quickly as it is convected through coarse mesh regions. These methods are also computationally very expensive.

Regardless of the model used, a correlation with experimental wake geometry data must be performed to validate the computational results. Unfortunately, these experimental data are rather sparse.

Experimental determination of the rotor wake geometry is difficult, especially in forward flight. In principle, methods such as laser Doppler velocimetry (LDV) and hot-wire anemometry are able to define the rotor flow field completely but require large numbers of data points, which fact translates into a massive block of testing time. These methods are best suited to a limited study (refs. 13 and 14) or to studies with known flow field structures (ref. 15).

In the past, flow visualization techniques have been used to qualify and quantify the rotor wake geometry. Various flow visualization techniques and their uses are discussed in reference 16. Rotor wake flow visualization has been used with success in wind and water tunnel tests and flight tests. (See refs. 17–22.)

Wind tunnel research to visualize the rotor wake can be divided into two main groups: optical methods and smoke or particle injection methods. Optical methods include Schlieren and shadowgraph techniques as

described in references 23–28. Smoke injection, which is a classic technique, has been shown recently to be very effective when used in conjunction with a laser light sheet. (See refs. 29–31.) A laser is used to create a thin sheet of light that can be located in the rotor wake to view phenomena occurring in that plane of light. Smoke particles are typically injected upstream of the laser light sheet to illuminate the flow and allow significant wake structures to become visible at a known location.

For this study, the wake of the rotor system was assumed to be periodic with blade passage. All data that were taken were used to define the motion of the rotor wake system during only 90° of blade rotation for a specific flight condition. This assumption ignored blade-to-blade differences and the effect of unsteady onset flow to the rotor. These effects were assessed during this investigation.

In this study, a laser light sheet was used to visualize and quantify the wake geometry of a small-scale rotor for comparison with theoretical calculations. The position of tip vortices and the general wake structure were compared with the predictions of four computational methods. The rotor wake vortex structure was illuminated in four longitudinal planes and seven lateral planes at two forward speeds.

Illumination of the wake longitudinally allowed the tip vortices to be observed in a known plane. From these observations the following phenomena were documented: tip vortex and inboard sheet roll-up location, tip vortex vertical skew angle $\alpha_v$, vortex convective velocity, and vortex particle void radius. The vortex vertical skew angle is defined as the angle between the vortex wake and the free-stream velocity. (Positive vertical skew angle is in the direction of positive fuselage rotation, which is nose up.) The convective velocity is defined as the velocity at which the tip vortices convect downstream in the laser light sheet plane. The particle void radius is defined as the radius of the dark center of a vortex. This dark center is essentially void of smoke particles. The experimental tip vortex location and vertical skew angle are compared with three analytical predictions: a relatively simple wake analysis, a free-wake analysis, and an analysis that accounts for effects of the fuselage.

The laser light sheet was positioned laterally across the wake to allow the roll-up of the tip vortices into an apparent disk vortex to become visible. The location of the apparent disk vortex, the vertical trajectory $\alpha_t$, and the lateral contraction angle $\alpha_l$ are presented. The vertical trajectory is defined as the angle between the apparent disk vortex wake and the horizontal plane. The horizontal contraction angle is the angle between the apparent disk vortex wake and a longitudinal line down the wind

tunnel (as seen from above). The location of the apparent disk vortex and the angles of vertical trajectory and lateral contraction are compared with predictions from a Navier-Stokes computer code.

## Symbols

| | |
|---|---|
| $A$ | area of rotor disk, $\pi R^2$, 25.04 ft$^2$ |
| $a_0$ | coning angle, deg |
| $b$ | number of blades (4) |
| $C_T$ | rotor thrust coefficient, $\dfrac{T}{\rho\pi\Omega^2 R^4} = 0.0064$ |
| CW | vortex that appears to observer to rotate clockwise |
| CCW | vortex that appears to observer to rotate counterclockwise |
| $c$ | blade chord, 0.2175 ft |
| ISV | inboard sheet vortex |
| $R$ | rotor radius, 2.8233 ft |
| RWF | rotor-wake fuselage |
| $r$ | radial location, ft |
| $r_v$ | particle void size, ft |
| $\Delta r_v$ | uncertainty in particle void size measurement, in. |
| $S$ | resultant length, ft |
| $\Delta S$ | resultant uncertainty in length, ft |
| $T$ | rotor thrust, 148 lb |
| $t$ | time, sec |
| $\Delta t$ | total uncertainty in $t$, sec |
| $u$ | component of velocity in $x$ direction, ft/sec |
| upper | tip vortex that rolls up and over apparent disk vortex |
| $V$ | velocity, ft/sec |
| $\Delta V$ | total uncertainty in velocity, ft/sec |
| $V_\infty$ | free-stream velocity, ft/sec |
| $V/V_\infty$ | ratio of speeds |
| $w$ | component of velocity in $z$ direction, ft/sec |
| $x, y, z$ | coordinate system hub center, (0,0,0), ft |
| $x_{measure}$ | one-half pixel uncertainty in particle void size measurement, in. |
| $x_{min}$ | limiting minimum uncertainty in $x$, in. |
| $x_{subject}$ | subjectivity error in $x$, in. |
| $\Delta x$ | total uncertainty in $x$, in. |

$\Delta x_{grid}$    uncertainty in measuring $x$ dimension for reference grid, in.

$\Delta x_{member}$    uncertainty in measuring $x$ dimension for reference grid members, in.

$\Delta x_{pitch}$    uncertainty in measuring $x$ dimension for reference grid angularity, in.

$y_{min}$    limiting minimum uncertainty in $y$, in.

$y_{subject}$    subjectivity error in $y$, in.

$\Delta y$    total uncertainty in $y$, in.

$\Delta y_{grid}$    uncertainty in measuring $y$ dimension for reference grid, in.

$\Delta y_{member}$    uncertainty in measuring $y$ dimension for reference grid members, in.

$\Delta y_{pitch}$    uncertainty in measuring $y$ dimension for reference grid angularity, in.

$z_{min}$    limiting minimum uncertainty in $z$, in.

$z_{subject}$    subjectivity error in $z$, in.

$\Delta z$    total uncertainty in $z$, in.

$\Delta z_{grid}$    uncertainty in measuring $z$ dimension for reference grid, in.

$\Delta z_{member}$    uncertainty in measuring $z$ dimension for reference grid members, in.

$\Delta z_{pitch}$    uncertainty in measuring $z$ dimension for reference grid angularity, in.

$\alpha_l$    disk vortex lateral contraction angle,
$$\tan^{-1}\left(\frac{y/R}{x/R}\right), \text{deg}$$

$\alpha_s$    shaft angle of attack (positive nose up), deg

$\alpha_t$    disk vortex vertical trajectory angle,
$$\tan^{-1}\left(\frac{z/R}{x/R}\right), \text{deg}$$

$\alpha_{TPP}$    tip-path plane angle of attack (positive nose up), deg

$\alpha_v$    vortex vertical skew angle, $\tan^{-1}\left(\frac{z/R}{x/R}\right)$, deg

$\alpha_w$    momentum wake angle, $-(\chi_{TPP} - \alpha_{TPP})$, deg

$\mu$    advance ratio, $\dfrac{V_\infty \cos\alpha_{TPP}}{\Omega R}$

$\rho$    density of free-stream flow, slug/ft$^3$

$\sigma$    rotor solidity, $\dfrac{bc}{\pi R}$

$\chi_{TPP}$    wake deflection angle,
$$\tan^{-1}\left[\tan(-\alpha_{TPP}) + \frac{C_T}{2\mu^2}\right], \text{deg}$$

$\psi_b$    blade azimuth angle (0° over tail), deg

$\psi_w$    wake azimuth age (0° over tail), deg

$\Omega$    rotor rotational frequency, rad/sec

2MRTS    2-meter rotor test system

## Description of Experiment

### Test Apparatus

The experiments were performed in the Langley 14- by 22-Foot Subsonic Tunnel shown in figure 1. The 14- by 22-Foot Subsonic Tunnel is a closed-circuit low-speed wind tunnel designed for tests of vertical or short takeoff and landing (V/STOL) models. (See ref. 32.) A novel feature of this facility is the ability to operate as an open test section with the walls and ceiling lifted out of the flow. For this study, the wind tunnel was run as an open test section to allow maximum optical access to the rotor wake. The wind tunnel features a smoke–laser-velocimetry-seeding traversing rig that is mounted in the settling chamber of the wind tunnel 90 ft upstream of the test section. The traversing rig position is remotely controlled to seed any portion of the test section. The smoke generator in this investigation used vaporized propylene glycol that was heated to approximately 350° to 400°F. The vaporized liquid is sent through 65 ft of heated hose and ejected out of a crude nozzle. Air pressure was used to adjust the flow rate and smoke quality.

The 2-meter rotor test system (2MRTS) is a general-purpose rotor-model-testing system, which was mounted on a vertical strut in the forward portion of the test section. The rotor was powered by a 29-hp electric motor with a two-stage 90° transmission using a 4:1 gear reduction ratio. Details of this rotor test system are given in reference 33. The rotor hub was fully articulated with coincident flap and lead-lag hinges that employed viscous dampers to dampen blade lag motion. A 33.88-in-radius, four-bladed, articulated rotor system was used. (The rotor disk area $A = 25.04$ ft$^2$.) The rotor blades had a rectangular planform and an NACA 0012 airfoil section with a chord of 2.6 in. and linear twist of $-8°$ (nose down). Note that the rotor blades were very stiff torsionally when compared with a full-scale rotor system. Rotor trim and attitude were set with a blade pitch remote control system. The rotor system mounted in the wind tunnel is shown in figure 2.

A generic fuselage shell that can be parameterized with easily defined coordinates enclosed the helicopter drive and control system. The geometry of the shell

3

consisted of a slender main body with a slender nacelle about the rotor shaft. (See ref. 34.) The rotor and fuselage were each mounted on a six-component strain-gage balance to measure rotor and fuselage forces and moments independently. One blade was instrumented with strain gages to monitor blade loads for safety of flight considerations. Potentiometers were used to measure blade flapping and lead-lag motion, and a digital encoder (1024 counts per revolution) was attached to the rotor shaft to monitor rotor speed in rpm. The encoder also provided an azimuthal reference and was used to strobe the laser light sheet.

## Flow Visualization System

In this study, a laser light sheet system was combined with injected smoke to visualize the flow. The system employed a 15-W argon ion laser from which a 6-W beam (in all spectral lines) was directed through a Bragg cell (acoustic-optical modulator) to allow on-off control. The beam was then expanded through a cylindrical lens to create a sheet of light. The laser light sheet was in the shape of a fan with the origin at the cylindrical lens. The flow structure was discerned with vaporized propylene glycol smoke seeding the area of interest; the smoke was injected in the settling chamber of the wind tunnel at a distance of approximately 90 ft from the wind tunnel test section. The propylene glycol smoke scattered the laser light striking it and, thereby, illuminated any flow structures in the light sheet.

The laser light sheet was operated in two modes: a vertical light sheet oriented perpendicularly to the free stream (i.e., lateral light sheet) and operated as a continuous light sheet, and a vertical light sheet oriented parallel to the free stream (i.e., longitudinal light sheet) and operated as a strobed light sheet. The lateral light sheet was used to visualize the roll-up of the tip vortices into apparent disk vortices. Because the laser was not strobed, a time-averaged view of the wake cross section was obtained. The longitudinal light sheet was used to visualize the instantaneous position of the tip vortices.

For the strobed longitudinal laser light sheet shown in figure 3, the signal from the rotor shaft encoder was used to trigger the Bragg cell, which provided an instantaneous view of the tip vortex wake. When the trigger signal was received from the rotor shaft encoder, the Bragg cell shifted the laser beam. The shifted laser beam then passed through to the cylindrical lens to create the light sheet.

A trigger-generating circuit was used to vary the strobe duration, number of rotor blades, and phase delay of the trigger. The laser light sheet, which was pulsed by the Bragg cell, was triggered so that the rotor and the individual blade tip vortices appeared stationary. The

trigger could be adjusted in increments of 11.25° of blade azimuth. Because a four-bladed rotor system was used, the wake geometry and blade positions repeat every 90°. Thus, by adjustment of the trigger to sweep a reference blade through a 90° arc, the entire wake geometry was captured. In addition, the trigger circuitry had the ability to slip-synchronize the rotor phase, which allowed the rotor blades to appear to rotate slowly. See reference 30 for details of the laser light sheet hardware and operation.

For the longitudinal light sheet tests, charge-coupled-device (CCD) video cameras were positioned on either side of the wind tunnel test section. (See fig. 3.) The video cameras were positioned at angles to the laser light sheet to receive the greatest amount of forward scattered light. Cameras positioned orthogonally to the laser light sheet would have made it easier to analyze the data (less image warping); however, the nature of laser light required that the cameras be positioned at an angle to the light sheet for best results.

For the lateral light sheet shown in figure 4, the laser beam was passed continuously through the Bragg cell, and, thus, the light sheet did not strobe. A CCD camera was positioned downstream and to the left of the model in one of two locations that depended on laser light sheet location.

For both laser light sheet planes, the light sheet was estimated to be 1/8 to 1/4 in. thick. The thickness of the laser light sheet in the measurement area varied with light sheet location and was not measured.

## Test Procedure

Tests were conducted at advance ratios of 0.15 and 0.23 (level flight) and at one thrust level ($C_T = 0.0064$). The shaft angle of attack was maintained at $-3°$ for both advance ratios with zero flapping of the blades relative to the shaft.

The laser light sheet was oriented perpendicular (laterally) to the flow at $x/R$ of 1.0 to 4.0 in increments of $0.5R$, which allowed visualization of the rolled-up coalesced disk vortex. Before a run, the laser light sheet was set up in the desired plane as a continuous beam. The rotor system and wind tunnel were stabilized at an advance ratio of 0.15 and proper test conditions. Smoke was injected into and traversed across the test section until entrained in one of the apparent disk vortices. The video camera was adjusted for pan-tilt, focus, and zoom settings, and videotape data were recorded with a U-Matic (3/4-in.) videotape recorder (VTR) for approximately 20 sec. The smoke was then traversed to the opposite side of the rotor until entrained in the other apparent disk vortex. Camera settings were not adjusted between recordings. Following data acquisition, the

4

advance ratio was increased to 0.23, and the previous procedure repeated. Again, camera settings were not changed between recordings.

After the videotape data were acquired, the wind tunnel was shut down, and a reference grid was placed in the plane of the laser light sheet. The reference grid was composed of a series of 4- by 4-in. squares. A reference point was identified on this grid, and a videotape image was acquired. The camera settings were kept identical for both the data and reference images. The laser light sheet was then adjusted to the next light sheet plane, and the whole process repeated.

The laser light sheet was also oriented parallel (longitudinally) to the flow and strobed to visualize the blade tip vortices at four light sheet planes located at $y/R = \pm 0.3$ and $\pm 0.8$. The data acquisition procedure was similar to that described previously but with the addition of a strobed laser light sheet. The laser light sheet was strobed so that it was in phase with blade number 1 at a blade azimuth of $0°$. The strobe fired four times per revolution so that the four blades (and the tip vortices generated from each blade) appeared stationary. Video-tape data were recorded with a U-Matic (3/4-in.) video-tape recorder (VTR) for approximately 20 sec. The phase of the strobed light was then increased to $11.25°$. That is, the laser light sheet was triggered when blade 1 reached a blade azimuth of $11.25°$. Videotape data were again collected, and the phase of the strobed light was again adjusted in increments of $11.25°$ until the reference blade had swept a total of $90°$. The advance ratio was increased to 0.23, and the whole process, was repeated. During this process, the camera settings were not changed.

After the videotape data were acquired, the wind tunnel was shut down, and the reference grid was placed in the plane of the laser light sheet. A reference point was identified on this grid, and a videotape image was acquired. The camera settings were kept identical for both the data and reference images. The laser light sheet was then adjusted to the next light sheet plane, and the whole process repeated.

### Data Processing

After the videotape data were recorded onto 3/4-in. tape, the data were transferred onto Betacam SP tape for compatibility with the computer digitizing hardware and software. Because the Betacam SP format is approximately double the resolution of the 3/4-in. format, data degradation is minimal.

Next, the videotape was visually inspected, and useful data were selected for digitization. The image of interest, 486 pixels high by 646 pixels wide, was digitized and stored on the hard disk of the computer work-station. The image was then converted to grey scale and finally into binary format.

A special software package was used that allowed the digitized images to be stacked in a virtual volume of data. A reference grid image was also digitized and placed in the virtual volume, which allowed a one-to-one mapping of the pixel coordinates of the reference grid image to the data image. The process is similar to super-imposition of images on each other. Figure 5 shows the reference grid image superimposed on the data image. To bring out salient features not seen on the original images, the data were enhanced by traditional image-processing techniques, i.e., contrast stretching, pseudo-coloring, filtering, and contouring. For an overview of these techniques, see references 35 and 36. The center of a vortex could be identified by a mark at the pixel location, and that pixel location corresponded to the reference point on the reference grid image. The pixel values, after correction for geometric warping, were then converted into units of measure and referenced to the rotor hub center. All vortex data presented in this paper are in the wind axis system as shown in figures 3 and 4.

The vortex particle void radius was obtained in a similar manner. After digitization, the diameter of the area in the center of a vortex void of particles was measured. The particle void diameter was only measured horizontally. A tool that magnified the area of interest proved to be of great benefit in the data analysis. The particle void diameter measurement was divided by 2 to determine the particle void radius and then converted to units of measure.

As mentioned previously, strobed laser light sheet provided the ability to freeze the blades in increments of $11.25°$ of blade azimuth. Thus, the tip vortices could be traced downstream both from incrementalization of the strobe trigger in steps of $11.25°$ and from plots of the analyzed vortex position data in order of ascending wake age. The convective velocity of a vortex in the plane of the laser light sheet was determined by calculation of the distance traversed over an azimuthal increment. The time for the vortex to translate this distance was determined from the change in rotor azimuth between the two vortices and the rotor speed in rpm. These calculations assumed that the rotor wake was periodic, an assumption confirmed in subsequent analysis of the videotape data.

The inboard sheet vortex is difficult to view at real-time videotape speeds and is not always visible in every image. During the data analysis, a technique was developed that allowed the videotape images (run at full speed or frame by frame prior to digitization) to be super-imposed on the reference grid image and displayed on an adjacent monitor. This technique of live videotape image blending improved productivity in analysis of the

videotape data. The superposition of the two screens could be blended so that all, none, or part of the reference grid image could be seen. A Betacam SP VTR (used to eliminate frame jitter) was then run in slow motion and/or frame by frame for the analysis just described. This technique proved essential in the analysis of the roll-up of the inboard trailing vortex sheet.

The analysis of the tip vortex and inboard sheet roll-up data was conducted with a single frame to determine location of these features. The wake was frozen for analysis by a strobed laser light sheet with the assumption that the wake was periodic and steady in space and that the effects of video camera vibration were negligible. Analysis of the data proved this to be true for the longitudinal laser light sheet portion of the test. For the apparent disk vortex data, when viewed in the lateral laser light sheet, the effects of video camera vibration were not negligible, and a statistical approach to the data analysis was undertaken.

The position of the video camera to view the apparent disk vortex, when illuminated by a lateral laser light sheet, was in an area of increased wind-induced vibration. At long focal lengths, this amount of vibration proved too significant to rely on a single videotape frame to quantify the wake. The apparent disk vortex data were quantified by analysis of 30 frames of videotape for each location. The technique of live videotape image blending, run frame by frame, was used to obtain pixel values for the apparent disk vortex. The pixel locations were averaged to obtain the mean and standard deviation and then converted to engineering units.

**Uncertainty Estimates**

An analysis was conducted to determine the data uncertainty. The analysis addressed the uncertainty of only wake data measurements; the accuracies of the rotor system and wind tunnel were neglected. Therefore, the accuracy of the physical wake in space was assumed; only the uncertainty to measure that given wake in space was accounted for.

The measurement uncertainty for the physical location of the reference grid was estimated to be ±0.25 in., angular uncertainty was estimated to be ±0.1° in pitch (because the grid was aligned with the laser as a reference), and roll and yaw angular uncertainties were neglected. The grid members (composed of taut lines) had an uncertainty of ±0.125 in.

The measurement of a known point on the image was analyzed statistically to determine the standard deviation of that measurement. This analysis was conducted for two grid locations. Both locations had a standard deviation of approximately ±0.3 pixel. The uncertainty

was defined as the limiting minimum uncertainty for this test and is given in table 1. Because of optical skewing of the image (the video camera not being orthogonal to the laser light sheet plane), this minimum uncertainty varies with pixel location. Intrinsic in the uncertainty estimate are such variables as video camera focal length, zoom, and pantilt. Quantification of flow visualization data requires some subjectivity. To locate the center of a well-defined vortex (i.e., where a particle void was clearly visible) was the least subjective. A statistical analysis of three different configurations was conducted to quantify the subjectivity error. Thirty images of one vortex from a configuration with well-defined vortices ($y/R = -0.8$, $\mu = 0.15$, and the vortex located at $x/R \approx -0.4$ and $z/R \approx 0.02$) were analyzed to determine the standard deviation. The standard deviation of the center of a well-defined tip vortex was determined to be ±0.78 pixel for $x$ and ±0.85 pixel for $z$ and represented the minimum subjectivity error found in table 2. This exercise also confirmed the assumption that the rotor wake is periodic.

A configuration was chosen where the vortices were not easily visualized ($y/R = 0.8$, $\mu = 0.23$, and the vortex located at $x/R \approx 2.0$ and $z/R \approx -0.09$). Thirty images were analyzed for one vortex and yielded standard deviations of ±2.17 pixels for $x$ and ±1.22 pixels for $z$ that represent the maximum subjectivity error found in table 2.

In some instances (where the tip vortices rolled up and around the apparent disk vortex), only a portion of the tip vortex was visible (viewed as a series of troughs and crests). A statistical analysis of 30 images of 1 vortex was conducted for the configuration $y/R = -0.8$, $\mu = 0.15$, and the vortex located at $x/R \approx 1.1$ and $z/R \approx 0.19$. The upper tip vortex data in table 2 were computed with subjectivity errors based upon standard deviations of ±1.25 pixels for $x$ and ±1.02 pixels for $z$.

The total uncertainty is given by

$$\Delta x = [(\Delta x_{grid})^2 + (\Delta x_{member})^2 + (\Delta x_{pitch})^2$$
$$+ (x_{min})^2 + (x_{subject})^2]^{1/2} \tag{1}$$

$$\Delta y = [(\Delta y_{grid})^2 + (\Delta y_{member})^2 + (\Delta y_{pitch})^2$$
$$+ (y_{min})^2 + (y_{subject})^2]^{1/2} \tag{2}$$

$$\Delta z = [(\Delta z_{grid})^2 + (\Delta z_{member})^2 + (\Delta z_{pitch})^2$$
$$+ (z_{min})^2 + (z_{subject})^2]^{1/2} \tag{3}$$

Table 3 presents the total uncertainty in the location of the center of the tip vortices and trailed vortex sheet roll-up data. The measurement uncertainty associated with the finite duration of the strobed longitudinal laser light sheet was neglected.

As noted previously, a statistical analysis was conducted for the location of the apparent disk vortex. This approach allowed the uncertainty of video camera vibration and the subjectivity of the researcher to be quantified as the standard deviation to the mean apparent disk vortex location. Table 4 presents the total uncertainty in the location of the center of the apparent disk vortices based on the standard deviation of the mean location and the measurement uncertainty of grid placement and grid member location. The uncertainty associated with the measurement of the particle void radius was estimated to be 1.0 pixel for the particle void diameter and 0.5 pixel for the particle void radius. (See table 5.) In addition, the uncertainty associated with the grid members needs to be considered. Thus the total measurement uncertainty for the particle void measurement is given by

$$\Delta r_v = [(\Delta x_{member})^2 + (x_{measure})^2]^{1/2} \qquad (4)$$

The total uncertainty for particle void size measurement is shown in table 6. Subjectivity error was negligible for this measurement. The measurement uncertainty associated with the finite duration of the strobed laser light sheet was neglected.

The uncertainty in the convective velocity measurements used the total uncertainty in $x$, $z$, and $t$ and computed the convective velocity error based on the method outlined in reference 37 as

$$\Delta V = \left[\left(\frac{\Delta S}{t}\right)^2 + (V_\infty)^2\left(\frac{\Delta t}{t}\right)^2\right]^{1/2} \qquad (5)$$

where $\Delta S$, which is the resultant of the maximum total uncertainty in $x$ and $z$, is defined as

$$\Delta S = (\Delta x^2 + \Delta z^2)^{1/2} \qquad (6)$$

and $t$ is the total wake age divided by rotor rotational frequency

$$t = \frac{\pi \psi_w}{180\Omega} \qquad (7)$$

The resolution of the shaft encoder was $\pm 0.176°$, which corresponded to $\Delta t = 1.39 \times 10^{-5}$ sec. Table 7 presents the total uncertainty in velocity $\Delta V$ for the convective velocity measurements for both advance ratios.

To evaluate the frame-to-frame fidelity of the videotape system, the convective velocity was analyzed with azimuthal intervals of 11.25° for interframe analysis and 90° for intraframe analysis. The convective velocity was determined by analysis of the distance between successive vortices over the given azimuthal increment. The time to traverse the distance is given by the previous equation. By summation of the convective velocities

between each azimuthal increment over the total wake history, a standard deviation of the mean convective velocity was determined. The frame-to-frame fidelity was quantified by

$$\Delta x = [(\Delta V)t]_{11.25} = [(\Delta V)t]_{90} \qquad (8)$$

The configuration for $y/R = -0.8$ and $\mu = 0.15$ was analyzed. For the 11.25° increment, the standard deviation of the convective velocity was determined to be 67.51 ft/sec and $\Delta x$ was determined to be 0.72 in. A standard deviation of 9.24 ft/sec and a $\Delta x$ of 0.79 in. were computed for the case where the azimuthal increment was 90°. Because $\Delta x$ for both azimuthal increments was approximately equivalent, the frame-to-frame fidelity was considered to be very good.

## Analytical Methods

The experimental data were compared with the results of four computer codes: (1) a Navier-Stokes method developed at Iowa State University to compare the location of the experimental roll-up of the tip vortices into an apparent disk vortex, the vertical trajectory, the horizontal contraction, and the rotor performance (this computer code was chosen to compare the results of a relatively new prediction method with experimental data), (2) a comprehensive computer code, Comprehensive Analytical Method of Rotorcraft Aerodynamics and Dynamics–Johnson Aeronautics version (CAMRAD/JA), to determine free-wake geometries for comparison with the experimental tip vortex location, vertical skew angle, and rotor performance (the computer code was readily available and had been widely used in previous comparisons with in-house experimental data (ref. 38)), (3) a prescribed wake geometry computer code, the Generalized Wake module developed at United Technologies Research Center (UTRC) (ref. 6), for comparison with the experimental tip vortex location and vertical skew angle (this computer code offered the advantage of being simple to run and utilized a mature prediction technique), and (4) a Rotor-Wake-Fuselage (RWF) computer code, which was developed by the U.S. Army at NASA Langley Research Center (ref. 39), to generate free-wake geometries by a vortex lattice method for comparison with the experimental tip vortex location and vertical skew angle of the wake with and without the effects of the fuselage (the RWF computer code allowed the comparison of the effects of the fuselage on the geometry of the wake).

### Three-Dimensional Navier-Stokes Calculations

In this method the viscous flow field surrounding the rotor was modeled by the steady laminar incompressible 3-D Navier-Stokes equations. These equations were

solved by a finite volume approach known as SIMPLER. (See ref. 40.) The rotor blades were modeled implicitly as time-averaged source terms embedded in the momentum equations. The source terms were added only at the points in the computational grid through which the rotor blades pass. (See ref. 41.) Therefore, in this technique a body-fitted rotational grid was not required for the rotor blades. The computational grid was used only to simulate the flow field induced by the rotor system on an average or steady-state basis. A consequence of this modeling technique was that less CPU memory was required in the simulation of the rotor flow field than for the conventional Navier-Stokes computations in which a dense body-fitted grid over the rotor blade surface is needed.

As the rotor blade spins, it imparts a certain amount of momentum to the fluid. This change in momentum is related to sectional aerodynamic and geometric characteristics of the blade. With the computed blade section Mach number and angle of attack, a look-up table was used to obtain the local lift and drag coefficients. Next, the source terms were calculated from the rotor forces and added to the momentum equations. The source terms, which were unknown at the start of the iterations, were fully coupled with the flow field and evolved as part of the solution. Therefore, the presence of the rotor influenced the flow field, and in turn, the perturbed flow field altered the load and the inflow distribution on the rotor disk from one iteration to another until a steady-state converged solution was reached. (See ref. 42.)

In this analysis, the cyclic and collective pitch inputs were determined from a trimming procedure based on the approach given in reference 43. For a given flow field around the rotor, the steady-state flapping motion of a blade was determined by solution of a nonlinear equation representing the sum of moments about a flapping hinge. Next, an inner-loop iteration was performed to achieve zero flapping with respect to the tip-path plane by cyclic pitch adjustments. The desired propulsive force was attained by an outer-loop iteration to adjust the collective pitch. No attempt was made to achieve a complete moment balance on the rotor disk.

The Navier-Stokes computations were performed only on an isolated rotor system. Therefore, the fuselage was not modeled. The calculations were conducted on a stretched cylindrical grid, which was aligned with the free stream, with 114000 control volumes. The grid density was increased in the vicinity of the rotor system to capture the two resulting apparent disk vortex structures. A velocity vector plot is shown in figure 6 at $x/R = 1.88$ and $\mu = 0.15$. A velocity vector is plotted at each grid point and, thus, is a good indication of grid size and density.

The location of the apparent disk vortex was obtained from a plot of vorticity contours in the region of the apparent disk vortex and the center of the vorticity contours. Figure 7 shows a representative vorticity contour plot used to determine the center of the roll-up of the tip vortices into apparent disk vortices at $x/R = 1.88$ and $\mu = 0.15$. The data were then converted into wind axis coordinates. A converged solution was attained in 400 iterations with each iteration taking about 10 sec of CPU time on the Cray Y-MP computer.

### CAMRAD/JA Model

Theoretical performance parameters and rotor wake geometry results were generated by CAMRAD/JA. (See ref. 44.) The CAMRAD/JA was used in this study because it had been used previously to analyze the rotor system and was able to provide performance estimates as well as wake geometry predictions with a free-wake approach.

The free-wake analysis of CAMRAD/JA is based on the method of Scully. (See ref. 7.) Line segments are used for the tip vortex with either rectangular sheets or line segments (the present analysis) used for the inboard-shed and trailed wake vorticities. The geometry of the tip vortices was allowed to distort outboard of the 80-percent span. Inboard of this, a rigid geometry was used. The wake is modeled with a near- and far-wake scheme. The near wake was rigid (fixed with respect to the blade), whereas the far wake was allowed to distort, which increased the computational efficiency.

The analysis was performed by trimming the rotor thrust coefficient and the longitudinal and lateral flapping angles to experimental values by use of collective and cyclic blade pitch with a fixed shaft angle. Trim parameters used in the present analysis included 70 control iterations, a tolerance for motion convergence EPMOTN = $0.001°$, a factor reducing control increment in order to improve trim convergence FACTOR = $0.1$, and a tolerance for circulation convergence EPCIRC = $\Delta C_T / \sigma = 0.001$. The control step in perturbation identification of derivative matrix DELTA was $1.2°$ with five trim iterations between perturbation MTRIMD.

Nine radial aerodynamic segments were used with edges at $r/R = 0.246, 0.450, 0.550, 0.663, 0.738, 0.800, 0.850, 0.900, 0.950,$ and $1.000$. The extents of the wake regions in azimuthal increments of $15°$ were as follows: near wake of 6, rolling-up wake of 12, far-wake tip vortices of 48, and far-wake tip vortices (for points off the rotor disk) of 96. Three wake geometry iterations were used in the analysis. A tip loss factor of 0.97 was used, and static stall and unsteady aerodynamic models were incorporated in the analysis. The tip vortex core size was

set to $0.0025R$ for the nonuniform inflow model and free-wake model. The vortex-bursting model was suppressed. Airfoil section characteristics used in the analysis were taken from the NACA 0012 airfoil data table of reference 45. The tip vortices were composed of line segments of linear circulation distribution, and the resolution of the wake analysis was 15°. A uniform radial distribution was used for blade mass, chordwise bending stiffness, torsional stiffness, and flapwise bending stiffness.

The wake geometry output gave wake age in degrees and the $x$, $y$, and $z$ locations of the tip vortex in the TTP coordinate system. The data were converted to the wind axis coordinate system (the coordinate system of the experimental data). Then, converted data were interpolated linearly to obtain tip vortex locations in the plane of the laser light sheet. The CW and CCW tip vortices were sorted in ascending wake age. The calculations required approximately 5 min of CPU time on a Cray-2 S supercomputer.

### Generalized Wake

A stand-alone version of the UTRC Generalized Wake module (ref. 46) was used to generate theoretical rotor wake geometries. The analysis was extremely quick and easy to use with limited data input ($C_T$, $\alpha_{TPP}$, $\mu$, $a_0$, and number of blades).

The Generalized Wake models the wake as a classical undistorted skewed helical sheet of vorticity and a distorted tip vortex. The undistorted tip vortex geometry, $x/R$ and $y/R$, is given by

$$\frac{x}{R} = \cos(\psi_w - \psi_b) + \mu\psi_w \tag{9}$$

$$\frac{y}{R} = -\sin(\psi_w - \psi_b) \tag{10}$$

The $z/R$ coordinate of the undistorted wake was obtained from $C_T$, $\alpha_{TPP}$, and $\mu$. The tip vortex geometry was then distorted in the $z$ coordinate. The tip vortex distortion function was generalized from the identified wake definition parameters. (See refs. 6 and 47.) Observations of the helicopter wake were made to develop fundamental mathematical models to represent the axial distortion. The distortion is based on an amplitude-scaling function and a geometric shape function. The amplitude-scaling function generalizes the amplitude of the distortions with wake age, and the shape function generalizes the characteristic azimuthal distribution of the distortions with wake age. The amplitude-scaling function was acquired from an exponential curve fit of the variations of the distortion peaks with wake age. An analytical study was conducted to evaluate mathematical expressions for the amplitude-scaling factor and shape function and was

based on distorted wake predictions for several actual and representative rotors and operating conditions.

The wake geometry output gave wake age in degrees and the $x$, $y$, and $z$ locations of the tip vortex in the TTP coordinate system. The data were converted to the wind axis coordinate system (the coordinate system of the experimental data). Then, converted data were interpolated linearly to obtain tip vortex locations in the plane of the laser light sheet. The CW and CCW tip vortices were sorted in ascending wake age. The calculations were performed on a workstation and CPU time was negligible.

### RWF Model

The Rotor-Wake-Fuselage (RWF) computer program was used to determine the combined aerodynamic effects of lifting rotor system full-sheet free wakes in the presence of a nonlifting fuselage. This analysis used a limited number of inputs (i.e., number of blades, advance ratio, blade twist, rotor shaft, collective pitch, cyclic pitch, coning angle, and flapping angles) to determine the wake of an untrimmed rotor. (See ref. 48.)

The method of computation of the effects of the lifting rotor blade in steady flight was developed with a conventional vortex lattice method for the blades and wake with constant-source panels for the fuselage. Piecewise constant-strength vortex filaments were computed from doublet panels representing the panels of the rotor blade and wake geometry. The Biot-Savart law was applied to each segment of the combined blade wake vortex lattice to compute the convected distortion for all points in the wake. Boundary conditions permitted an arbitrary velocity and orientation in space for each panel.

The unsteady aerodynamics are solved by time stepping a solution with quasi-steady approximations to the flow. The initial geometry of the rotor wake includes only a single downstream row of doublet panels that represent the rotor wake. The solution procedure impulsively starts the rotor, and at each successive time step, the rotor blade sheds a new downstream row of doublet panels. The solution of the system of equations is made in a series of time steps as the rotor system advances through successive azimuthal steps and the geometry of the rotor and body moves forward in the fluid.

The potential theory model for calculation of the aerodynamic characteristics of a nonlifting fuselage configuration was adapted from the method of Hess and Smith. (See ref. 49.) The computer code modeled the flow in the presence of nonlifting fuselage elements and determined the source strength for each of the panels forming the fuselage surface. Separated regions on the fuselage were neglected. Compressibility effects were

neglected, and retreating blade separation and flow reversal were not closely modeled. Thirty panels were used for each blade, and 650 fuselage panels were used.

The wake geometry output gave the $x$, $y$, and $z$ locations of the outer edge of the vortex sheet in the TTP coordinate system. The data were converted to the wind axis coordinate system (the coordinate system of the experimental data). Then, the converted data were interpolated linearly to obtain tip vortex locations in the plane of the laser light sheet. The CW and CCW tip vortices were sorted in ascending wake age. The calculations required approximately 12 hr of CPU time on an SGI 4D/35 workstation.

## Results

### Performance Comparisons

Table 8 provides a comparison between experimental rotor performance and the predictions of CAMRAD/JA and the 3-D Navier-Stokes computer codes. In the table, note the significant discrepancy between the power measured experimentally and that predicted by CAMRAD/JA. Numerous attempts to improve correlation with the measured performance parameters by manipulation of the size of the tip vortex core radius proved to be of limited effectiveness. Manipulation of the tip vortex radius brought about only minor changes in the wake geometry and had no effect on the vertical skew angle of the tip vortices. In light of this, Scully (ref. 7) recommended that a tip vortex radius of $0.0025R$ ($0.03c$) be used in this study. Note that the coning angle was not measured in this test. The estimate of the coning angle is based on data from a previous test with the same rotor system.

### Vortex Position

*Disk vortex.* The roll-up of the edges of the total rotor wake structure is called an apparent disk vortex. The laser light sheet used to visualize this apparent disk vortex was a continuous beam and was oriented perpendicular to the free stream at locations of $x/R$ from 1.0 to 4.0 in increments of $0.5R$ and permitted a time-averaged view of the rotor wake. For all locations, the apparent disk vortex exhibited a well-defined center void of particles. A typical videotape image of the roll-up of the tip vortices into an apparent disk vortex is shown in figure 8. The center of the apparent disk vortex is the area void of smoke particles in the center of the vortex structure. Figures 9 and 10 show the lateral contraction of the apparent disk vortex at stations downstream of the rotor for advance ratios of 0.15 and 0.23, respectively. Recall that the experimental data were obtained with an average of 30 images for a single apparent disk vortex location.

These figures also show the apparent disk vortex paths determined from the results of the Navier-Stokes solver. The Navier-Stokes solver gave the vorticity contours behind the wake, and the center of the apparent disk vortex was determined from these vorticity contours. Note that the coordinate (0,0,0) is the center of the rotor hub with the sign and axis convention shown in figure 4. In figures 9 and 10, note that the curves exhibited a slight contraction downstream of the disk. The theoretical predictions for both advance ratios appear to be very good except far downstream on the advancing side of the rotor disk. The effect that the rotor moment imbalance of the Navier-Stokes results has on the rotor wake is unknown. A least-squares fit to a linear trajectory was performed on the experimental and theoretical data to determine wake contraction $\alpha_l$ and the results are presented in table 9. Note that for a given advance ratio, the disk vortex appeared to have a greater contraction on the advancing side for the experimental data than for Navier-Stokes predictions.

Figures 11–14 depict the apparent disk vortex trajectories $\alpha_l$ with respect to the horizontal plane for both advance ratios. The theoretical predictions compare very well with the experimental data. From the contraction data in table 9, note that both theoretical and experimental data show that increasing the advance ratio produces a decrease (in absolute magnitude) in the slope of the disk vortex trajectory for both the retreating and advancing sides. This decrease is a consequence of a higher free-stream velocity flattening out the trajectory for the higher advance ratio.

For a constant advance ratio and thrust coefficient, the disk vortex trajectories appear to indicate the relative strength of the rotor downwash between the advancing and retreating sides. Greater downwash on the advancing side, relative to the retreating side, is indicated by the greater downward slope of the apparent disk vortex trajectory on the advancing side, as shown in table 9. This greater downwash on the advancing side for both theoretical and experimental data can be qualitatively understood from the cycloidal geometry of the tip vortex wake. On the advancing side of the rotor disk, the tip vortex filaments from all the blades are more aligned with the free-stream velocity and with each other. Consequently, the filaments act in unison to produce a greater downwash on the advancing side. Although this qualitative argument assumes nearly constant tip vortex strength, this asymmetry of the rotor wake has been seen previously on both small- and full-scale rotor systems (refs. 17 and 19) and has been predicted theoretically (e.g., ref. 12).

*Tip vortex.* By orientation of a strobed laser light sheet parallel to the flow, the individual blade tip vortices

were illuminated. A typical videotape image is shown in figure 15 with annotations of the terms used to describe the results. In this example, four vortex structures are identified: tip vortices that rotate clockwise (CW) (seen by an observer standing on the port side of the rotor system in forward flight) and form a part of the lower wake boundary, a second row of tip vortices downstream of the first row that rotates counterclockwise (CCW) and forms a part of the lower wake boundary, tip vortices that distort and wrap around the apparent disk vortex and form an upper boundary of the wake, and a cone created by the tip vortices rolling up into the apparent disk vortex. The terms lower and upper boundary of the wake pertain to the position of the tip vortices in relation to the roll-up into an apparent disk vortex. The part of the wake that forms a lower boundary lies below the roll-up, and the part of the wake that forms an upper boundary lies above the roll-up of the tip vortices into an apparent disk vortex. Figure 16 shows the same configuration as figure 15 but with the wind tunnel lights turned on.

A simplified representation of the wake is shown in figure 17 and depicts the blade tip vortex as it cuts through the laser light sheet as seen from above. The observer (i.e., the video camera) perceives a clockwise rotation of the tip vortices created as the rotor blades slice through the laser light sheet at an azimuth of 233°. An apparent counterclockwise rotation of the tip vortices is seen when the rotor blade reenters the laser light sheet at an azimuth of 306°. On the outboard edge of the wake the tip vortex distorts, rolls up (or comes out of the page in fig. 17), and moves inboard; thus, it forms an upper boundary of the wake structure as it slices through the laser light sheet again. An apparent disk vortex forms between the lower wake boundary and the upper distorted wake. This apparent disk vortex expands as it moves downstream and, when sliced by the laser sheet, appears as a slice of a cone-shaped structure. From the side view with a laser light sheet, the wake is seen as a series of vortices emanating from the forward and aft portions of the rotor disk. (See fig. 18.)

The vortices seen in figure 15 occur when the blades are located at azimuthal angles of 0°, 90°, 180°, and 270°. Two trains of tip vortices are created by the rotor blades. The vortices rotating CW are created when the rotor blade is situated in the forward section of the rotor disk, and the vortices rotating CCW are created when the rotor blades are positioned on the aft portion of the disk. The strobed laser light sheet caused the vortices to appear stationary, and every fourth tip vortex represented one complete rotor revolution. No noticeable unsteadiness was observed when the videotape was viewed even for relatively "old" tip vortices (i.e., vortices with a wake age greater than 360°). A single image could contain, in some instances, tip vortices of 3 to 4 rotor revolutions.

However, multiple images were required to analyze all the tip vortices for a given condition.

The data obtained from figure 15 were plotted in figure 19. Figure 19(a) depicts a simplistic representation of the videotape image shown in figure 15. The idealized vortex locations are then plotted in figure 19(b). The space between the vortex cores can be filled by a change of phase of the strobed laser light with respect to the reference blade in 11.25° increments until an increment of 90° is obtained.

As noted in the section "Uncertainty Estimates," a statistical analysis, which also quantified wake periodicity, was conducted on three tip vortices in three locations. The rotor wake was periodic and repeatable. Table 2 represents the subjectivity error found in this test but also provides a conservative estimate of wake periodicity.

Figures 20–27 show the vortex trajectory data taken with the laser light sheet situated at $y/R = \pm 0.8$ and $\pm 0.3$ and at two advance ratios of 0.15 and 0.23. Also plotted are the theoretical results obtained from CAMRAD/JA (Scully free wake), Generalized Wake (prescribed wake), and the RWF analysis of the tip vortex trajectories with and without the effects of a fuselage in the flow. The theoretical data were obtained by linear interpolation of the wake geometry coordinates closest to the laser light sheet plane on either side of the target $y/R$ location of the light sheet plane.

The experimental data in figures 20–27 are presented for a vortex core that is clearly visible. Because of geometry, the vortices should first cross the laser light sheet at $x/R = \pm 0.6$ for a light sheet positioned at $y/R = \pm 0.8$ and at $x/R = \pm 0.95$ for a light sheet positioned at $y/R = \pm 0.3$. This origin tip vortex location is obtained from

$$\frac{x}{R_{origin}} = \left[1 - \left(\frac{y}{R}\right)^2\right]^{1/2} \tag{11}$$

In most instances these tip vortex locations, where the rotor blade first crosses the laser light sheet plane, were documented with the light sheet strobe slip synchronized.

For an advance ratio of 0.15 and a laser light sheet plane at $y/R = 0.8$ (figs. 20(a) and 21(a)), the experimental data are compared with three theories (CAMRAD/JA, Generalized Wake, and RWF). The tip vortices, which are visible toward the front of the rotor disk (i.e. the lower boundary CW data), initially convect above the TTP and then descend. This effect on the leading edge of the rotor disk (also reported by other researchers in refs. 20, 28, and 50) is due to the upwash induced by the rotor. The tip vortex farthest upstream will be induced upward by the downstream tip vortices. After the first blade passage, this tip vortex will be induced downward

by the tip vortex, which is now farthest upstream. (See ref. 7.) Inflow measurements at advance ratios of 0.15 and 0.23 on the present experimental configuration have confirmed the existence of significant upwash on the leading edge of the rotor disk. (See refs. 13 and 51.)

Figure 20(a) shows experimental data plotted with results from CAMRAD/JA and Generalized Wake. Neither theory predicted the initial upwash of the experimental CW data. The Generalized Wake predicted the downstream convection of the experimental CCW tip vortices better than CAMRAD/JA. Because of video camera optical blockage caused by the fuselage, only a limited amount of experimental CW data could be obtained. Well-defined vortices were not apparent for the experimental CCW data until $x/R = 1.1$ instead of $x/R = 0.6$, where the vortices actually originated in this laser light sheet plane, as seen in figure 20(a) for $\mu = 0.15$.

At a higher advance ratio of 0.23, the Generalized Wake accurately predicted the location of the CCW tip vortices, as shown in figure 20(b). Once again, data from the CAMRAD/JA CCW overpredict the downward convection of tip vortices. Neither theory accurately predicts the initial upwash or the downward convection of the experimental CW tip vortices. The scarcity of data between $x/R = 0.3$ and 1.00 is due to video camera optical blockage by the fuselage. The primary video camera was located on the retreating side of the disk, and a significant number of tip vortices were hidden behind the fuselage (the laser light sheet plane was positioned on the advancing side). Visible CCW vortices were not apparent until approximately $x/R = 1.3$, which is a significant distance from the origin of the vortices at $x/R = 0.6$. The video camera, which was positioned on the advancing side of the rotor, viewed only the forward portion of the disk.

Experimental data and results from the RWF computer code (with and without fuselage effects) are shown in figure 21(a) for a laser light sheet plane of $y/R = 0.8$ and an advance ratio of 0.15. The fuselage has little effect on the tip vortex trajectory of the RWF computer code. The RWF results, with and without fuselage effects, fail to predict the extent of the upwash of the experimental CW data and overpredict the tip vortex vertical skew angle for the experimental CW and CCW data. Figure 21(b) combines the RWF analysis results with the experimental data at a laser light sheet plane of $y/R = 0.8$ and an advance ratio of 0.23. Again, little effect of the fuselage on the tip vortex trajectories is noted for the RWF analysis. The RWF results overpredict the downward convection of the experimental tip vortices and fail to predict the extent of the initial upwash of the experimental CW data. The jagged nature of the RWF theoretical data seen farthest downstream in figures 21(a)

and 21(b) is due to the time-stepping method of this computer code.

More inboard at a laser light sheet location of $y/R = 0.3$ and $\mu = 0.15$, CAMRAD/JA adequately predicted the experimental CCW data. (See fig. 22(a).) The Generalized Wake underpredicts these data, and both theories fail to accurately model the initial upwash and the downward convection of the experimental CW tip vortices. Again, the gaps in the experimental CW data for both advance ratios were due to video camera optical blockage by the fuselage. At the higher advance ratio of 0.23 for the laser light sheet plane of $y/R = 0.3$ (fig. 22(b)), CAMRAD/JA and the Generalized Wake underpredict the initial upwash seen in the experimental CW data. The Generalized Wake underpredicted the downward convection of the experimental tip vortices; however, experimental tip vortex convection data are predicted by CAMRAD/JA.

The RWF computer code slightly underpredicts the extent of the initial upwash of the experimental data for a laser light sheet location of $y/R = 0.3$ and $\mu = 0.15$. (See fig. 23(a).) Surprisingly, the effect of the fuselage on the tip vortex trajectory is predicted to be small in this more inboard plane. This effect is attributed to the fact that the fuselage is a slender body. The RWF analysis predicts well the tip vortex trajectory of the experimental data at the higher advance ratio of 0.23. (See fig. 23(b).) Slight effects of the tip vortex trajectory caused by the fuselage are noted for RWF analysis of the CW vortices.

With the laser light sheet positioned at $y/R = -0.3$ (retreating side) and $\mu = 0.15$, the Generalized Wake initially predicts well the location and trajectory of the experimental tip vortices for the lower advance ratio. (See fig. 24(a).) Note that experimental CCW data at an advance ratio of 0.15 were not visible. However, the Generalized Wake failed to predict the significant change in the tip vortex vertical skew angle of the experimental CW data at $x/R = 0.5$ for an advance ratio of 0.15. For $x/R > 0.5$, the experimental CW tip vortices are seen to convect downward at a steeper angle than the experimental CW tip vortices for $x/R < 0.5$. The CAMRAD/JA predicted a significant change in vortex vertical skew angle (although a lesser magnitude) at $x/R = -0.4$ instead of at the experimental value of $x/R = 0.5$. The RWF analysis predicts well the experimental CW data. (See fig. 25(a).)

The CAMRAD/JA and the Generalized Wake adequately predicted the location of the tip vortices for $\mu = 0.23$. (See fig. 24(b).) The CAMRAD/JA slightly overpredicted the downward convection of the experimental CW tip vortices, whereas the Generalized Wake slightly underpredicted the downward convection of the experimental CCW tip vortices. The RWF computer code at the higher advance ratio was seen to adequately

12

predict the location of the tip vortices. (See fig. 25(b).) Little difference was noted between the RWF computer code run with fuselage effects and the RWF computer code run without fuselage effects.

Figure 26(a) shows results at a laser light sheet position of $y/R = -8$ and $\mu = 0.15$. The CAMRAD/JA model predicted the experimental wake geometry very well. In fact, the model prediction is perplexing because CAMRAD/JA does such a good job of matching the experimental data (particularly the experimental CW data) on the retreating side but does such a poor job of predicting the experimental behavior on the advancing side. The Generalized Wake underpredicted the tip vortex vertical skew angle. In figure 27(a), the RWF computer code predicted the initial upwash of the experimental CW tip vortices but underpredicted the downward convection of the experimental tip vortices.

At the higher advance ratio of 0.23 at a laser light sheet plane of $y/R = -0.8$, CAMRAD/JA predicts the tip vortex trajectory for both CW and CCW data. (See fig. 26(b).) The Generalized Wake underpredicts the experimental data. The RWF computer code predicts the tip vortex trajectory with only minor effects of the fuselage noted on the computed tip vortex trajectory. (See fig. 27(b).) The relatively slender body is not expected to have any significant effects at $y/R = \pm0.8$.

As mentioned previously, the tip vortices wrap up and around the apparent disk vortex. The wrap-up of the tip vortices are shown in figure 28 and defined as the experimental upper tip vortex data. Also plotted in these figures are the apparent disk vortex locations that were described previously. Although the $y/R$ locations for these data are not quite the same as the laser light sheet plane, they are used here to show that the apparent disk vortex position lies between the upper and lower boundaries of the tip vortices. Note that all experimental upper tip vortex data consisted of vortex "foot prints" (series of crests and troughs) without clearly defined vortex centers.

Figure 28(a) shows the tip vortex wrap-up that occurs for a laser light sheet location of $y/R = -0.8$ and an advance ratio of 0.15. From the experimental data, the apparent disk vortex center lies between the experimental CCW and upper tip vortices. The CAMRAD/JA predicted a wrap-up to be much lower than the experimental (upper) wrap-up. In addition, a predicted apparent disk vortex, which lies between the CAMRAD/JA CCW and upper tip vortex data, is lower than the experimental apparent disk vortex location. However, what is unclear is the effect that the relatively coarse resolution of 15° used for the CAMRAD/JA computations has on the prediction of the vortex wrap-up location and trajectory.

For an advance ratio of 0.15 and a laser light sheet plane at $y/R = 0.8$ (fig. 28(b)), the apparent disk vortex position lies between the experimental CCW and upper tip vortex data. The CAMRAD/JA CCW and upper tip vortex predictions are also plotted. Once again, CAMRAD/JA predicted a wrap-up to be significantly lower than the experimental data. The prediction of the apparent disk vortex position, as suggested by the CAMRAD/JA prediction, is significantly lower than the apparent disk vortex position determined experimentally.

Figure 28(c) shows the tip vortex wrap-up that occurs for a laser light sheet location of $y/R = 0.8$ and an advance ratio of 0.23. Consistent with the above observations, the location of predicted CAMRAD/JA upper tip vortex data is significantly lower than the experimental upper tip vortex data. Again, the CAMRAD/JA prediction is significantly lower than the apparent disk vortex position determined experimentally.

A summary of the tip vortex vertical skew angle data is provided in tables 10 and 11. An (a) in the column in the tables indicates insufficient data. Values were obtained by a linear least-squares fit of the data. As a comparison, the momentum wake angle $\alpha_w$, which was determined from classic momentum considerations (function of advance and inflow ratios in ref. 21), was calculated to be $-14.01°$ at $\mu = 0.15$ and $-9.44°$ at $\mu = 0.23$ with respect to the horizontal plane. The scarcity of experimental data in some instances may give misleading conclusions, particularly for $y/R = 0.8$ and $\mu = 0.15$. Nevertheless, important trends were observed, which are described as follows.

At the lower advance ratio of 0.15 and for the outboard laser light sheet planes of $y/R = \pm0.8$, the greatest (in absolute magnitude) vertical skew angle is shown on the retreating side. (See table 10(a).) This was the opposite of the trend seen previously for the apparent disk vortices. Recall that the apparent disk vortex trajectory on the advancing side had a greater slope when compared with the retreating side. With a laser light sheet oriented perpendicularly to the free stream, the apparent disk vortices were generally more tightly rolled up on the advancing side than on the retreating side. (See fig. 29.) In addition, this tighter roll-up may be seen by comparison of the cone angles (the angle formed by the upper and lower CCW boundaries) in figures 28(a) and 28(b). The cone angle on the retreating side was approximately 22°, whereas on the advancing side, the cone angle was estimated to be 12°. The greater concentration and alignment of tip vortex filaments on the advancing side may be a reason for the blade tip vortices to be more tightly rolled into the apparent disk vortex on this side. The CAMRAD/JA predicted a cone angle, the angle formed between the CCW lower and upper boundaries,

to be 11° on the retreating side and 9° on the advancing side.

At the higher advance ratio, the outboard tip vortices had approximately the same vertical skew angle on the retreating side as on the advancing side. (See table 10(b).) Both experimental and CAMRAD/JA data predicted a cone angle, the angle formed between the CCW lower and upper boundaries, of 8°.

For the outboard planes of $y/R = \pm 0.8$ and at both advance ratios, the Generalized Wake model predicted the greater vertical skew angle of the tip vortices to exist on the retreating side, but CAMRAD/JA and RWF (both with and without a fuselage) predicted the greater vertical skew angle of the tip vortices to occur on the advancing side.

With the laser light sheet positioned at the inboard planes of $y/R = \pm 0.3$ and for both advance ratios, the vertical skew angle was greater on the advancing side than on the retreating side. The lone exception was CAMRAD/JA CCW data at an advance ratio of 0.23.

In figures 30–33 a single tip vortex filament was viewed from above, viewed from behind, and plotted as height $z/R$ versus wake age for a blade azimuth of 0°. From the view above, the theories generally do predict the $X$-$Y$ plane wake geometry well. (See figs. 30(a), 31(a), 32(a), and 33(a).) However, a discrepancy resulted between theoretical and experimental data for the inboard laser light sheet planes $y/R = \pm 0.3$. Note that the experimental data (except for $y/R = 0.3$ and $\mu = 0.23$) were significantly upstream of the predictions for both advance ratios. The scarcity of laser light sheet plane cuts makes results unclear if rotor-fuselage interactions or some other wake-distorting effects are having an influence on the inboard portion of the wake.

In figures 30(b), 31(b), 32(b), and 33(b), the downward displacement of the theoretical tip vortex traces at approximately $y/R = \pm 0.6$ was thought to be an indication of downwash strength. The greater vertical skew angle seen on the advancing side of the CAMRAD/JA and RWF (with and without fuselage effects) data, when compared with the retreating side, indicated greater downwash on this side. Conversely, the Generalized Wake data had a greater vertical skew angle on the retreating side, which would correspond to a greater downwash on this side. The experimental data showed that the greatest apparent disk vortex trajectory slope was on the advancing side and that the tip vortices on that side exhibited a tighter roll-up into the apparent disk vortex. (See fig 29.) The tip vortices exhibit a more shallow trajectory on the advancing side. Thus, CAMRAD/JA was seen to predict the correct trends in the downwash but not the correct tip vortex distortion.

Figures 30(c), 31(c), 32(c), and 33(c) (plotted as height $z/R$ versus vortex wake age) show good correlation between the experimental data and the predictions of the Generalized Wake and the RWF computer codes. The predicted results of the RWF computer code with fuselage effects were only slightly better than the RWF computer code without fuselage effects. (See figs. 32(c) and 33(c).) For wake ages greater than 135°, the CAMRAD/JA data are seen to generally overpredict the wake downwash. (See figs. 30(c) and 31(c).)

## Vortex Convective Velocity

The net convective velocity of the tip vortices in the plane of the laser light sheet was estimated by computation of the distance between the first and last vortex, the time required to traverse that distance, and the rotor speed in rpm (a constant). The convective velocities calculated in this manner are shown in table 11. The convective velocities in the table are based on the distance between the farthest visible vortex upstream and the farthest visible vortex downstream. From quantification of the ratio of speeds $V/V_\infty$, the tip vortices generally are convected downstream at approximately the free-stream velocity.

Data indicate that the upper tip vortices convect noticeably slower downstream. Slower convection is most likely due to the inherent difficulty in determination of the time required for the vortex to convect the given distance. Recall that the upper tip vortex data occur when a tip vortex rolls up and over the apparent disk vortex. The upper tip vortex intersects the laser light sheet plane twice. (See fig. 17.) The location of the two vortex intersections could not be determined, and a more detailed study of the roll-up behavior is needed.

The angles of the convective velocity vector are given in table 12 along with the components $u$ and $w$ of the convective velocity. Because the convective velocity angle was determined as the angle between the beginning vortex and the ending vortex, these angles will be different from the vortex vertical skew angles (table 10) that were determined from a least-squares fit of the tip vortex data.

## Particle Void Size of Tip Vortex

In this experiment, an attempt was made to quantify the tip vortex core size by measurement of the size of the dark region void of particles in the center of the vortex. Results are shown in figures 34 and 35. The term particle void size is used instead of vortex core size to differentiate between the experimental measurement and the true vortex core size. As shown in figures 34(a) and 34(b), the particle void size increased with increasing distance

14

downstream. The average particle void size was approximately $0.2c$.

Table 13 shows reported vortex core sizes (based on maximum tangential velocity) determined by a variety of measurement techniques and test conditions. Core sizes measured with hot-wire probes (refs. 15 and 52–54) and shadowgraphy (refs. 24–26, 28, and 55) result in the reported core sizes to be relatively small ($r_v/c < 0.07$ for moderate thrust coefficients) and, generally, to not increase significantly with wake age (the exception is in refs. 15 and 55). These results are in marked disagreement with studies that utilized smoke flow visualization (refs. 56–58 and the present investigation) or laser velocimetry (ref. 59), where the core sizes were reported to be larger and to increase with wake age. A possible explanation is that the smoke particles were being centrifuged by the vortices causing inaccuracies in the true measurement of the vortex core size.

The smoke generator used in this test emitted vapor with a particle size of 4 to 6 μm. (See ref. 60.) The density of seeding particles is also important (propylene glycol has a specific gravity of 0.968). Observations were similar for the apparent disk vortex particle void size, which further confirms suspicions of particle centrifuge and dispersion. (See figs. 35(a) and 35(b).)

As discussed earlier, no noticeable vortex core position fluctuation was observed. This observation was at variance with reported results and observations of Light, Norman, and Frerking (ref. 27) and Leishman and Bagai (ref. 28) who reported the vortex core location to fluctuate noticeably for wake ages greater than approximately 270°. In this study, part of the reason for no noticeable vortex core fluctuation may be the inherent difficulty in the true vortex core being visible with smoke particles. The void sizes measured in this study were at least five times larger than those reported from shadowgraph core size measurements. Because fluctuations reported by Light et al. were on the order of 1 or 2 core diameters, the fluctuations may not be easily seen with smoke particles.

Accurate measurements of vortex core size may be possible with laser light sheets. However, care must be exercised in the choice of particle size and density.

**Inboard Sheet Edge Vortex**

In the longitudinal data analysis, multiple vortices were noted to exist in the wake that could not be identified as a primary tip vortex (either CW or CCW). These vortices were attributed to the roll-up of the outer edge of the trailing vortex sheet into a discrete vortical structure.

Recall that the wake of the rotor blade consists of the coalesced tip vortex and a trailed vortex sheet. The sheet and the discrete tip vortex are separated by the change in

sign of the circulation bound to the rotor blade near the tip. Furthermore, the inboard sheet convects downward at approximately twice the rate of the tip vortex. (See ref. 5.) The trailed vortex sheet, which has been visualized in hover studies (ref. 5), is believed to roll up at the outer edge, which is in close proximity to the tip vortex. This process is sketched in figure 36(a). The roll-up of the outer edge of the vortex sheet follows a cycloidal path in a manner similar to the tip vortex, but more inboard. Viewed from the side in a laser light sheet, the trailed vortex sheet is inboard of the tip vortex. (See fig. 36(b).)

A roll-up of the inboard vortex sheet into a coherent vortex is predicted on a rotor blade according to criteria set forth by Betz (ref. 61) and Rossow (ref. 62). Vortex roll-up will occur at sites of maximum sheet strength or abrupt changes in sheet strength. (See ref. 62.)

The inboard sheet vortex (ISV) has been modeled on helicopter wakes by free-wake computer codes (refs. 63 and 64), but, until recently, visualization with ISV has been difficult due to the relative weakness of the ISV. Mueller (ref. 65) investigated ISV in a water tunnel on a simple nonrotating rotor blade. A vortex generator was utilized upstream of the rotor blade to cause a change in the spanwise lift distribution and, thus, create a strong ISV. Recently, Kim, Komerath, and Liou (ref. 66) have reported the existence of ISV on a small rotor system with untwisted blades (triangular blade loading).

Figure 37 shows the vortices attributed to sheet roll-up and affiliated with the CCW tip vortices for the laser light sheet location of $y/R = 0.3$ and $\mu = 0.15$. A magnified view of these vortices is shown in this figure. The vortices attributed to sheet roll-up were periodic, associated with the tip vortices, and visible in all laser light sheet planes and at both advance ratios but were easiest to qualify and quantify on the retreating side of the rotor disk. Video camera optical blockage by the fuselage and the different convection rates between ISV and tip vortex, more noticeable farther downstream, made analysis more difficult on the advancing side. Furthermore, ISV rotation was noted to be in an opposite sense of the associated tip vortex, and the ISV was noted to always be inboard of the associated tip vortex. For clarity, figure 38 shows the same configuration in figure 37 but with the wind tunnel lights turned on.

The vortices attributable to the roll-up of the outer edge of the trailing vortex sheet were quantified for laser light sheet locations of $y/R = -0.8$ and $-0.3$ and for advance ratios of $\mu = 0.15$ and 0.23. (See figs. 39 and 40.) The raw videotape images were run superimposed on a still image of the reference grid and analyzed frame by frame.

**15**

The location of the roll-up of the inboard sheet is shown for $y/R = -0.8$ and $\mu = 0.15$ in figure 39(a). Note that the vertical scale has been expanded for clarity. Also, the point (0,0,0) is the center of the rotor hub. The vortices associated with the CW tip vortices were inboard (closer to the rotor hub) and located higher than the CW tip vortices. The vortices associated with the CCW tip vortices were inboard and located lower than the CCW tip vortices. These locations are geometrically oriented correctly for vortices created by the roll-up of the outer edge of the trailing vortex sheet. Because of coning, shaft tilt, and control inputs to the rotor, the physical location of the blades dictates that the ISV formed on the forward portion of the rotor disk is slightly higher and farther inboard than the corresponding CW tip vortex. (See fig. 36(b).) Likewise, the ISV formed on the aft part of the rotor disk appears inboard and slightly lower than its corresponding CCW tip vortex.

The ISV was hypothesized in reference 65 to be caused by a disturbance of the spanwise blade loading due to blade vortex interaction with the preceding blade. Thus, the ISV was thought not to occur until after first blade passage ($\psi_w = 90°$ for the present rotor system). As seen in figure 39(a), the ISV was observed to occur before the first blade passage ($\psi_w < 90°$). However, the ISV observed before first blade passage was more difficult to see than the ISV created after first blade passage.

The ISV was observed to fluctuate spatially more than the tip vortices, particularly as the ISV convected downstream. The tip vortices appeared stationary during videotape data frame-by-frame analysis, whereas the ISV was observed to fluctuate noticeably frame by frame. This observation may account for the scattering of the ISV seen in figure 39(a).

At the higher advance ratio of 0.23, the ISV occurs slightly inboard and higher than the CW tip vortices. (See fig. 39(b).) The ISV created on the aft portion of rotor disk could not be analyzed.

More inboard at a laser light sheet plane location of $y/R = -0.3$, considerable scatter was noted in the ISV data. (See fig. 40.) In figure 40, the ISV followed the expected geometric relationship with the tip vortices as seen previously in figure 39. Again, the ISV created on the aft portion of rotor disk could not be analyzed.

Reference 66 reported that the distance between the ISV and CCW tip vortex pairs (aft portion of the rotor disk) was approximately twice the distance between the ISV and the CW tip vortex pairs (forward portion of the rotor disk). This difference was not seen in figure 39(a). The distances between vortex pairs were approximately equal for both the aft and forward portion of the wake ($r/R = 0.05$ and 0.06, respectively).

The distance between the first observed tip vortex (before first blade passage) and the corresponding ISV was between $r/R = 0.05$ and 0.08. Immediately after the first blade passage, the distance between the tip vortex and the ISV was computed to be between $r/R = 0.07$ and 0.11. However, after the first blade passage, computation of the distance between the ISV and the tip vortex was difficult because of a difference between sheet and tip vortex convection rates.

An estimate of the location of ISV formation on the rotor blade was based on the difference between tip vortex and ISV locations. (See fig. 41(a).) Based on this method, the ISV distance from the tip vortex was estimated to be between $r/R = 0.05$ and 0.10. The assumption that the tip vortex is formed at $r/R = 0.99$ (ref. 54) corresponds to an ISV formation between $r/R = 0.94$ and 0.89. An alternate method was used to determine ISV formation based on the ISV $x/R$ measurement. (See fig. 41(b).) The ISV formation for this method was between $r/R = 0.95$ and 0.89. Reference 64 predicted that the ISV would occur at $r/R = 0.90$.

A linear least-squares fit was performed to obtain the vertical skew angle for ISV data. (See table 14.) Table 14 showed close agreement between the vortex vertical skew angles of the tip vortex and ISV trajectory. Tip vortex data downstream of the last ISV were deleted so that the vortex vertical skew angle comparison would be over the same distance. Therefore, the tip vortex vertical skew angles in table 14 are different than the tip vortex vertical skew angles in table 10.

## Conclusions

Smoke injection in conjunction with laser light sheet flow visualization has been used in the Langley 14- by 22-Foot Subsonic Tunnel to examine features of the wake geometry of a helicopter rotor in forward level flight (advance ratio $\mu = 0.15$ and 0.23) at one thrust level (thrust coefficient $C_T = 0.0064$). Qualitative as well as quantitative information was obtained and is available for validation of computer codes. Location and skew angle were obtained for the roll-up of tip vortices into an apparent disk vortex and for blade tip vortices. In addition, tip vortex convective velocities were obtained. Theoretical model results were compared with experimental data, which showed the difficulties in prediction of a complex rotor wake flow field. Important conclusions from this study are as follows:

1. The greatest downwash occurs on the advancing side of the rotor as shown by a comparison of apparent disk vortex trajectories.

16

2. The advancing side of the rotor disk has a tighter roll-up of tip vortices into the apparent disk vortex than the roll-up on the retreating side.

3. Tip vortices generally convect streamwise in the plane of the laser light sheet at the free-stream velocity.

4. Vortex core size measurements were attempted. However, due to particle centrifugal action, the measured void size is substantially larger than estimates of core size reported by other researchers using different techniques. Proper selection of particle size and density is required for these data.

5. Vortices were seen in the flow that were periodic and associated with the tip vortices. These vortices rotate in an opposite sense of the tip vortex. Based on the geometry of the analyzed data, these vortices are probably due to the roll-up of the outer edge of the trailing vortex sheet and may be an important feature to model in theoretical computer codes. These vortices are seen both before and after the first blade passage.

6. The Navier-Stokes solution generally predicts apparent disk vortex location, lateral contraction, and trajectory well.

7. The other theories (i.e., Comprehensive Analytical Method of Rotorcraft Aerodynamics and Dynamics–Johnson Aeronautics (CAMRAD/JA), Generalized Wake, and Rotor-Wake-Fuselage (RWF)) have difficulty predicting the upwash found on the leading edge of the rotor disk, particularly at $y/R = 0.8$. None of the theories (i.e., CAMRAD/JA, Generalized Wake, or RWF) accurately predict the position of the roll-up of tip vortices.

8. The CAMRAD/JA and RWF (with and without the effect of the fuselage) computer codes predict the trend of greatest downwash on the advancing side. The Generalized Wake predicts the greatest downwash on the retreating side, which is at variance with the experimental data.

NASA Langley Research Center
Hampton, VA 23681-0001
March 15, 1996

# References

1. Landgrebe, Anton J.; and Cheney, Marvin C., Jr.: Rotor Wakes—Key to Performance Prediction. *Aerodynamics of Rotary Wings*, AGARD-CP-111, 1973, pp. 1-1–1-19.

2. Gessow, Alfred; and Myers, Garry C., Jr.: *Aerodynamics of the Helicopter.* MacMillan Co., 1952. (Republished 1967 by F. Ungar Publ. Co.)

3. Gray, Robin B.: *An Aerodynamic Analysis of a Single-Bladed Rotor in Hovering and Low Speed Forward Flight as Determined From Smoke Studies of the Vorticity Distribution in the Wake.* Aeronaut. Eng. No. 356, Princeton Univ., Sept. 1956.

4. Landgrebe, Anton J.: An Analytical Method for Predicting Rotor Wake Geometry. *J. AHS*, vol. 14, no. 4, Oct. 1969, pp. 20–32.

5. Landgrebe, Anton J.: *An Analytical and Experimental Investigation of Helicopter Rotor Hover Performance and Wake Geometry Characteristics.* USAAMRDL Tech. Rep. 71-24, U.S. Army, June 1971. (Available from DTIC as AD 728 835.)

6. Egolf, T. A.; and Landgrebe, A. J.: *Helicopter Rotor Wake Geometry and Its Influence in Forward Flight—Volume 1: Generalized Wake Geometry and Wake Effect on Rotor Airloads and Performance.* NASA CR-3726, 1983.

7. Scully, Michael P.: *Computation of Helicopter Rotor Wake Geometry and Its Influence on Rotor Harmonic Airloads.* ASRL TR 178-1 (Contracts N00019-73-C-0378 and N00019-74-C-0321), MIT, Mar. 1975.

8. Bliss, Donald B.; and Wachspress, Daniel A.: *A Free Wake Method for Improved Prediction of Higher Harmonic Airloads.* CDI-85-1, Continuum Dynamics, Inc., Jan. 1985.

9. Steinhoff, John; and Ramachandran, K.: Free Wake Analysis of Compressible Rotor Flow Fields in Hover. *Proceedings of the 12th European Rotorcraft Forum*, Sept. 1986, pp. 20-1–20-20.

10. Quackenbush, Todd R.; Bliss, Donald B.; Wachspress, Daniel A.; Boschitsch, Alexander H.; and Chua, Kiat: *Computation of Rotor Aerodynamic Loads in Forward Flight Using a Full-Span Free Wake Analysis.* NASA CR-177611, 1990.

11. Rajagopalan, R. Ganesh; and Lim, Chin K.: Laminar Flow Analysis of a Rotor in Hover. *J. AHS*, vol. 36, Jan. 1991, pp. 12–23.

12. Zori, Laith A. J.: Three-Dimensional Navier-Stokes Calculations of a Rotor/Airframe Interaction in Forward Flight. M.S. Thesis, Iowa State Univ., 1991.

13. Elliott, Joe W.; Althoff, Susan L.; and Sailey, Richard H.: *Inflow Measurement Made With a Laser Velocimeter on a Helicopter Model in Forward Flight. Volume 1—Rectangular Planform Blades at an Advance Ratio of 0.15.* NASA TM-100541, AVSCOM TM-88-B-004, 1988.

14. Gorton, Susan Althoff; Poling, David R.; and Dadone, Leo: *Investigation of Blade-Vortex Interaction Using Laser Velocimetry and Pressure-Instrumented Rotor Blades. Volume 1—Advance Ratio of 0.2, Rotor Lift Coefficient Normalized by Solidity of 0.07, and Shaft Angle of 0°.* NASA TM-4570, ATCOM TR-94-A-002, 1995.

15. Cook, C. V.: The Structure of the Rotor Blade Tip Vortex. *Aerodynamics of Rotary Wings*, AGARD-CP-111, 1973.

16. Merzkirch, W.; and Gersten, K.: *Techniques of Flow Visualization*. AGARD-AG-302, Dec. 1987. (Available from DTIC as AD A194 291.)

17. FAA Technical Center: *Helicopter Full Scale Wake FLT Research Probe Airborne RAM*. TST 179.16, Apr. 1988. (Video Tape)

18. Larin, A.V.: Vortex Formation in Oblique Flow Around a Helicopter Rotor. *Uch. Zap.* (Tsentr. Aerogidrodinamicheskii Inst.), vol. 1, no. 3, 1970, pp. 115–122

19. Larin, A.: Vortex Wake Behind a Helicopter. *Aviatsiya i kosmonavtika*, vol. 3, 1973, pp. 32–33.

20. Lehman, August F.: Model Studies of Helicopter Rotor Flow Patterns in a Water Tunnel. *Proceedings of the 24th Annual National Forum of the American Helicopter Society*, May 1968. (Available as USAAVLABS TR-68-17.)

21. Landgrebe, A. J.; and Bellinger, E. D.: *An Investigation of the Quantitative Applicability of Model Helicopter Rotor Wake Patterns Obtained From a Water Tunnel—Final Report*. USAAMRDL-TR-71-69, Dec. 1971. (Available from DTIC as AD 739 946).

22. Jenks, Mark, Sr.; Ladone, Leo; and Gad-El-Hak, Mohamed: Towing Tank Flow Visualization Test of a Scale Model H-34 Rotor. *Proceedings of the 43rd Annual Forum of the American Helicopter Society*, vol. 2, 1987, pp. 825–838.

23. Tangler, James L.: Schlieren and Noise Studies of Rotors in Forward Flight. *Proceedings of the 33rd Annual National Forum of the American Helicopter Society*, May 1977, pp. 77.33-05-01–77.33-05-12.

24. Parthasarathy, S. P.; Cho, Y. I.; and Back, L. H.: Wide-Field Shadowgraph Flow Visualization of Tip Vortices Generated by a Helicopter Rotor. AIAA-85-1557, July 1985.

25. Norman, T. R.; and Light, J. S.: Rotor Tip Vortex Geometry Measurements Using the Wide-Field Shadowgraph Technique. *J. AHS*, vol 32, no. 2, June 1986, pp. 40–50.

26. Bagai, A.; Leishman, J. G.; and Samak, D. K.: A Study of Rotor Wake Development and Wake/Body Interactions in Hover. *Proceedings of the American Helicopter Society International Specialists' Meeting on Rotorcraft Basic Research*, 1991, pp. 41-1–41-17.

27. Light, Jeffrey S.; Norman, Thomas R.; and Frerking, Alexandra A.: Application of the Wide-Field Shadowgraph Technique to Helicopters in Forward Flight. *Proceedings of the 46th Annual Forum of the American Helicopter Society*, 1990, pp. 1207–1220.

28. Leishman, J. G.; and Bagai, A.: Fundamental Studies of Rotor Wakes in Low Speed Forward Flight Using Wide-Field Shadowgraphy. AIAA-91-3232, Sept. 1991.

29. Brand, A. G.; Komerath, N. M.; and McMahon, H. M.: Results From Laser Sheet Visualization of a Periodic Rotor Wake. AIAA-88-0192, Jan. 1988.

30. Leighty, Bradley D.; Rhodes, David B.; Franke, John M.; and Jones, Stephen B.: *A Synchronous Strobed Laser Light Sheet for Rotor Flow Visualization*. NASA TM-4266, 1991.

31. Wood, T. L.; Brand, A. G.; and Elliott, J. W.: An Experimental Investigation of Rotor Blade Airloads and Wake Structure at High Advance Ratio. *Proceedings of the 46th Annual Forum and Technology Display of the American Helicopter Society*, May 1990, p. 14.

32. Gentry, Garl L., Jr.; Quinto, P. Frank; Gatlin, Gregory M.; and Applin, Zachary T.: *The Langley 14- by 22-Foot Subsonic Tunnel—Description, Flow Characteristics, and Guide for Users*. NASA TP-3008, 1990.

33. Phelps, Arthor E., III; and Berry, John D.: *Description of the U.S. Army Small-Scale 2-Meter Rotor Test System*. NASA TM-87762, AVSCOM TM-86-B-4, 1987.

34. Berry, John D.; and Althoff, Susan L.: *Computing Induced Velocity Perturbations Due to a Helicopter Fuselage in a Free Stream*. NASA TM-4113, AVSCOM TR-89-B-001, 1989.

35. Kudlinski, Robert A.; and Park, Stephen K.: *Digital Enhancement of Flow Field Images*. NASA TP-2770, 1988.

36. Lamar, John E.; and Johnson, Thomas D.: *Sensitivity of F-106B Leading-Edge-Vortex Images to Flight and Vapor-Screen Parameters*. NASA TP-2818, 1988.

37. Rae, William H., Jr.; and Pope, Alan: *Low-Speed Wind Tunnel Testing*, Second ed. John Wiley & Sons, Inc., 1984.

38. Hoad, Danny R.: *Rotor Induced-Inflow-Ratio Measurements and CAMRAD Calculations*. NASA TP-2946, AVSCOM TM-89-B-010, 1990.

39. Berry, John D: *RWF Rotor-Wake-Fuselage Code Software Reference Guide*. NASA TM-104078, AVSCOM TR-91-B-008, 1991.

40. Patankar, Suhas V.: *Numerical Heat Transfer and Fluid Flow*. Hemisphere Publ. Corp., 1980.

41. Rajagopalan, R. G.; and Fanucci, J. B.: Finite Difference Model for Verticle Axis Wind Turbines. *J. Propuls. & Power*, vol. 1, Nov.–Dec. 1985, pp. 432–436.

42. Zori, Laith A. J.; Mathur, Sanjay R.; and Rajagopalan, R. G.: Three-Dimensional Calculations of Rotor-Airframe Interaction Forward Flight. *Proceedings of the 48th Annual Forum of the American Helicopter Society*, 1992, pp. 489–512.

43. Loiselle, J. W.: Generalized Helicopter Rotor Performance Predictions. M.S. Thesis, Naval Postgraduate School, Sept. 1977.

44. Johnson, Wayne: *A Comprehensive Analytical Model of Rotorcraft Aerodynamics and Dynamics—Johnson Aeronautics Version. Volume II: User's Manual*. CAMRAD/JA, Johnson Aeronautics (Palo Alto, CA), 1988.

45. Van Gaasbeek, J. R.: *Rotorcraft Flight Simulation Computer Program C81 With DATAMAP Interface. Volume 1—User's Manual*. BHT-699-099-111-VOL-1, USAAVRADCOM-TR-80-D-38A, Oct. 1981. (Available from DTIC as AD A108 246.)

46. Egolf, T. Alan; and Edwards, Donna: *Users Manual for a Stand-Alone Version of the UTRC Generalized Wake Module*. UTRC R83-912666-57, June 1983.

47. Egolf, T. Alan; and Landgrebe, Anton J.: *Helicopter Rotor Wake Geometry and Its Influence in Forward Flight. Volume II—Wake Geometry Charts*. NASA CR-3727, 1983.

48. Berry, John Donaldson: A Method of Computing the Aerodynamic Interactions of a Rotor-Fuselage Configuration in Forward Flight. Ph.D. Thesis, Georgia Inst. Technol., 1990.

49. Hess, J. L.; and Smith, A. M. O.: *Calculation of Potential Flow About Arbitrary Bodies. Progress in Aeronautical Sciences, Volume 8*, D. Küchemann, P. Carrière, B. Etkin, W. Fiszdon, N. Rott, J. Smolderen, I. Tani, and W. Wuest, eds., Pergamon Press, Inc., 1967, pp. 1–138.

50. Landgrebe, Anton J.; Taylor, Robert B.; Egolf, T. Alan; and Bennett, John C.: Helicopter Airflow and Wake Characteristics for Low Speed and Hovering Flight From Rocket Interference Investigations. *Proceedings of the 37th Annual Forum of the American Helicopter Society*, May 1981, pp. 51–65.

51. Elliott, Joe W.; Althoff, Susan L.; and Sailey, Richard H.: *Inflow Measurement Made With a Laser Velocimeter on a Helicopter Model in Forward Flight. Volume II—Rectangular Planform Blades at an Advance Ratio of 0.23*. NASA TM-100542, AVSCOM TM-88-B-005, 1988.

52. Tung, C.; Pucci, S. L.; Caradonna, F. X.; and Morse, H. A.: The Structure of Trailing Vortices Generated by Model Rotor Blades. *Vertica*, vol. 7, no. 1, 1983, pp. 33–43.

53. Rorke, J. B.; Moffitt, R. C.; and Ward, J. F.: Wind Tunnel Simulation of Full Scale Vortices. Preprint No. 623, AHS, May 1972.

54. Chigier, N. A.; and Corsiglia, V. R.: *Tip Vortices—Velocity Distributions*. Preprint No. 522, AHS, May 1971.

55. Swanson, Alexandra A.; and Light, Jeffrey S.: Shadowgraph Flow Visualization of Isolated Tiltrotor and Rotor/Wing Wakes. *Proceedings of the 48th Annual Forum of the American Helicopter Society*, 1992, pp. 1323–1344.

56. Thompson, T. L.; Kwon, O. J.; Kemnitz, J. L.; Komerath, N. M.; and Gray, R. B.: Tip Vortex Core Measurements on a Hovering Model Rotor. AIAA-87-0209, Jan. 1987.

57. Sullivan, John P.: *An Experimental Investigation of Vortex Rings and Helicopter Rotor Wakes Using a Laser Doppler Velocimeter*. Tech. Rep. No. 183 (Contract No. N00019-72-C-0450), MIT, June 1973. (Available from DTIC as AD 778 768.)

58. Querin, Osvaldo M.: Flow Visualisation of a Small Diameter Rotor Operating at High Rotational Speeds With Blades at Small Pitch Angles. *Proceedings of the American Helicopter Society International Specialists' Meeting on Rotorcraft Basic Research*, 1991, pp. 25-1–25-6.

59. Biggers, James C.; Lee, Albert; Orloff, Kenneth L.; and Lemmer, Opal J.: Measurements of Helicopter Rotor Tip Vortices. *Proceedings of the 33rd Annual National Forum of the American Helicopter Society*, May 1977.

60. Bruce, Robert A.; Hess, Robert W.; and Rivera, Jose A., Jr.: A Vapor Generator for Transonic Flow Visualization. NASA TM-101670, 1989.

61. Betz, A.: *Behavior of Vortex Systems*. NACA TM 713, 1933.

62. Rossow, V. J.: *On the Inviscid Rolled-Up Structure of Lift-Generated Vortices*. NASA TM X-62224, 1973.

63. Favier, D.; Nsi Mba, M.; Barbi, C.; and Maresca, C.: A Free Wake Analysis for Hovering Rotors and Advancing Propellers. *Proceedings of the 11th European Rotorcraft Forum*, Sept. 1985.

64. Miller, R. H.: *Simplified Free Wake Analyses for Rotors*. ASRL TR 194-3, Dep. Aeron. & Astron., MIT, Aug. 1981.

65. Mueller, Reinert H. G.: Special Vortices at a Helicopter Rotor Blade. *J. AHS*, vol. 35, Oct. 1990, pp. 16–22.

66. Kim, Jaimoo; Komerath, Narayanan; and Liou, Shiuh-Guang: Vorticity Concentration at the Edge of the Inboard Vortex Sheet. *Proceedings of the 49th Annual National Forum of the American Helicopter Society*, 1993, pp. 585–595.

### Table 1. Limiting Minimum Uncertainty

#### (a) Lateral laser light sheet

| $x/R$ | Uncertainty for— | | | | | | | |
|---|---|---|---|---|---|---|---|---|
| | $y$, in. | | $y/R$ | | $z$, in. | | $z/R$ | |
| | Min. | Max. | Min. | Max. | Min. | Max. | Min. | Max. |
| 1.0 | ±0.074 | ±0.104 | ±0.002 | ±0.003 | ±0.042 | ±0.058 | ±0.001 | ±0.002 |
| 1.5 | ±.067 | ±.074 | ±.002 | ±.003 | ±.042 | ±.051 | ±.001 | ±.002 |
| 2.0 | ±.074 | ±.118 | ±.002 | ±.003 | ±0.42 | ±.058 | ±.001 | ±.002 |
| 2.5 | ±.104 | ±.173 | ±.003 | ±.005 | ±.048 | ±.073 | ±.001 | ±.002 |
| 3.0 | ±.134 | ±.152 | ±.004 | ±.004 | ±.076 | ±.095 | ±.002 | ±.003 |
| 3.5 | ±.119 | ±.201 | ±.004 | ±.006 | ±.069 | ±.095 | ±.002 | ±.003 |
| 4.0 | ±.111 | ±.173 | ±.003 | ±.005 | ±.062 | ±.095 | ±.002 | ±.003 |

#### (b) Longitudinal laser light sheet

| $y/R$ | Camera position | Uncertainty for— | | | | | | | |
|---|---|---|---|---|---|---|---|---|---|
| | | $x$, in. | | $x/R$ | | $z$, in. | | $z/R$ | |
| | | Min. | Max. | Min. | Max. | Min. | Max. | Min. | Max. |
| −0.8 | Port | ±0.052 | ±0.093 | ±0.002 | ±0.004 | ±0.038 | ±0.055 | ±0.001 | ±0.002 |
| −.3 | Port | ±.041 | ±.073 | ±.001 | ±.002 | ±.035 | ±.047 | ±.001 | ±.001 |
| .3 | Port | ±.048 | ±.076 | ±.001 | ±.002 | ±.038 | ±.055 | ±.001 | ±.002 |
| .3 | Starboard | ±.041 | ±.052 | ±.001 | ±.002 | ±.038 | ±.051 | ±.001 | ±.002 |
| .8 | Port | ±.059 | ±.076 | ±.002 | ±.002 | ±.045 | ±.055 | ±.001 | ±.002 |
| .8 | Starboard | ±.041 | ±.045 | ±.001 | ±.001 | ±.035 | ±.037 | ±.001 | ±.001 |

Table 2. Subjectivity Error of Tip Vortex Location

| y/R | Camera position | Subjectivity error for— | | | | | | | |
|---|---|---|---|---|---|---|---|---|---|
| | | x, in. | | x/R | | z, in. | | z/R | |
| | | Min. | Max. | Min. | Max. | Min. | Max. | Min. | Max. |
| −0.8 | Port | ±0.11 | ±0.59 | ±0.003 | ±0.017 | ±0.09 | ±0.18 | ±0.003 | ±0.005 |
| −.3 | Port | ±.09 | ±.46 | ±.003 | ±.013 | ±.09 | ±.16 | ±.003 | ±.005 |
| .3 | Port | ±.10 | ±.48 | ±.003 | ±.014 | ±.09 | ±.18 | ±.003 | ±.005 |
| .3 | Starboard | ±.09 | ±.33 | ±.003 | ±.010 | ±.09 | ±.17 | ±.003 | ±.005 |
| .8 | Port | ±.13 | ±.48 | ±.004 | ±.014 | ±.11 | ±.18 | ±.003 | ±.005 |
| .8 | Starboard | ±.09 | ±.28 | ±.003 | ±.008 | ±.09 | ±.12 | ±.003 | ±.004 |
| −.8 upper tip vortex | Port | | ±.34 | | ±.010 | | ±.15 | | ±.005 |
| .8 upper tip vortex | Port | | ±.28 | | ±.008 | | ±.15 | | ±.005 |

Table 3. Total Uncertainty of Tip Vortex Location

[Longitudinal laser light sheet]

| y/R | Camera position | Total uncertainty for— | | | | | | | |
|---|---|---|---|---|---|---|---|---|---|
| | | x, in. | | x/R | | z, in. | | z/R | |
| | | Min. | Max. | Min. | Max. | Min. | Max. | Min. | Max. |
| −0.8 | Port | ±0.308 | ±0.661 | ±0.009 | ±0.020 | ±0.308 | ±0.347 | ±0.009 | ±0.010 |
| −.3 | Port | ±.299 | ±.424 | ±.009 | ±.013 | ±.308 | ±.335 | ±.009 | ±.010 |
| .3 | Port | ±.303 | ±.562 | ±.009 | ±.017 | ±.308 | ±.347 | ±.009 | ±.010 |
| .3 | Starboard | ±.299 | ±.438 | ±.009 | ±.013 | ±.308 | ±.341 | ±.009 | ±.010 |
| .8 | Port | ±.317 | ±.562 | ±.009 | ±.017 | ±.315 | ±.377 | ±.009 | ±.011 |
| .8 | Starboard | ±.299 | ±.400 | ±.009 | ±.012 | ±.308 | ±.317 | ±.009 | ±.009 |
| −.8 upper tip vortex | Port | ±.309 | ±.342 | ±.009 | ±.010 | ±.308 | ±.333 | ±.009 | ±.010 |
| .8 upper tip vortex | Port | ±.317 | ±.332 | ±.009 | ±.010 | ±.331 | ±.333 | ±.010 | ±.010 |

#### Table 4. Total Uncertainty of Apparent Disk Vortex Location

[Longitudinal laser light sheet]

| x/R | μ | Total uncertainty for— | | | | | | | |
|---|---|---|---|---|---|---|---|---|---|
| | | y, in. | | y/R | | z, in. | | z/R | |
| | | Min. | Max. | Min. | Max. | Min. | Max. | Min. | Max. |
| 1.0 | 0.15 | ±0.379 | ±0.425 | ±0.011 | ±0.013 | ±0.335 | ±0.338 | ±0.010 | ±0.010 |
| 1.0 | .23 | ±.379 | ±.454 | ±.012 | ±.013 | ±.315 | ±.353 | ±.009 | ±.010 |
| 1.5 | .15 | ±.359 | ±.418 | ±.011 | ±.012 | ±.325 | ±.362 | ±.010 | ±.011 |
| 1.5 | .23 | ±.347 | ±.606 | ±.010 | ±.018 | ±.361 | ±.400 | ±.011 | ±.012 |
| 2.0 | .15 | ±.354 | ±.415 | ±.010 | ±.012 | ±.315 | ±.324 | ±.009 | ±.010 |
| 2.0 | .23 | ±.418 | ±.481 | ±.012 | ±.014 | ±.416 | ±.389 | ±.012 | ±.011 |
| 2.5 | .15 | ±.454 | ±.512 | ±.013 | ±.015 | ±.374 | ±.396 | ±.011 | ±.012 |
| 2.5 | .23 | ±.425 | ±.686 | ±.013 | ±.020 | ±.345 | ±.396 | ±.010 | ±.012 |
| 3.0 | .15 | ±.470 | ±.496 | ±.014 | ±.015 | ±.345 | ±.355 | ±.010 | ±.010 |
| 3.0 | .23 | ±.419 | ±.426 | ±.012 | ±.013 | ±.391 | ±.451 | ±.012 | ±.013 |
| 3.5 | .15 | ±.421 | ±.529 | ±.012 | ±.016 | ±.360 | ±.395 | ±.011 | ±.012 |
| 3.5 | .23 | ±.412 | ±.624 | ±.012 | ±.018 | ±.417 | ±.595 | ±.012 | ±.018 |
| 4.0 | .15 | ±.413 | ±.489 | ±.012 | ±.014 | ±.325 | ±.371 | ±.010 | ±.011 |
| 4.0 | .23 | ±.519 | ±.567 | ±.015 | ±.017 | ±.438 | ±.604 | ±.013 | ±.018 |

#### Table 5. Measurement Uncertainty for Particle Void Radius

(a) Lateral laser light sheet

| x/R | Uncertainty for— | | | |
|---|---|---|---|---|
| | $r_v$, in. | | $r_{v/c}$ | |
| | Min. | Max. | Min. | Max. |
| 1.0 | ±0.10 | ±0.15 | ±0.004 | ±0.006 |
| 1.5 | ±.09 | ±.15 | ±.003 | ±.006 |
| 2.0 | ±.10 | ±.17 | ±.004 | ±.007 |
| 2.5 | ±.14 | ±.25 | ±.005 | ±.010 |
| 3.0 | ±.18 | ±.22 | ±.007 | ±.008 |
| 3.5 | ±.16 | ±.29 | ±.006 | ±.011 |
| 4.0 | ±.15 | ±.25 | ±.006 | ±.010 |

(b) Longitudinal laser light sheet

| y/R | Uncertainty for— | |
|---|---|---|
| | $r_v$, in. | $r_{v/c}$ |
| −0.8 | ±0.07 | ±0.003 |
| −.3 | ±.06 | ±.002 |
| .3 | (a) | (a) |
| .8 | ±.08 | ±.003 |

[a]Not applicable.

#### Table 6. Total Uncertainty for Particle Void Radius Measurement

(a) Lateral laser light sheet

| x/R | Total uncertainty for— | | | |
|---|---|---|---|---|
| | $r_v$, in. | | $r_{v/c}$ | |
| | Min. | Max. | Min. | Max. |
| 1.0 | ±0.160 | ±0.196 | ±0.061 | ±0.075 |
| 1.5 | ±.155 | ±.196 | ±.059 | ±.075 |
| 2.0 | ±.160 | ±.211 | ±.061 | ±.081 |
| 2.5 | ±.188 | ±.280 | ±.072 | ±.107 |
| 3.0 | ±.219 | ±.253 | ±.084 | ±.097 |
| 3.5 | ±.203 | ±.316 | ±.078 | ±.121 |
| 4.0 | ±.196 | ±.280 | ±.075 | ±.107 |

(b) Longitudinal laser light sheet

| y/R | Total uncertainty for— | |
|---|---|---|
| | $r_v$, in. | $r_{v/c}$ |
| −0.8 | ±0.144 | ±0.055 |
| −.3 | ±.138 | ±.053 |
| .3 | (a) | (a) |
| .8 | ±.148 | ±.057 |

[a]Not applicable.

Table 7. Total Uncertainty of Convective Velocity

[Longitudinal laser light sheet]

| $y/R$ | $\mu$ | Total uncertainty for— | | | | | |
|---|---|---|---|---|---|---|---|
| | | $\Delta V$, ft/sec | | | $\Delta V/V_\infty$ | | |
| | | CW | CCW | Upper | CW | CCW | Upper |
| −0.8 | 0.15 | 1.32 | 2.58 | 1.46 | 0.014 | 0.028 | 0.016 |
| −.8 | .23 | 1.52 | 1.99 | (a) | .011 | .014 | (a) |
| −.3 | .15 | .58 | (a) | | .006 | (a) | |
| −.3 | .23 | .85 | 1.81 | | .006 | .013 | |
| .3 | .15 | .50 | 1.24 | | .005 | .013 | |
| .3 | .23 | .79 | 1.67 | | .006 | .012 | |
| .8 | .15 | 3.00 | 1.61 | 1.22 | .032 | .017 | .013 |
| .8 | .23 | .47 | 1.62 | 1.19 | .003 | .011 | .008 |

[a]Not applicable.

Table 8. Rotor Performance

| Parameter | Experiment | CAMRAD/JA | 3-D Navier-Stokes |
|---|---|---|---|
| $\mu = 0.15$ | | | |
| Power, hp . . . . . . . . . . . . . . . . . . | 7.9 | 6.4 | (a) |
| Shaft angle of attack, deg. . . . . . . | −3.0 | −3.0 | −3.0 |
| Coning angle, deg . . . . . . . . . . . . | 1.5 | 1.80 | 1.33 |
| Longitudinal cyclic angle, deg. . . | 1.99 | 0.75 | 2.45 |
| Lateral cyclic angle, deg . . . . . . . | −1.39 | −3.33 | −1.94 |
| Collective angle, deg . . . . . . . . . . | 6.55 | 7.87 | 7.76 |
| $\mu = 0.23$ | | | |
| Power, hp . . . . . . . . . . . . . . . . . . | 8.4 | 7.6 | (a) |
| Shaft angle of attack, deg. . . . . . . | −3.0 | −3.0 | −3.0 |
| Coning angle, deg . . . . . . . . . . . . | 1.5 | 1.68 | 1.33 |
| Longitudinal cyclic angle, deg. . . | 3.23 | 3.64 | 3.60 |
| Lateral cyclic angle, deg . . . . . . . | −1.07 | −1.71 | −1.69 |
| Collective angle, deg . . . . . . . . . . | 6.47 | 7.30 | 7.26 |

[a]Not applicable.

Table 9. Apparent Disk Vortex Trajectory

| Parameter, deg | Experiment | 3-D Navier-Stokes |
|---|---|---|
| $\mu = 0.15$ | | |
| Lateral contraction—advancing side . . . . . . . | −2.53 | −1.28 |
| Lateral contraction—retreating side. . . . . . . . | −1.03 | 1.25 |
| Vertical trajectory—advancing side . . . . . . . . | −5.52 | −4.73 |
| Vertical trajectory—retreating side . . . . . . . . | −2.84 | −3.02 |
| $\mu = 0.23$ | | |
| Lateral contraction—advancing side . . . . . . . | −3.99 | −1.67 |
| Lateral contraction—retreating side. . . . . . . . | −0.49 | 1.39 |
| Vertical trajectory—advancing side . . . . . . . . | −4.82 | −1.32 |
| Vertical trajectory—retreating side . . . . . . . . | −0.67 | −0.45 |

## Table 10. Tip Vortex Vertical Skew Angle

### (a) μ = 0.15

| Tip vortex | Angle, deg, for y/R— | | | |
|---|---|---|---|---|
| | −0.8 | −0.3 | 0.3 | 0.8 |
| Experiment | | | | |
| Lower CW | −12.00 | −7.17 | −14.10 | −1.87 |
| Lower CCW | −14.21 | (a) | −13.14 | −8.90 |
| Upper | 7.49 | (a) | (a) | 3.11 |
| Theory | | | | |
| CAMRAD/JA CW | −16.60 | −15.81 | −18.93 | −20.27 |
| CAMRAD/JA CCW | −7.35 | −15.85 | −16.64 | −9.66 |
| CAMRAD/JA upper | 3.54 | (a) | (a) | −0.76 |
| Generalized Wake CW | −3.23 | −3.37 | −4.18 | −2.16 |
| Generalized Wake CCW | −7.01 | −10.47 | −8.36 | −5.21 |
| RWF CW; fuselage | −8.37 | −7.01 | −12.64 | −14.88 |
| RWF CCW; fuselage | −5.80 | −5.39 | −5.29 | −11.40 |
| RWF CW; no fuselage | −8.97 | −5.38 | −11.28 | −15.37 |
| RWF CCW; no fuselage | −5.43 | −6.18 | −5.85 | −10.70 |

[a]Insufficient data.

### (b) μ = 0.23

| Tip vortex | Angle, deg, for y/R— | | | |
|---|---|---|---|---|
| | −0.8 | −0.3 | 0.3 | 0.8 |
| Experiment | | | | |
| Lower CW | −4.98 | −2.60 | −9.27 | −5.59 |
| Lower CCW | −5.19 | −5.11 | −6.66 | −4.78 |
| Upper | (a) | (a) | (a) | 3.85 |
| Theory | | | | |
| CAMRAD/JA CW | −6.55 | −5.78 | −9.91 | −9.68 |
| CAMRAD/JA CCW | −2.39 | −8.18 | −6.06 | −7.56 |
| CAMRAD/JA upper | (a) | (a) | (a) | 0.69 |
| Generalized Wake CW | −1.87 | −1.86 | −1.53 | −1.25 |
| Generalized Wake CCW | −3.98 | −4.83 | −3.26 | −2.64 |
| RWF CW; fuselage | −3.74 | −3.23 | −7.76 | −7.95 |
| RWF CCW; fuselage | −2.85 | −1.29 | −3.33 | −6.58 |
| RWF CW; no fuselage | −4.25 | −1.24 | −5.82 | −8.03 |
| RWF CCW; no fuselage | −2.33 | −1.42 | −3.76 | −5.53 |

[a]Insufficient data.

Table 11. Convective Velocity

| y/R | Tip vortex— | | | | | |
| | Lower CW | | Lower CCW | | Upper | |
| | $V$, ft/sec | $V/V_\infty$ | $V$, ft/sec | $V/V_\infty$ | $V$, ft/sec | $V/V_\infty$ |
|---|---|---|---|---|---|---|
| $\mu = 0.15$ | | | | | | |
| −0.8 | 100 | 1.08 | 114 | 1.23 | 82 | 0.88 |
| −.3 | 94 | 1.01 | (a) | (a) | (a) | (a) |
| .3 | 93 | 1.00 | 98 | 1.06 | (a) | (a) |
| .8 | 98 | 1.05 | 78 | 0.84 | 66 | 0.71 |
| $\mu = 0.23$ | | | | | | |
| −0.8 | 146 | 1.02 | 149 | 1.04 | (a) | (a) |
| −.3 | 138 | 0.96 | 131 | 0.92 | (a) | (a) |
| .3 | 145 | 1.02 | 136 | .95 | (a) | (a) |
| .8 | 150 | 1.05 | 143 | .99 | 105 | 0.74 |

[a]Insufficient data.

Table 12. Convective Angle

| y/R | Tip vortex— | | | | | | | | |
| | Lower CW | | | Lower CCW | | | Upper | | |
| | Angle, deg | $u$, ft/sec | $w$, ft/sec | Angle, deg | $u$, ft/sec | $w$, ft/sec | Angle, deg | $u$, ft/sec | $w$, ft/sec |
|---|---|---|---|---|---|---|---|---|---|
| $\mu = 0.15$ | | | | | | | | | |
| −0.8 | −10.51 | 98 | −18 | −12.92 | 111 | −25 | 9.04 | 81 | 13 |
| −.3 | −7.10 | 93 | −12 | (a) | (a) | (a) | (a) | (a) | (a) |
| .3 | −12.07 | 91 | −19 | −11.97 | 96 | −20 | (a) | (a) | (a) |
| .8 | −0.08 | 98 | 0 | −9.96 | 77 | −13 | 2.84 | 66 | 3 |
| $\mu = 0.23$ | | | | | | | | | |
| −0.8 | −4.90 | 145 | −12 | −5.03 | 148 | −13 | (a) | (a) | (a) |
| −.3 | −2.53 | 138 | −6 | −4.84 | 131 | −11 | (a) | (a) | (a) |
| .3 | −7.93 | 144 | −20 | −7.17 | 135 | −17 | (a) | (a) | (a) |
| .8 | −3.13 | 150 | −8 | −5.00 | 142 | −12 | 3.32 | 105 | 6 |

[a]Insufficient data.

Table 13. Reported Vortex Core Sizes

| Reference | Airfoil | Type | μ | Instrument | $r_v/c$ | $C_T$ | Wake age, deg |
|---|---|---|---|---|---|---|---|
| 15 | NACA 0012 | Rotor | 0 | Hot wire | 0.01–0.09 | 0.0011–0.0020 | 100–400 |
| 51 | NACA 0012 | Rotor | 0 | Hot wire | .04 | .0018–.0059 | 50–76 |
| 52 | NACA 0015 | Static | (a) | Hot wire | .03–.05 | (a) | 0 |
| 53 | NACA 0015 | Static | (a) | Hot wire | .07 | (a) | (b) |
| 24 | NACA 0015 | Rotor | 0 | Shadowgraph | .06 | .0090 | (b) |
| 25 | SC1095 | Rotor | 0 | Shadowgraph | .04 | .0015–.0075 | (b) |
| 25 | SC1095R8 | Tiltrotor | 0 | Shadowgraph | .03 | .0048–.0103 | (b) |
| 26 | NASA RC(3)10/(4)10 | Rotor | 0 | Shadowgraph | .02 | .0088 | 0–300 |
| 28 | NASA RC(3)10/(4)10 | Rotor | .05–.15 | Shadowgraph | .02 | .0088 | 0–360 |
| 54 | NACA 64A223 | Tiltrotor | 0 | Shadowgraph | .03–.13 | .0049–.0159 | 51 |
| 55 | NACA 0012 | Rotor | 0 | Smoke | .01–.16 | .0022; .0057 | 30–570 |
| 56 | NACA 0012 | Rotor | 0 | Smoke | .09–.30 | .0039 | 60–540 |
| 57 | NACA 0012 | Rotor | .04; .08 | Smoke | .16–.25 | (b) | 0–1080 |
| Present | NACA 0012 | Rotor | .15; .23 | Smoke | .10–.35 | .0064 | 40–360 |
| 58 | NACA 0012 | Rotor | .18 | (c) | .08–.15 | .0043; .0048 | 70–90 |

[a]Not applicable.
[b]Not cited.
[c]Laser velocimeter.

Table 14. Tip Vortex and ISV Vertical Skew Angle

| | Angle, deg, for— | | | |
|---|---|---|---|---|
| $y/R$ | Lower CW | ISV CCW | Lower CCW | ISV CW |
| μ = 0.15 | | | | |
| −0.8 | −11.92 | −10.21 | −14.52 | −14.45 |
| −.3 | −3.33 | −3.61 | (a) | (a) |
| μ = 0.23 | | | | |
| −0.8 | −4.43 | −3.49 | (a) | (a) |
| −.3 | −1.04 | −0.56 | (a) | (a) |

[a]Insufficient data.
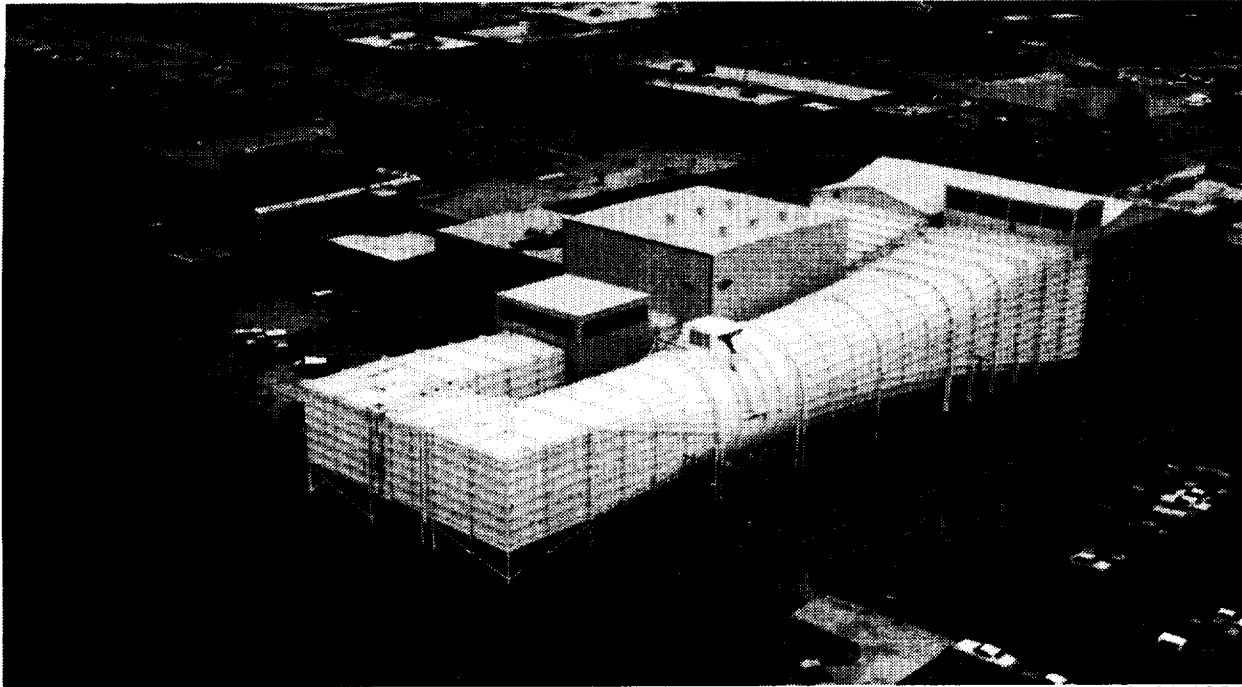
(a) Aerial view.

L-81-1354
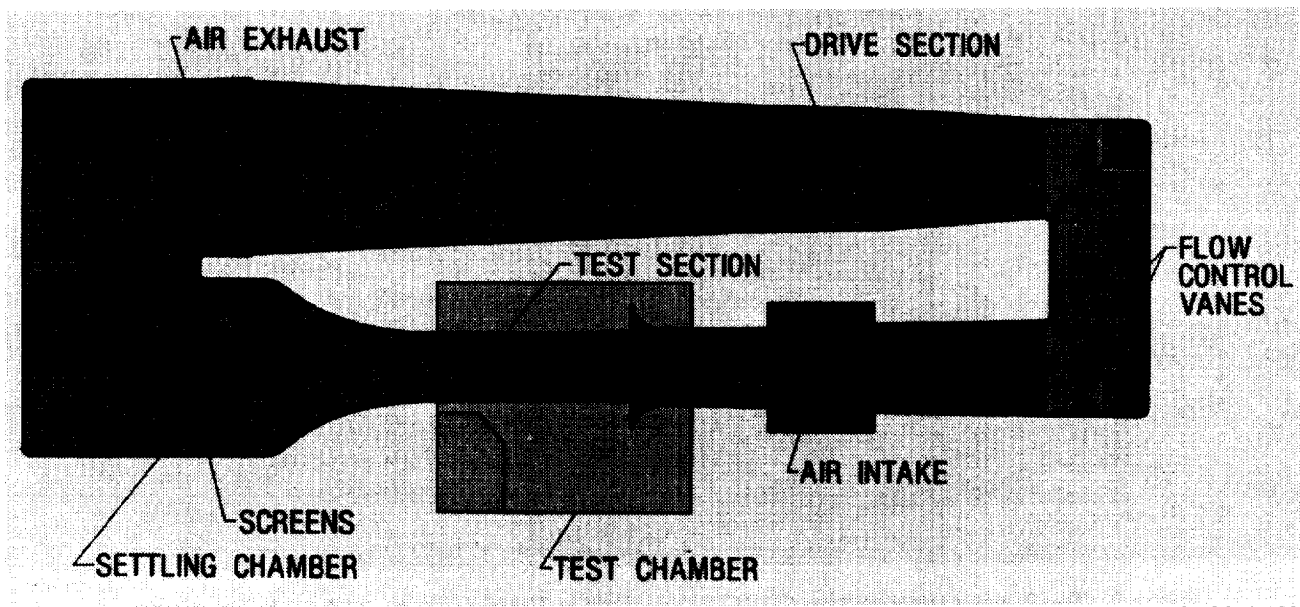


(b) Diagram.

L-83-7553

Figure 1. The Langley 14- by 22-Foot Subsonic Tunnel.

27
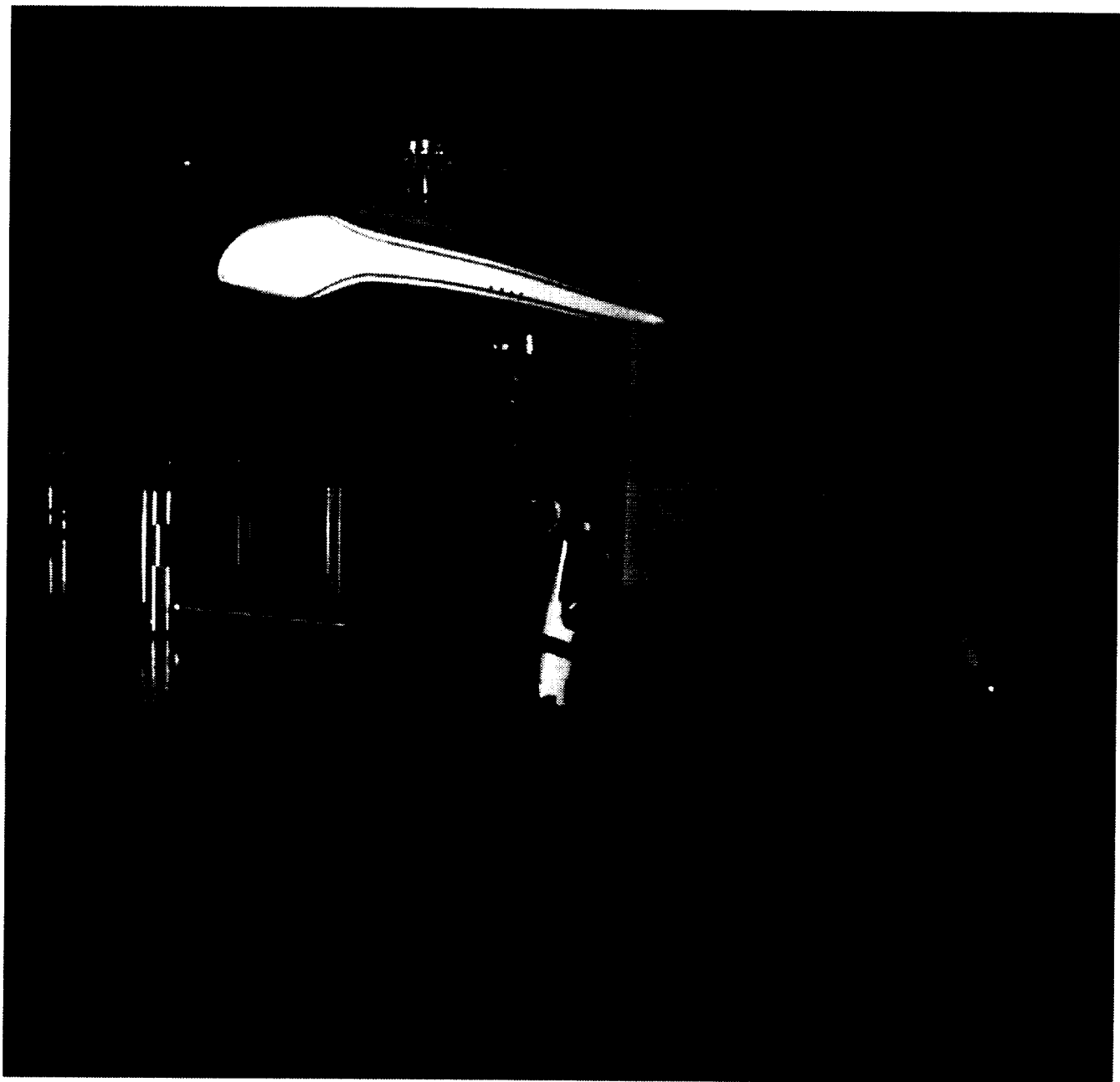
L-91-01441

Figure 2. The 2-meter rotor system (2MRTS) mounted in Langley 14- by 22-Foot Subsonic Tunnel.
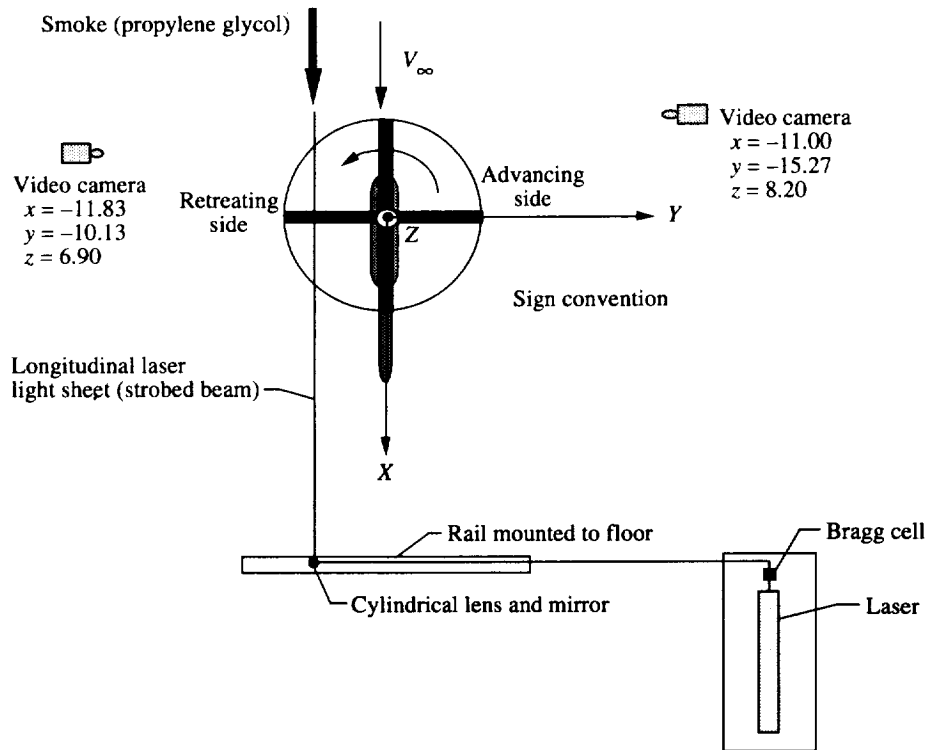
Figure 3. Experimental setup for longitudinal laser light sheet. Video camera location coordinates are in feet.
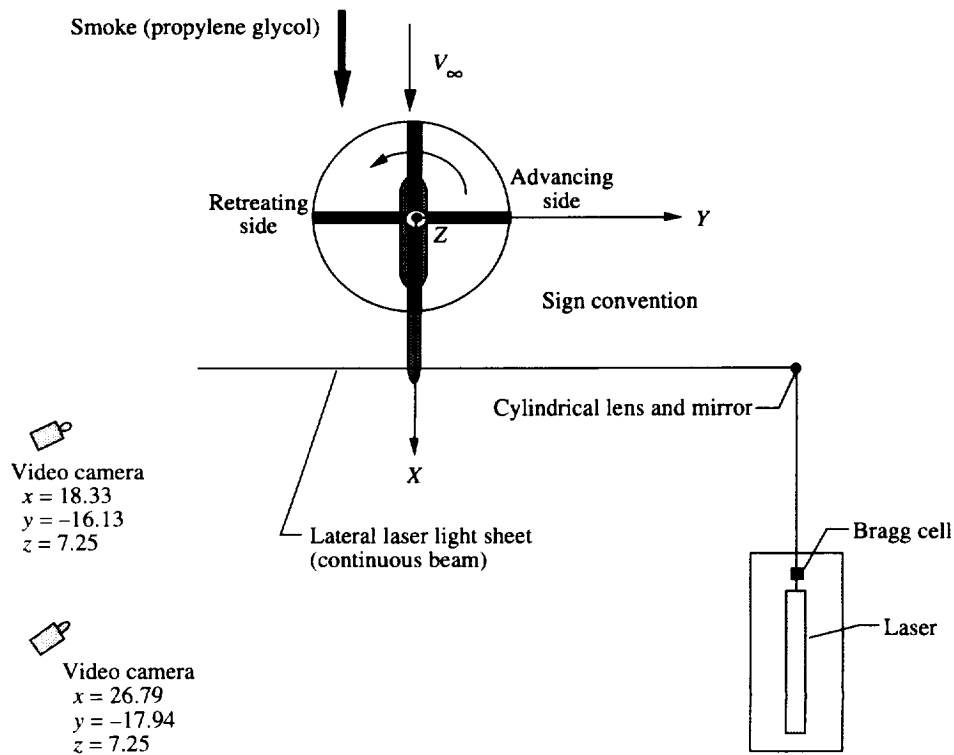


Figure 4. Experimental setup for lateral laser light sheet. Video camera location coordinates are in feet.

**29**
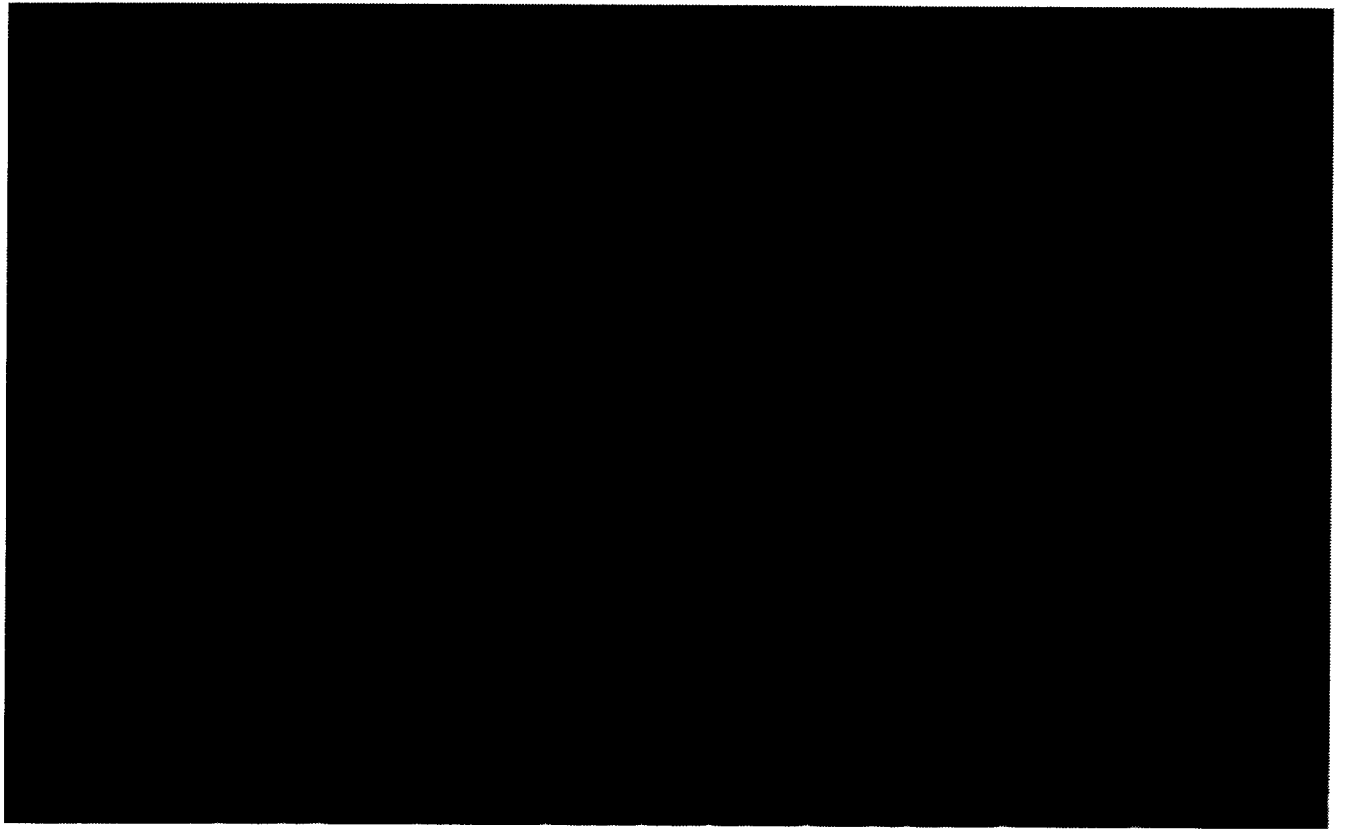
Figure 5. Reference locator point grid superimposed on data.
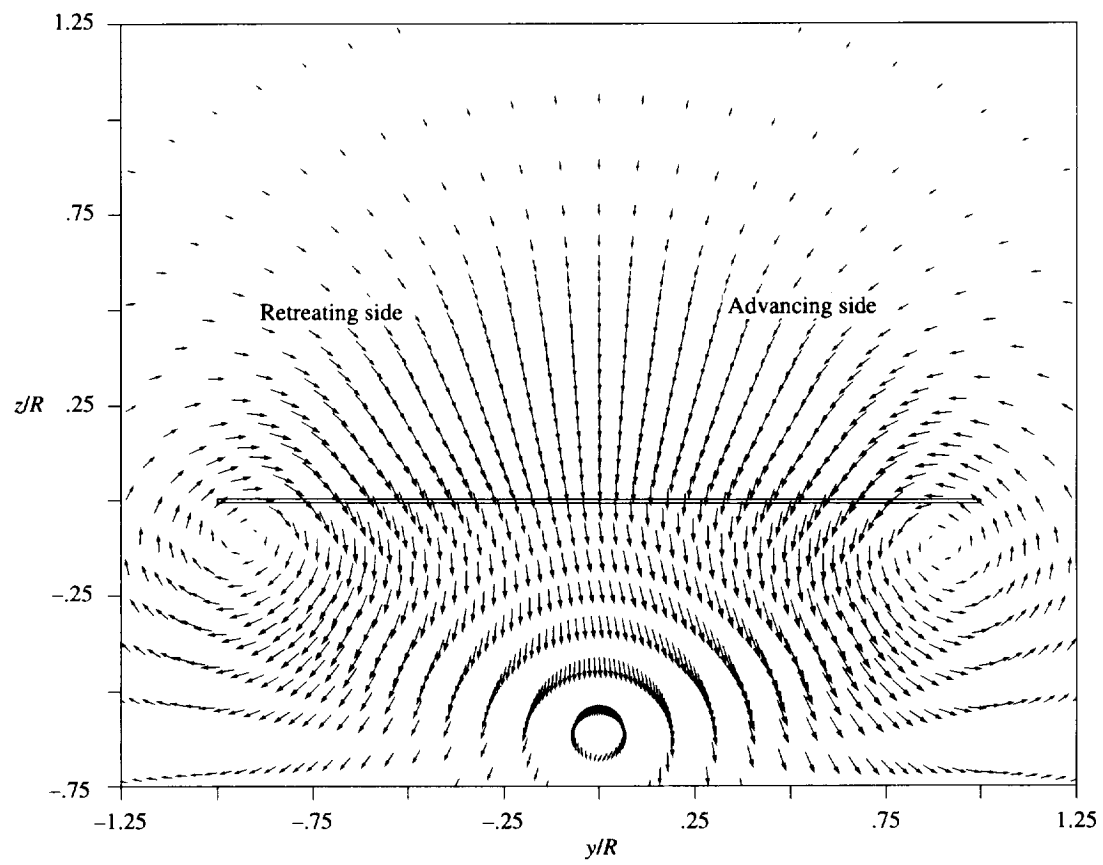
Figure 6. The 3-D Navier-Stokes velocity vector plot at $x/R = 1.88$ and $\mu = 0.15$.
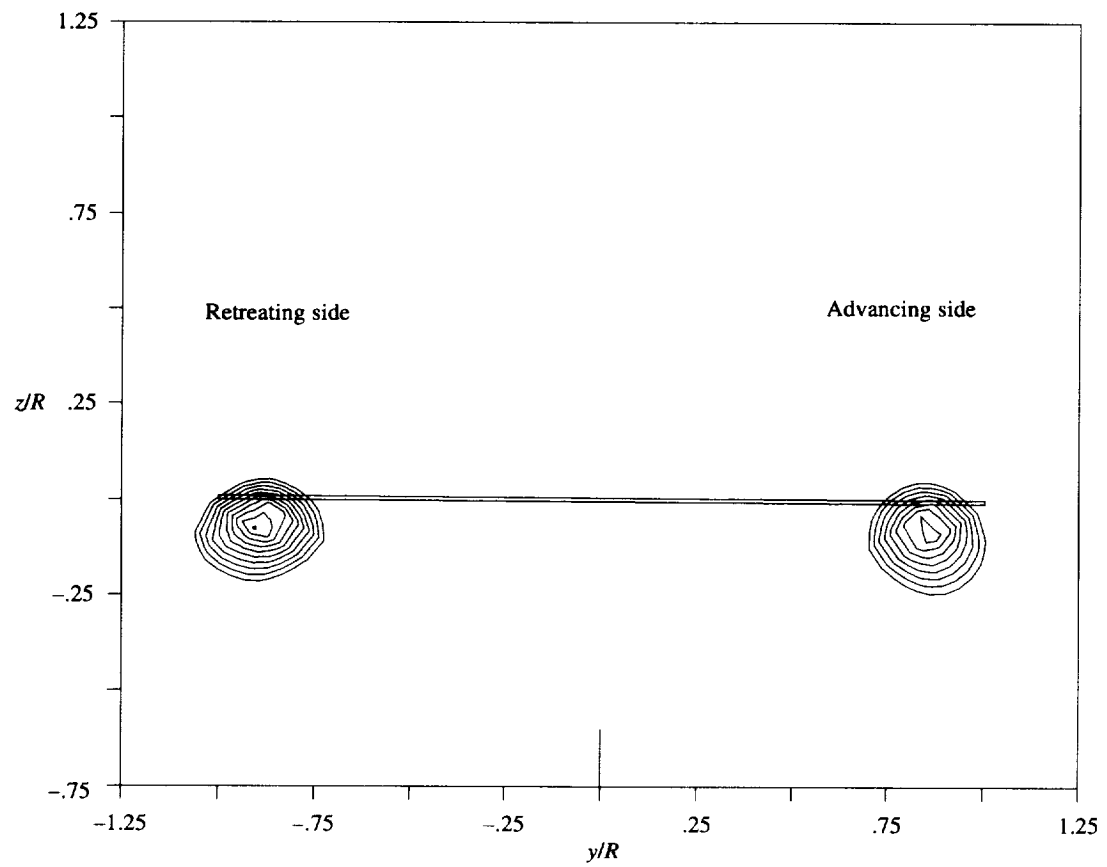
Figure 7. The 3-D Navier-Stokes vorticity contour plot at $x/R = 1.88$ and $\mu = 0.15$.
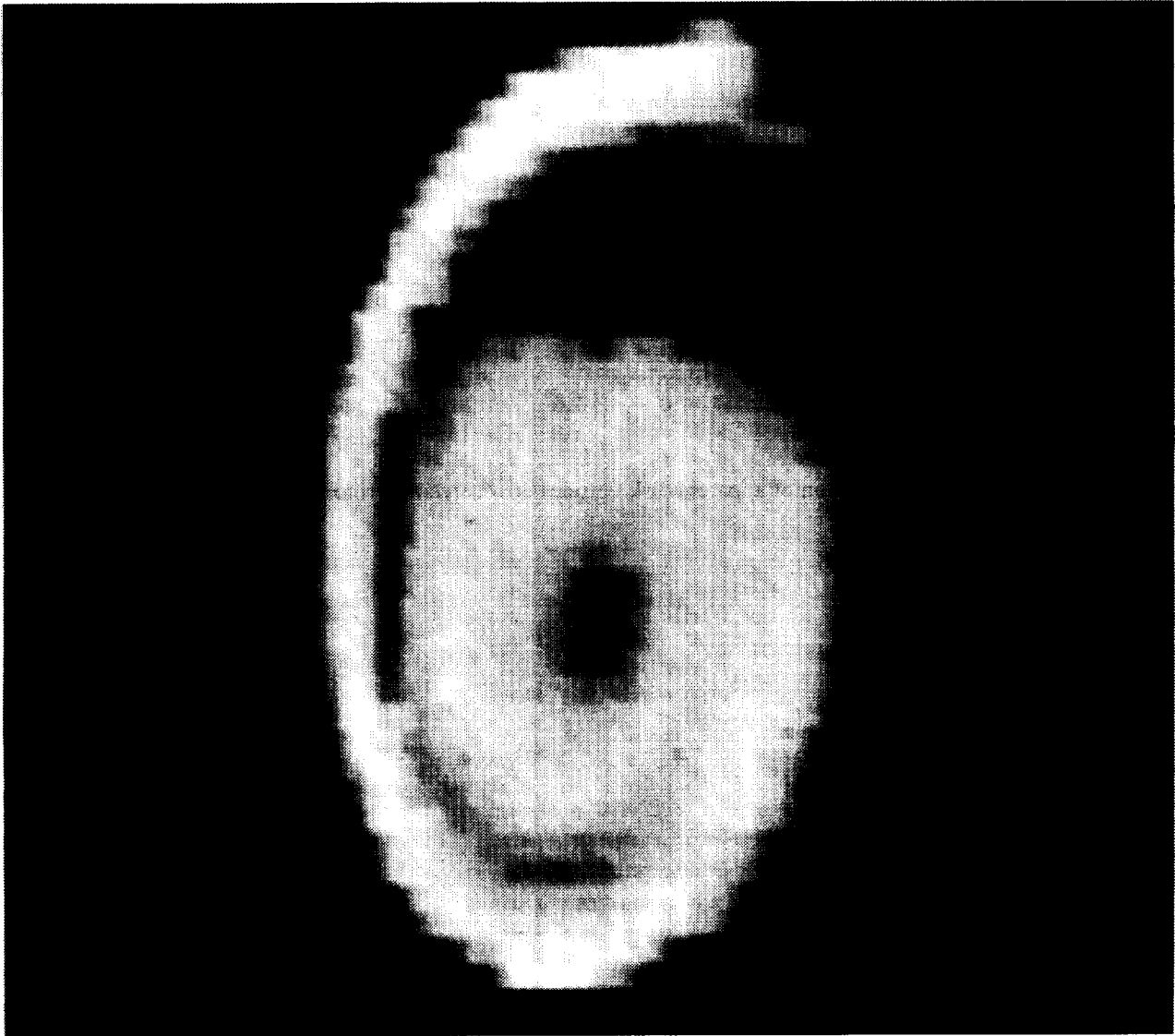
Figure 8. Typical advancing side apparent disk vortex image (viewed from downstream). Lateral laser light sheet at $x/R = 3.5$; $\mu = 0.15$.
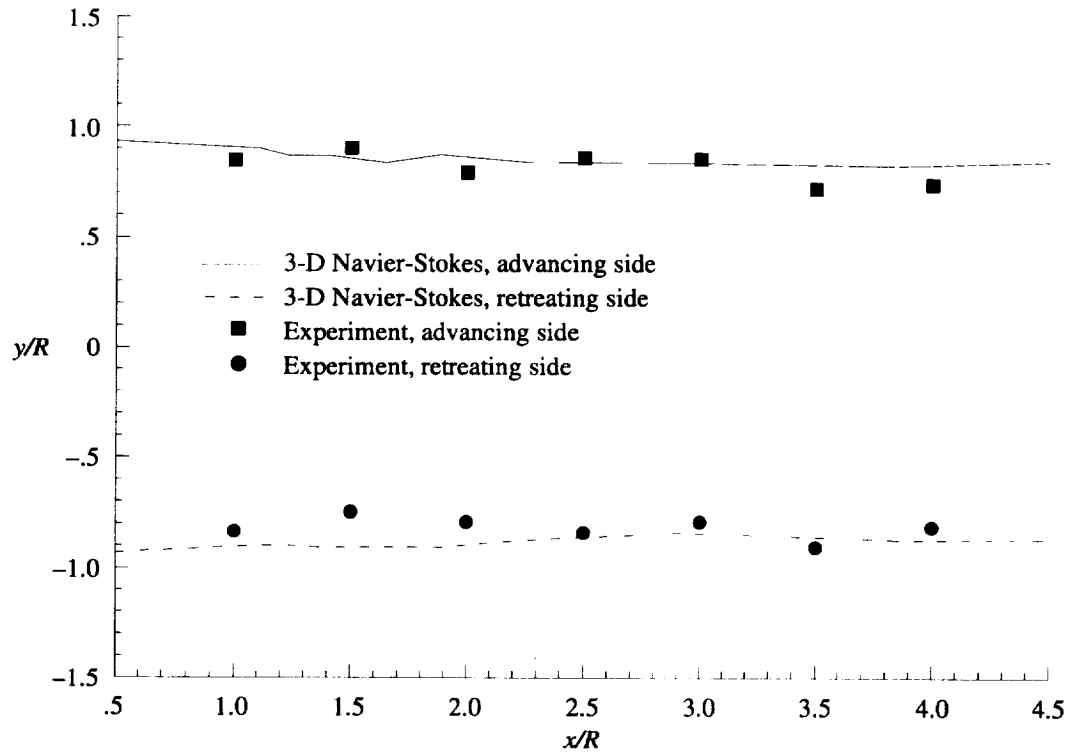
Figure 9. Lateral position of apparent disk vortices downstream of rotor hub for $\mu = 0.15$.
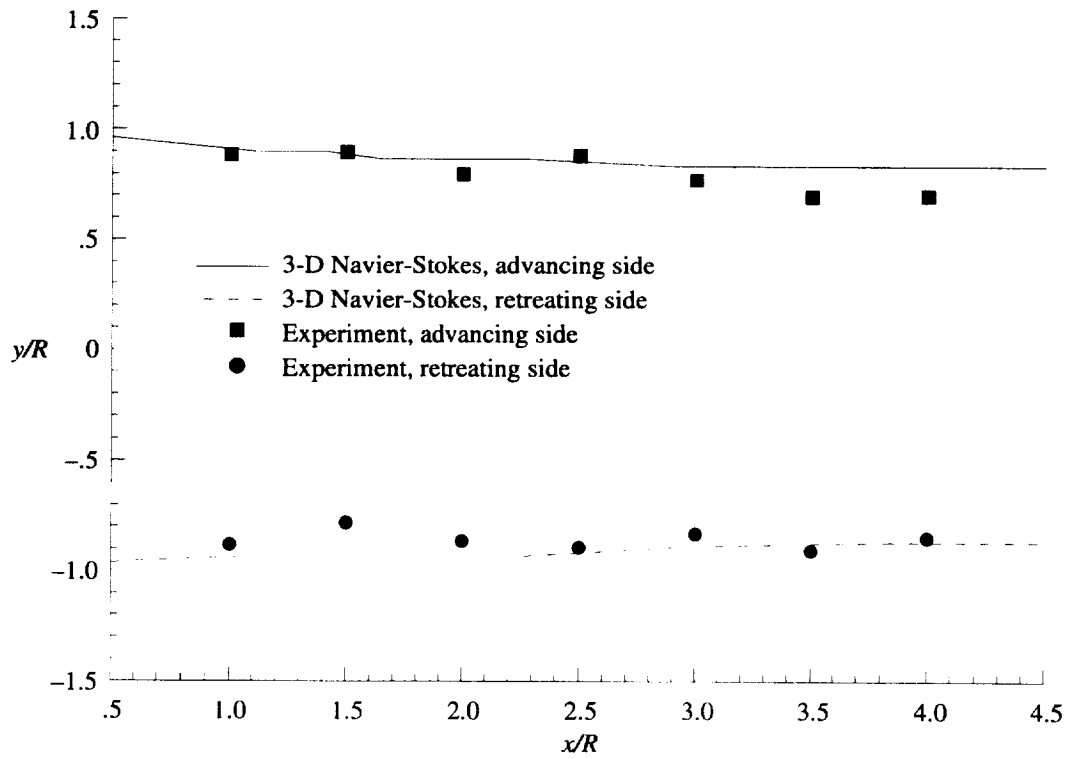


Figure 10. Lateral position of apparent disk vortices downstream of rotor hub for $\mu = 0.23$.
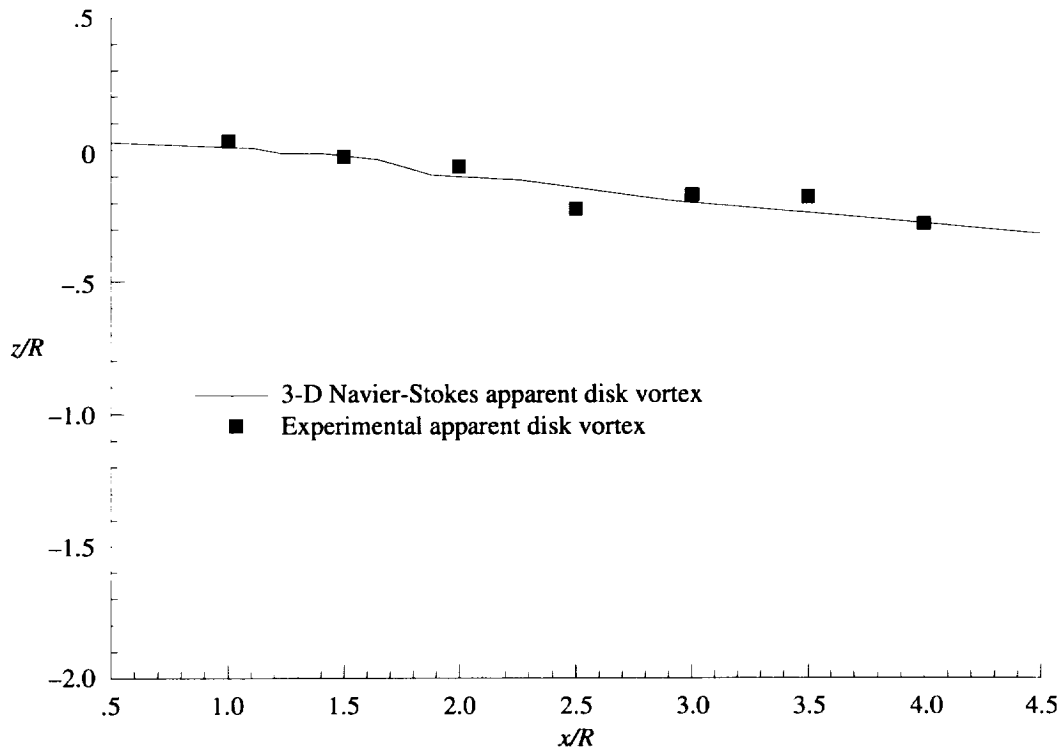
Figure 11. Vertical position of apparent disk vortices on advancing side for $\mu = 0.15$.
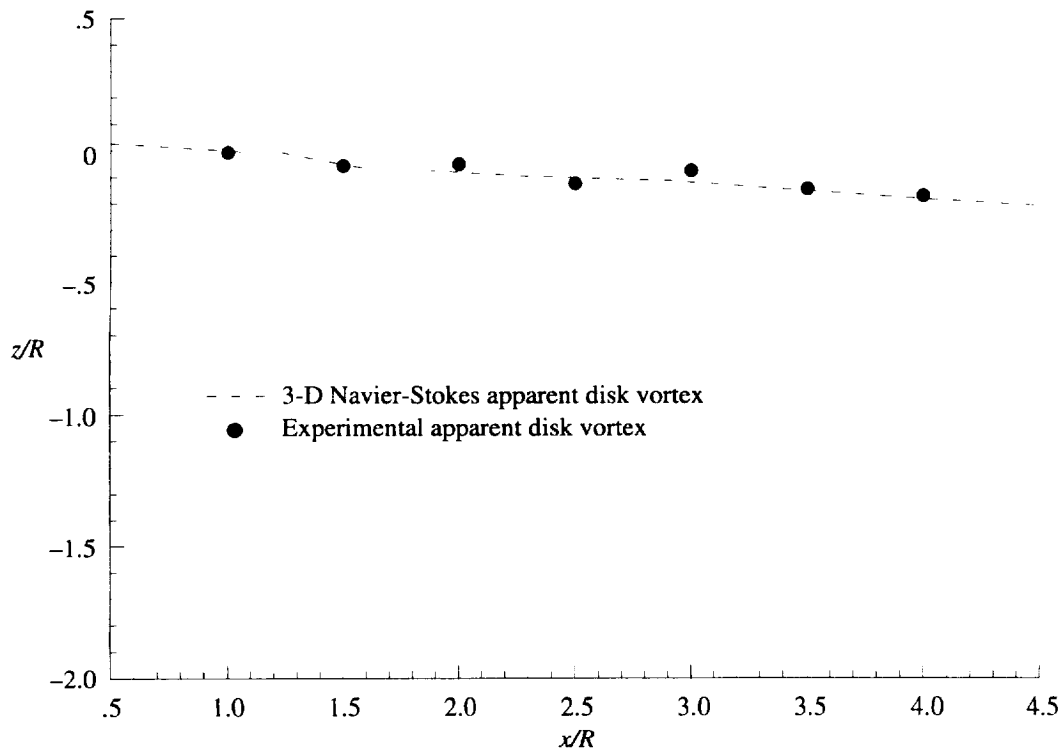


Figure 12. Vertical position of apparent disk vortices on retreating side for $\mu = 0.15$.
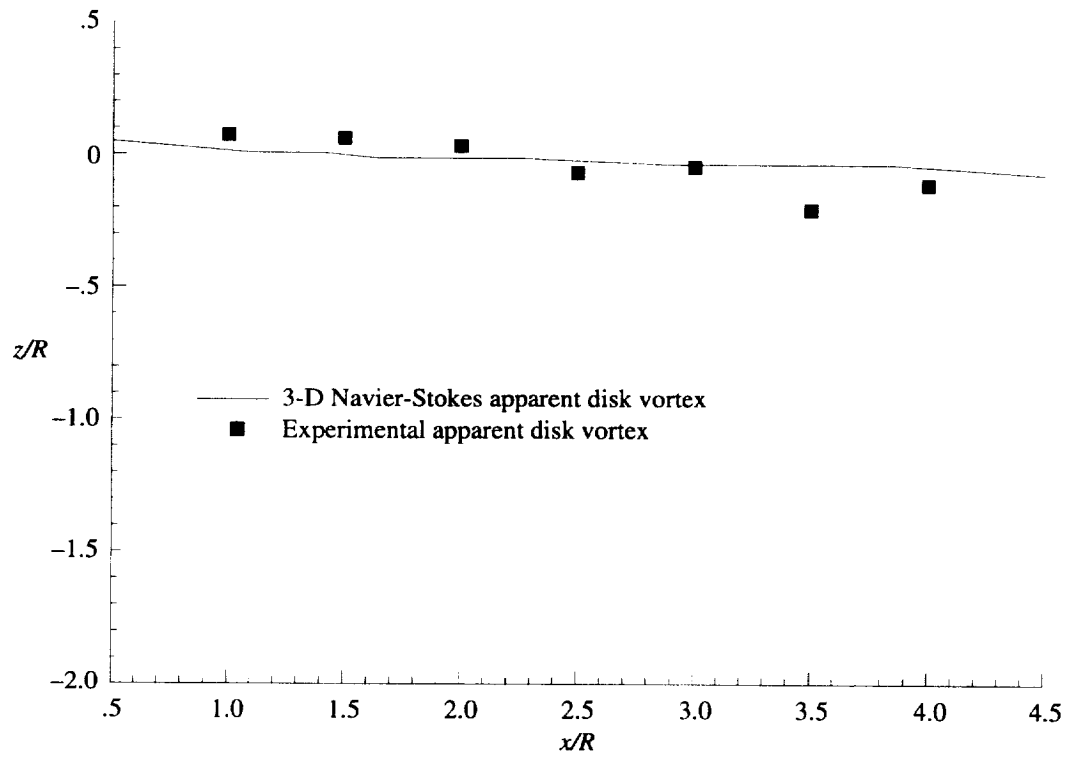
Figure 13. Vertical position of apparent disk vortices on advancing side for $\mu = 0.23$.
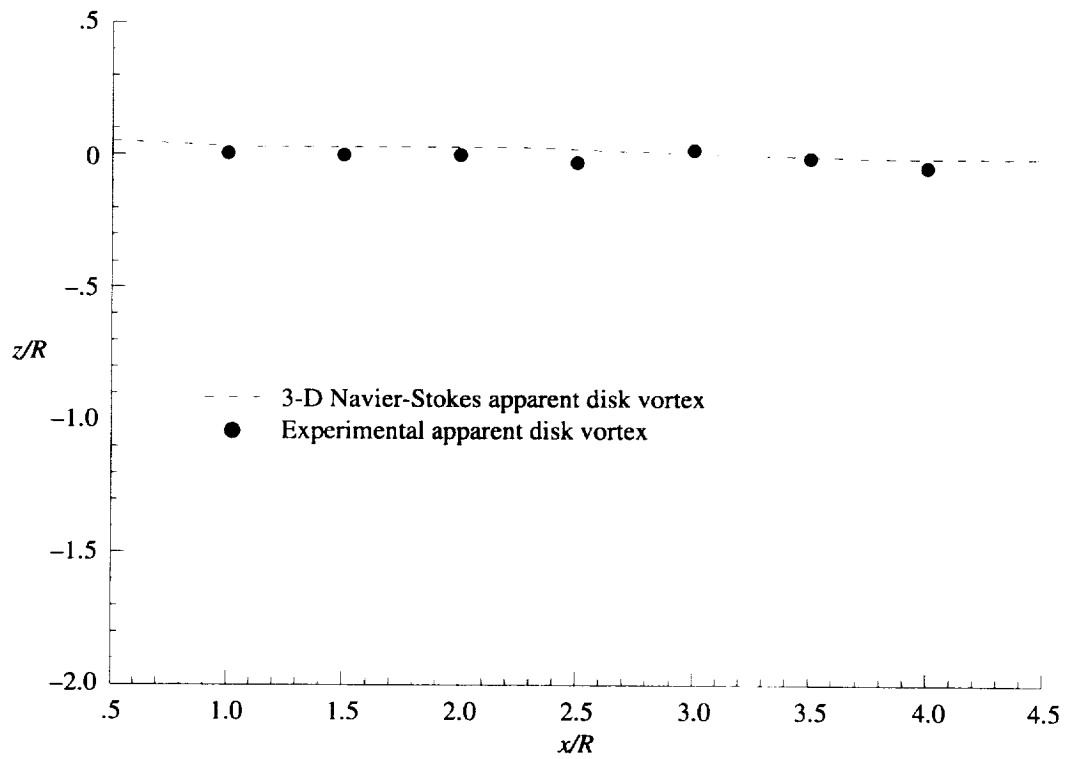


Figure 14. Vertical position of apparent disk vortices on retreating side for $\mu = 0.23$.
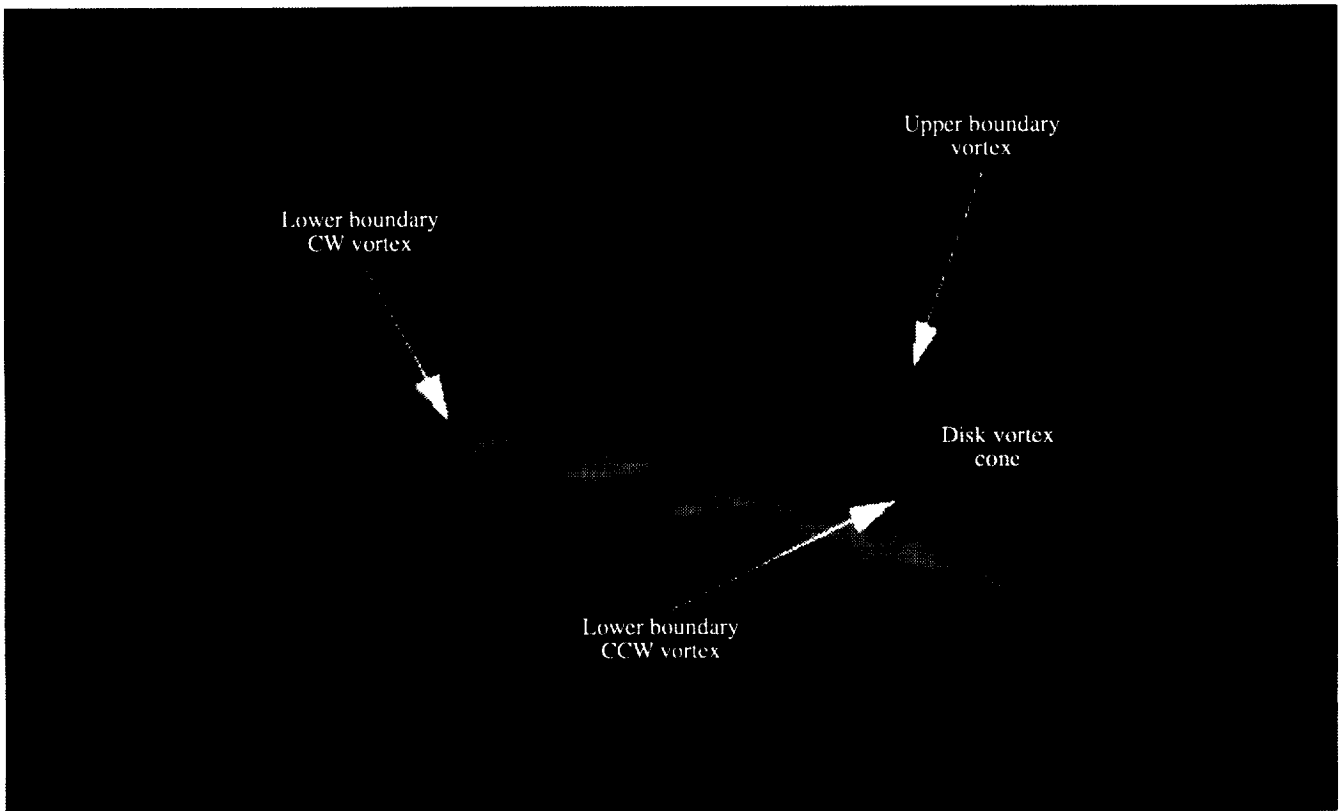
Figure 15. Typical blade tip vortices image with annotations. Longitudinal laser light sheet at $y/R = -0.8$; $\mu = 0.15$.
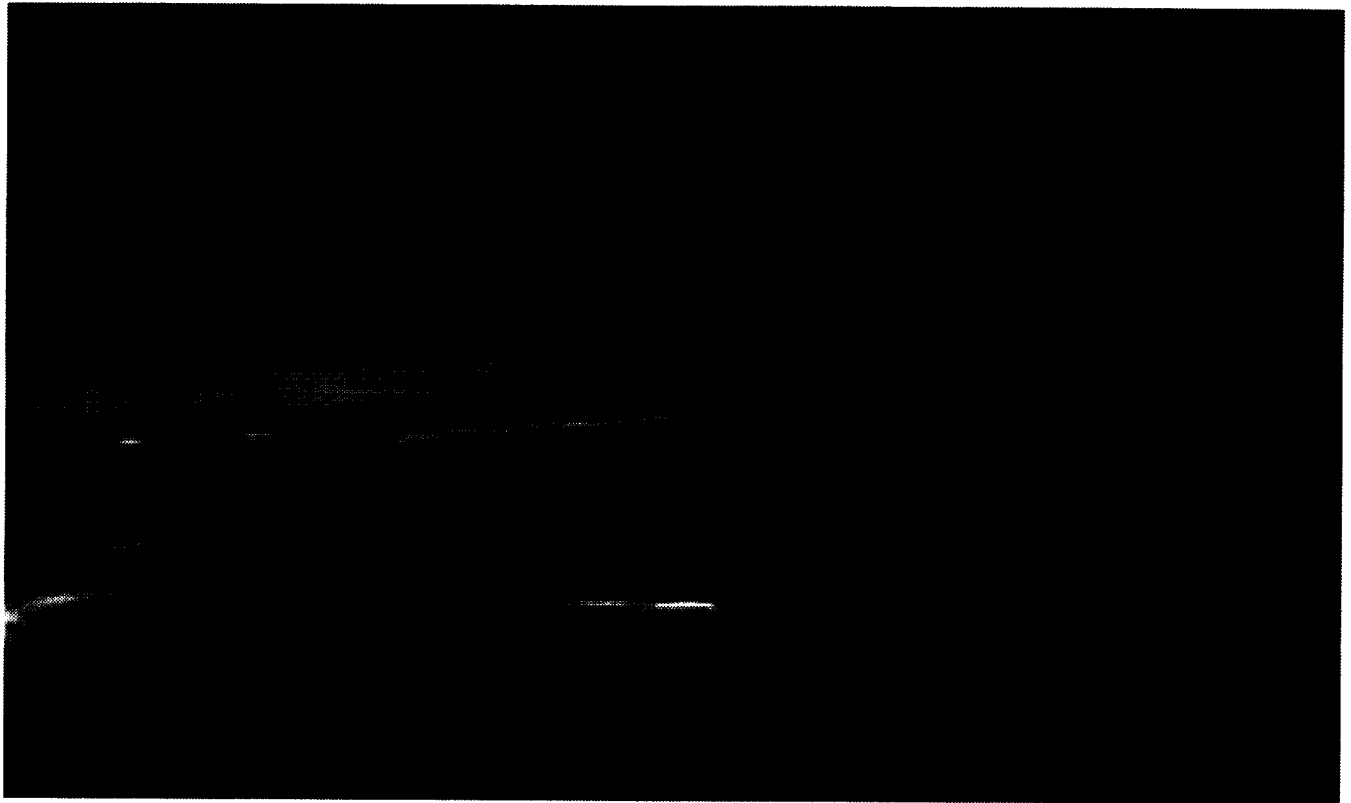
Figure 16. The 2MRTS in wind tunnel with lights on. Longitudinal laser light sheet at $y/R = -0.8$; $\mu = 0.15$.
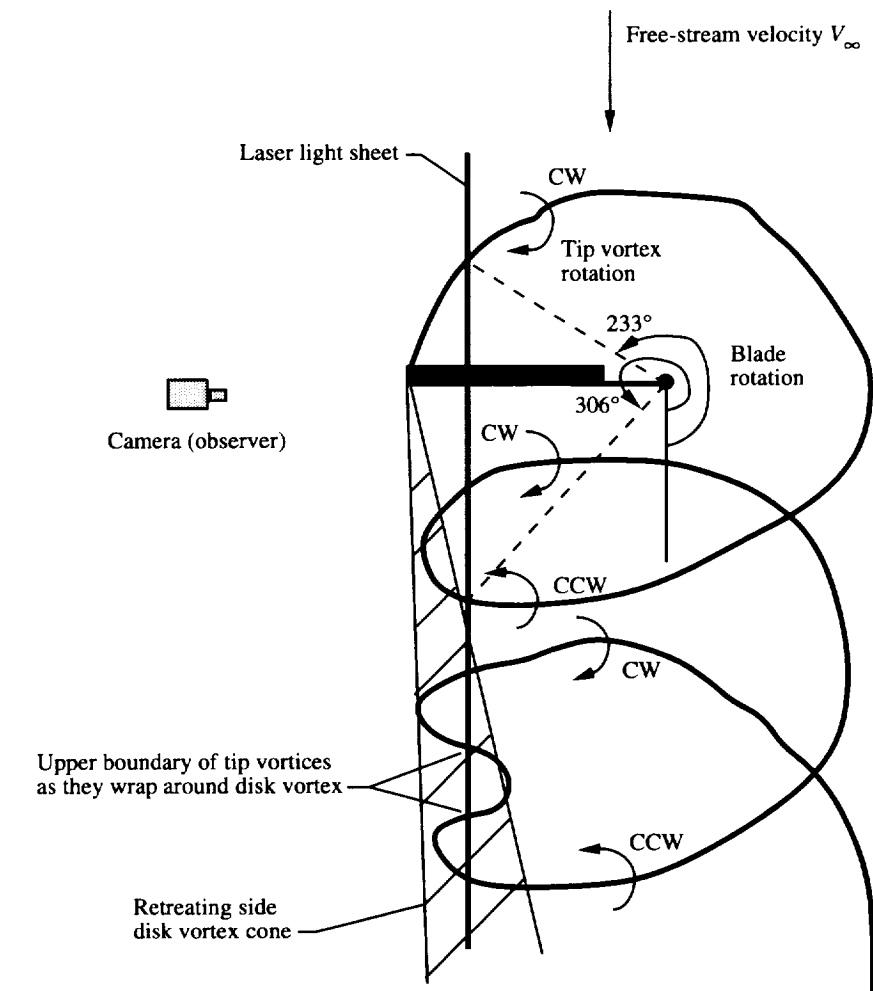
Figure 17. Top view of blade tip vortices cutting through laser light sheet plane.
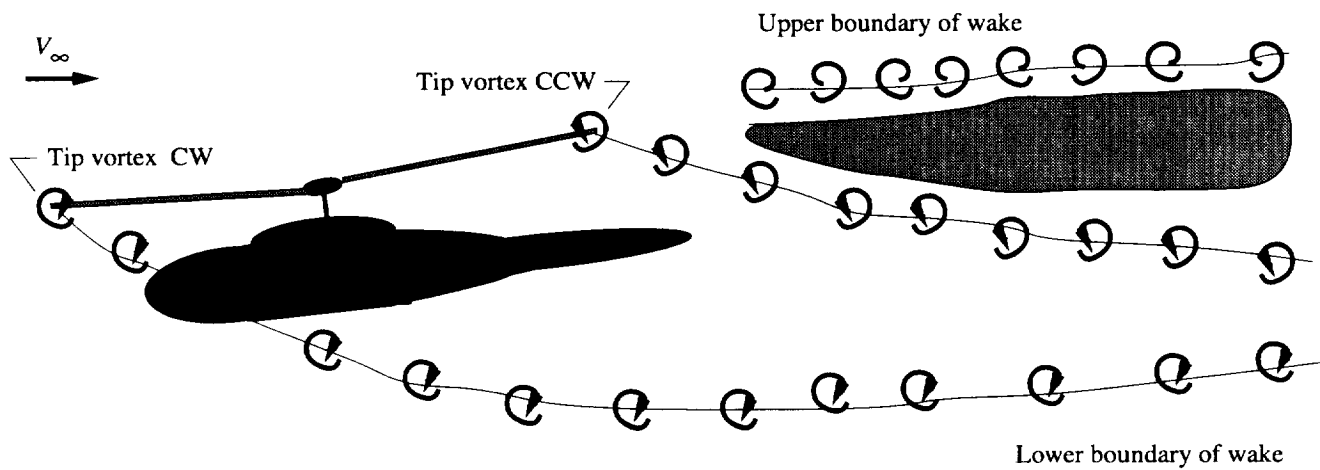


Figure 18. Side view of blade tip vortices cutting through laser light sheet plane.
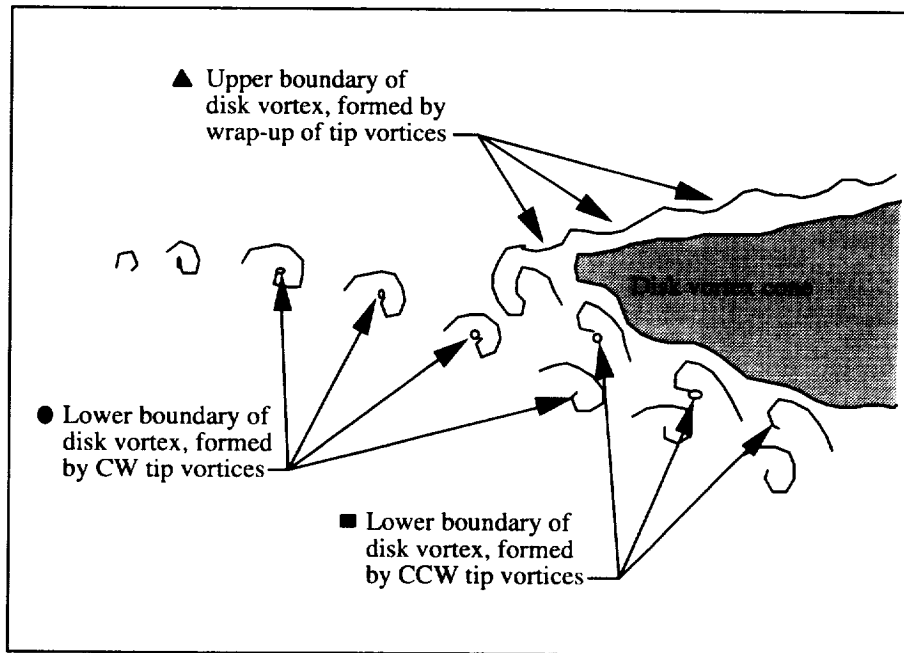
(a) Video image.
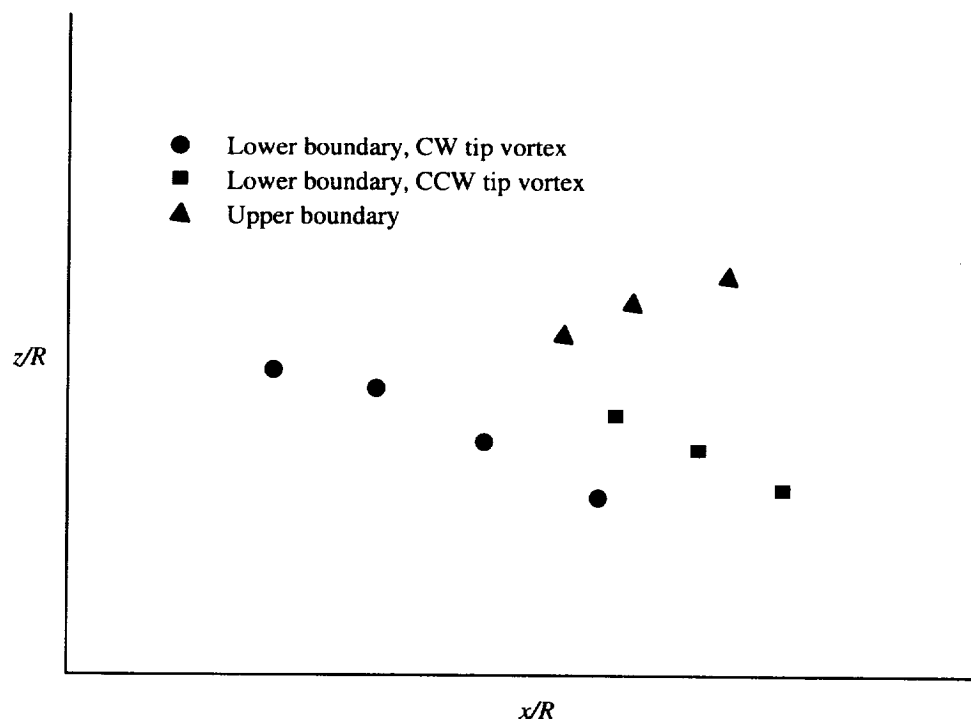


(b) Subsequent plotted data.

Figure 19. Location of tip vortices. (See fig. 15.)
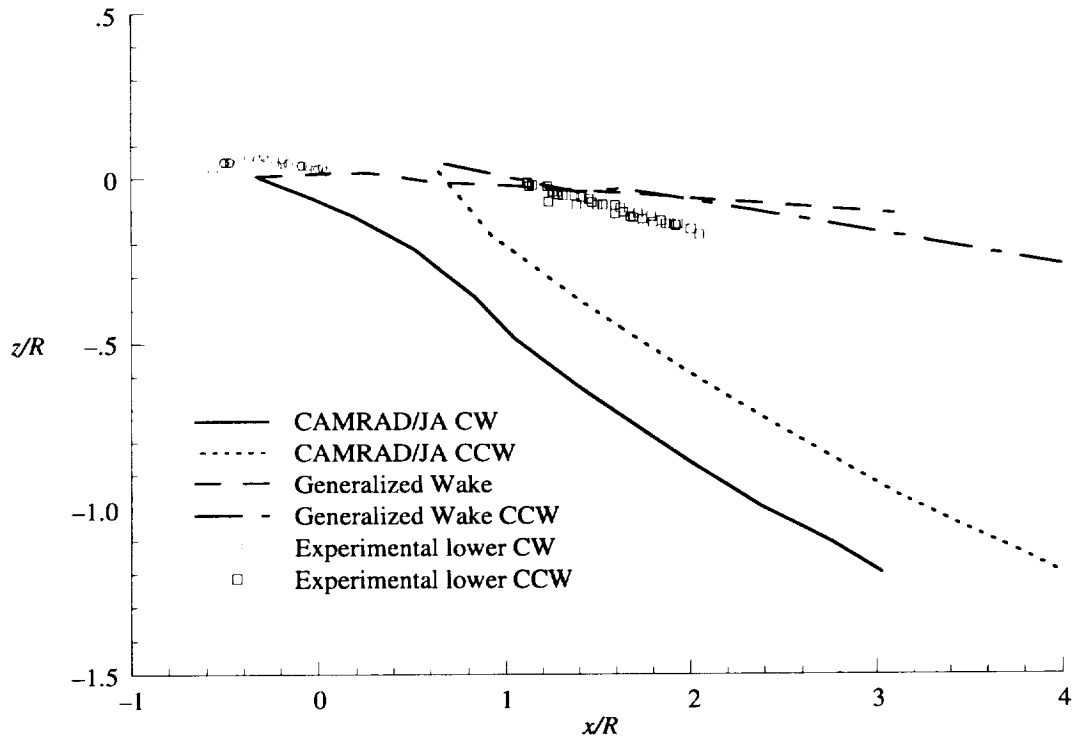
(a) $\mu = 0.15$.
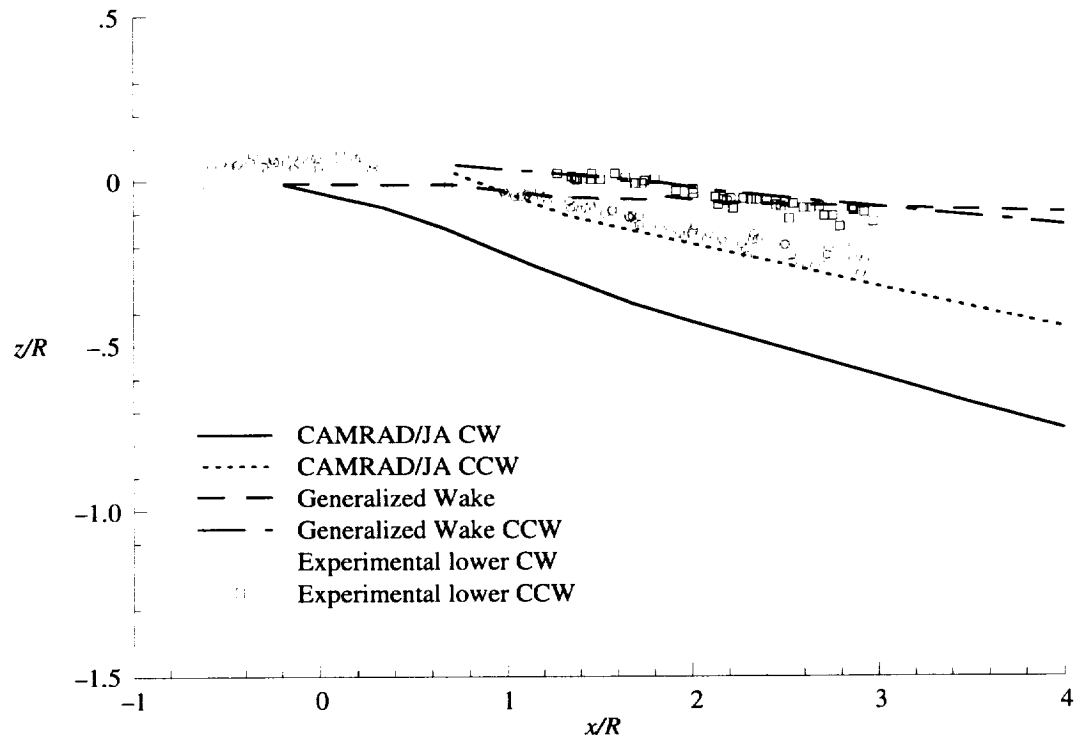


(b) $\mu = 0.23$.

Figure 20. Tip vortex core locations at $y/R = 0.8$ plotted with CAMRAD/JA and Generalized Wake data.

.5

0

z/R   −.5

RWF CW; fuselage
RWF CCW; fuselage
RWF CW; no fuselage
RWF CCW; no fuselage
Experimental lower CW
Experimental lower CCW

−1.0

−1.5

−1        0        1        2        3        4

x/R

(a) μ = 0.15.

.5

0

z/R   −.5

RWF CW; fuselage
RWF CCW; fuselage
RWF CW; no fuselage
RWF CCW; no fuselage
Experimental lower CW
Experimental lower CCW

−1.0

−1.5

−1        0        1        2        3        4

x/R
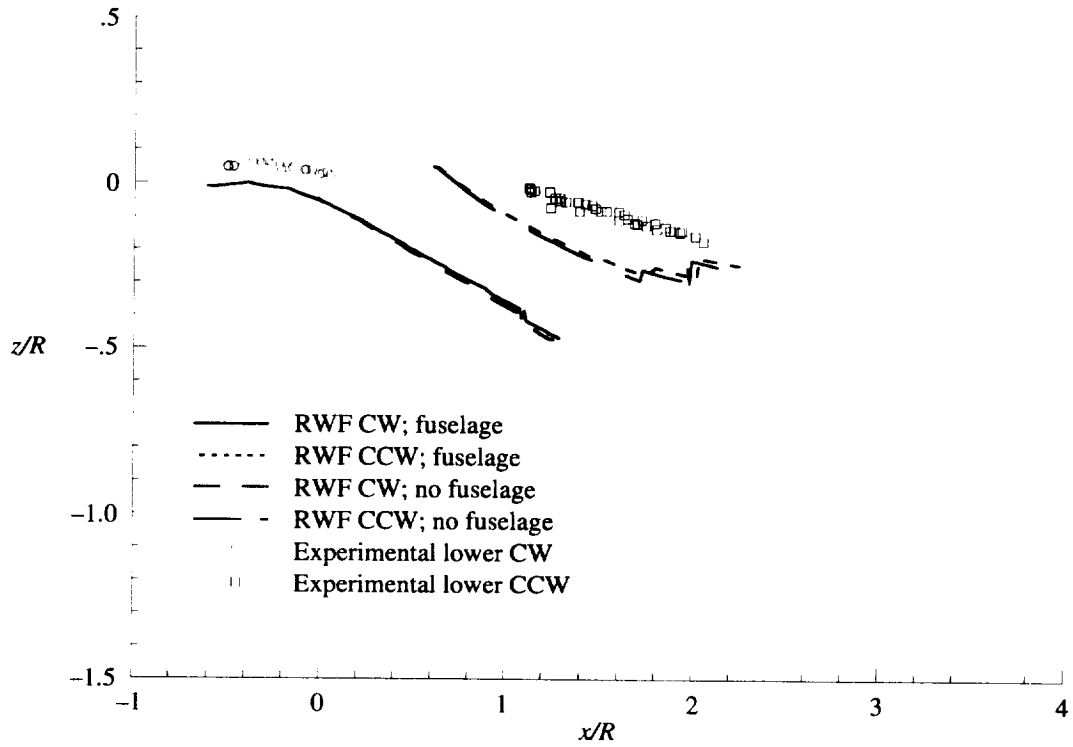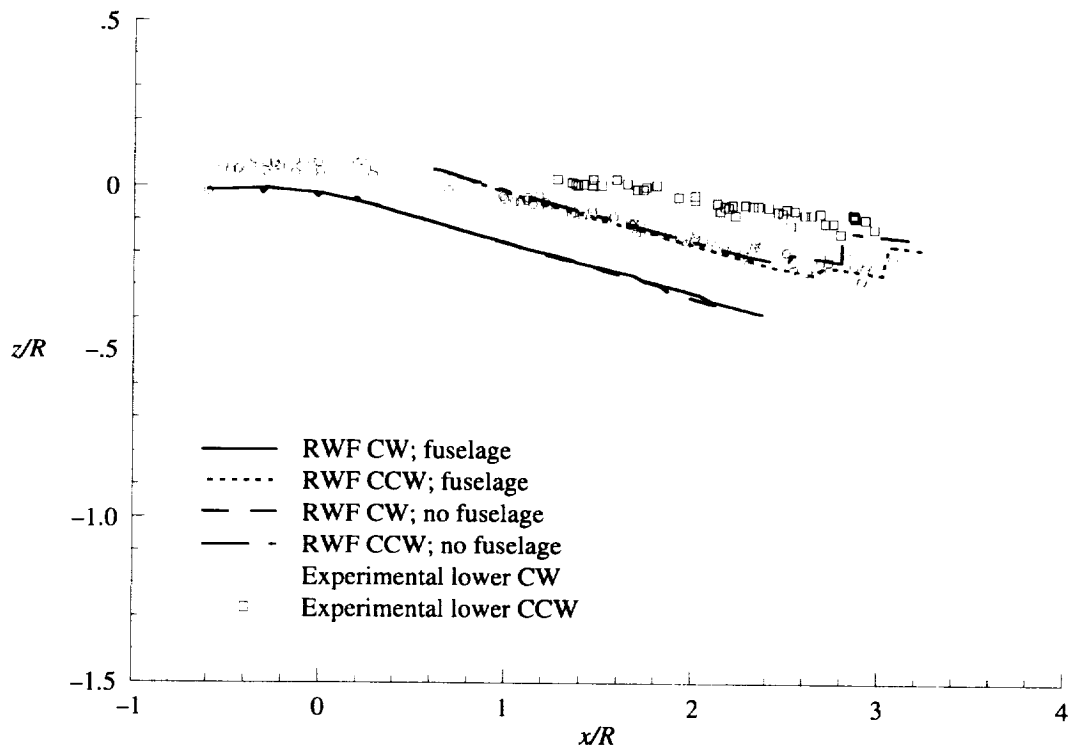
(b) μ = 0.23.

Figure 21. Tip vortex core locations at $y/R$ = 0.8 plotted with RWF data with and without fuselage.

(a) μ = 0.15.
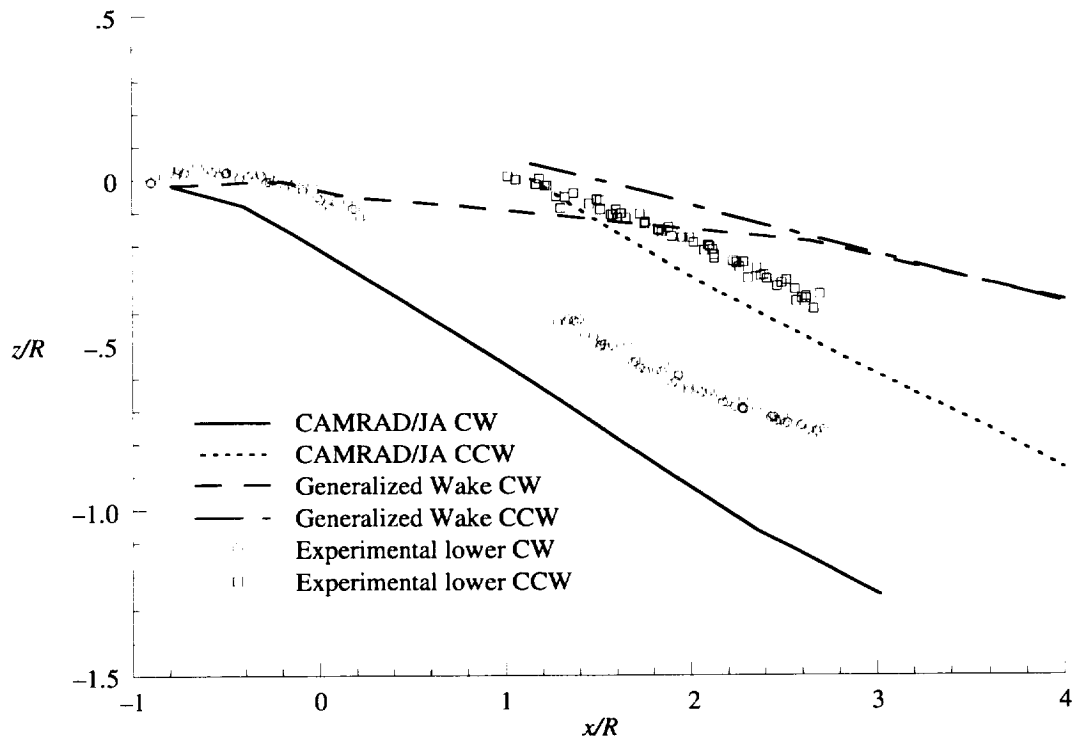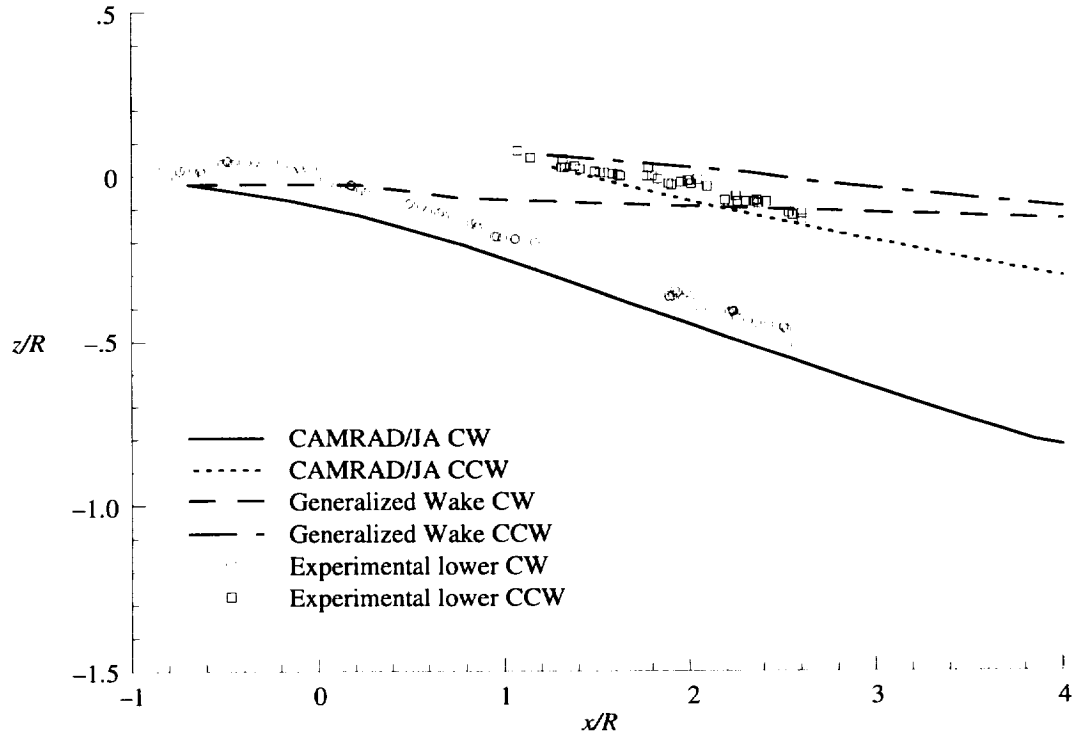


(b) μ = 0.23.

Figure 22. Tip vortex core locations at y/R = 0.3 plotted with CAMRAD/JA and Generalized Wake data.
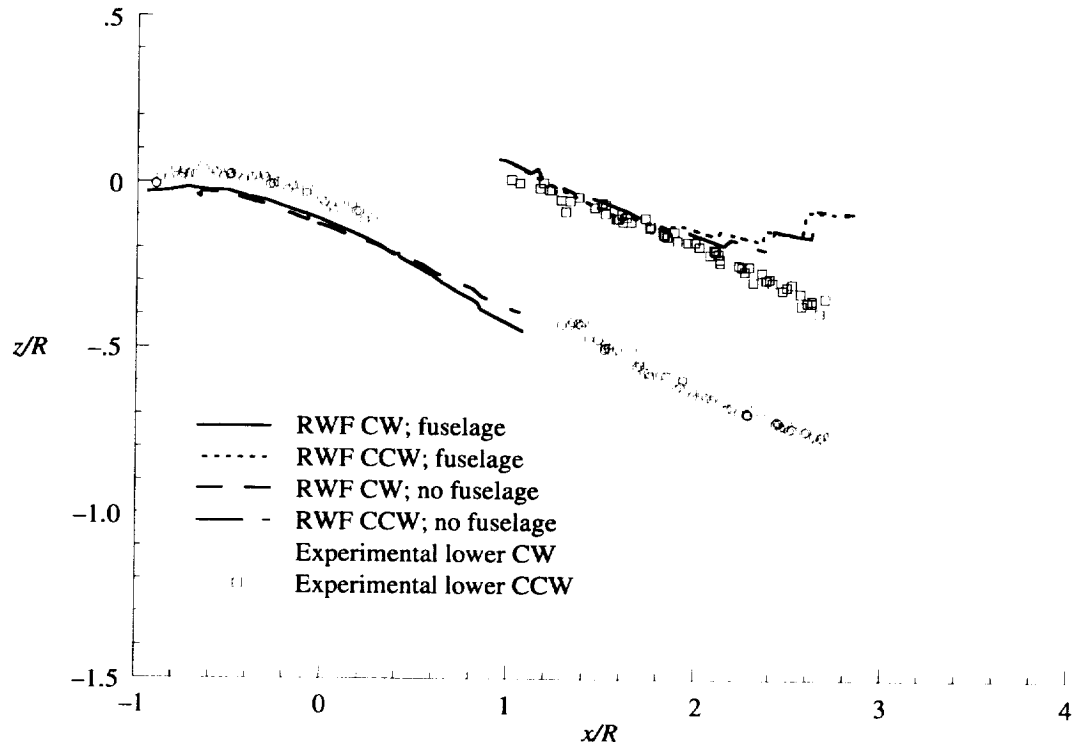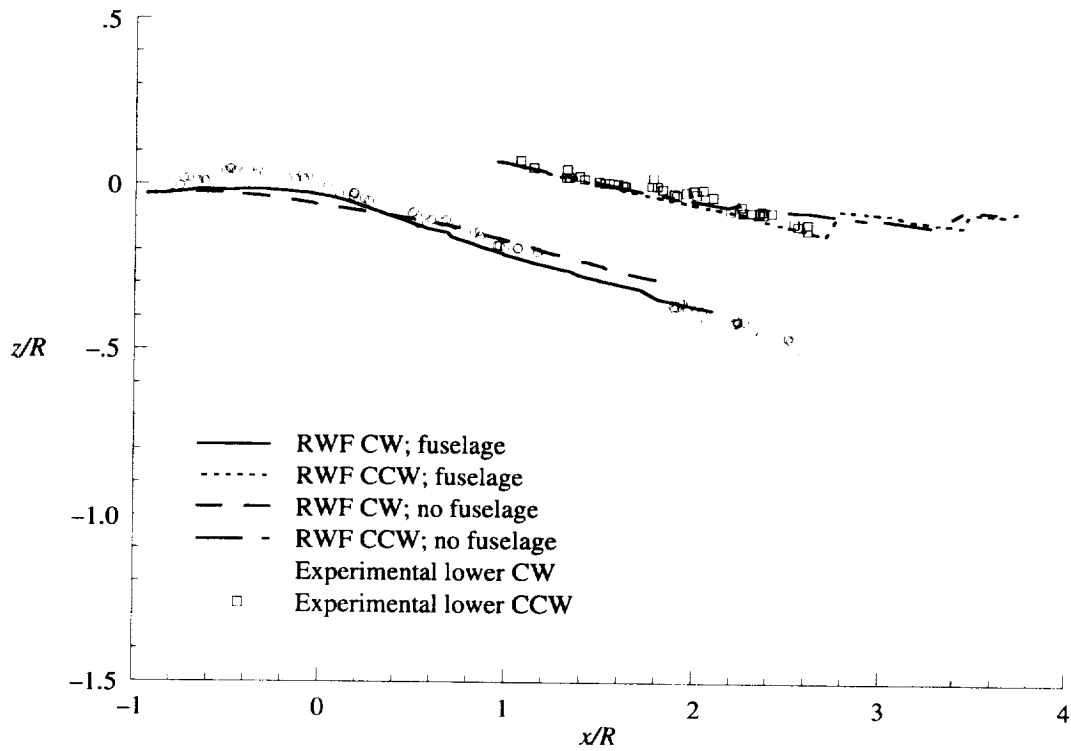
(a) $\mu = 0.15$.



(b) $\mu = 0.23$.

Figure 23. Tip vortex core locations at $y/R = 0.3$ plotted with RWF data with and without fuselage.
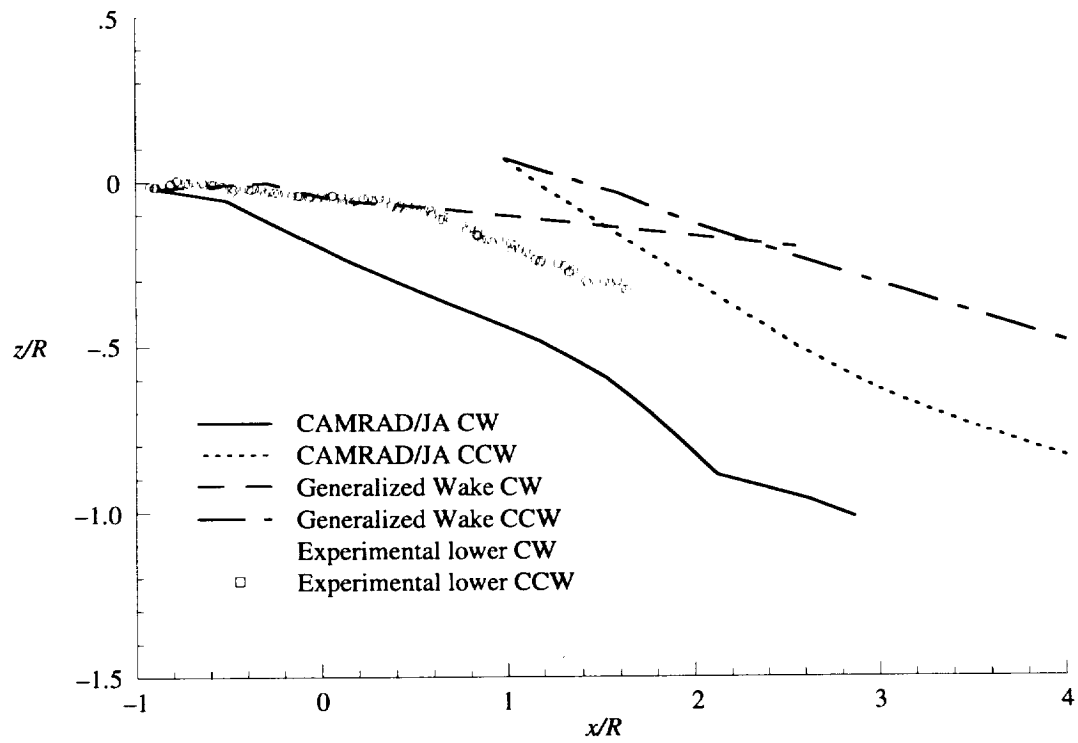
(a) $\mu = 0.15$.
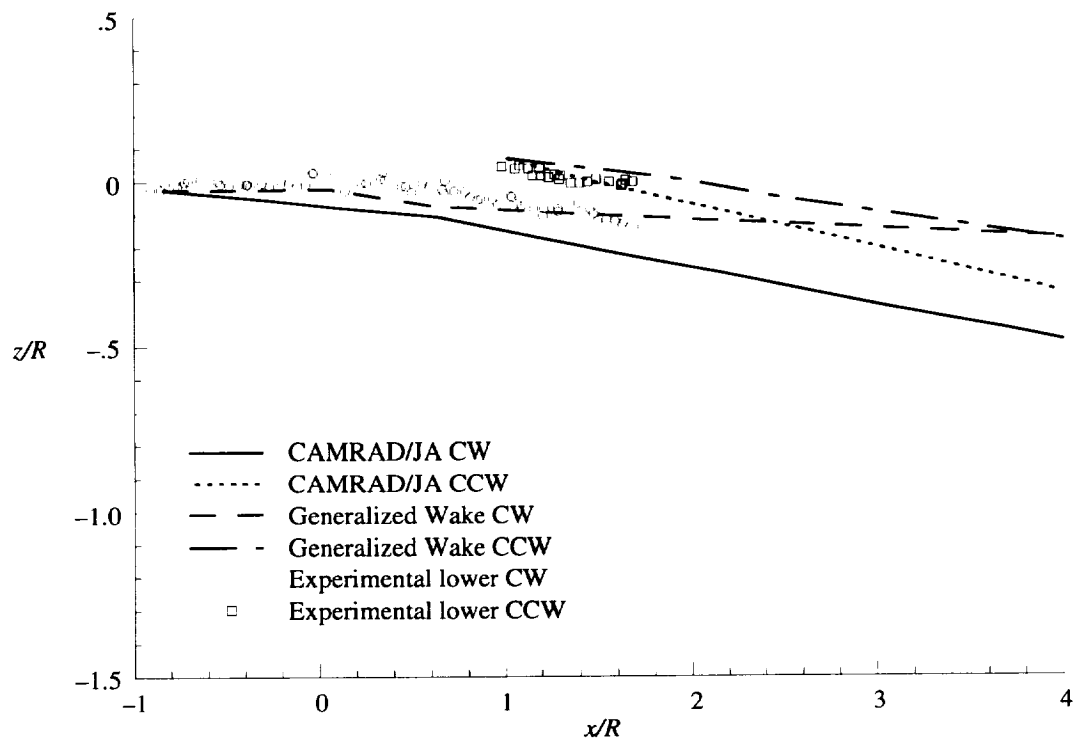


(b) $\mu = 0.23$.

Figure 24. Tip vortex core locations at $y/R = -0.3$ plotted with CAMRAD/JA and Generalized Wake data.
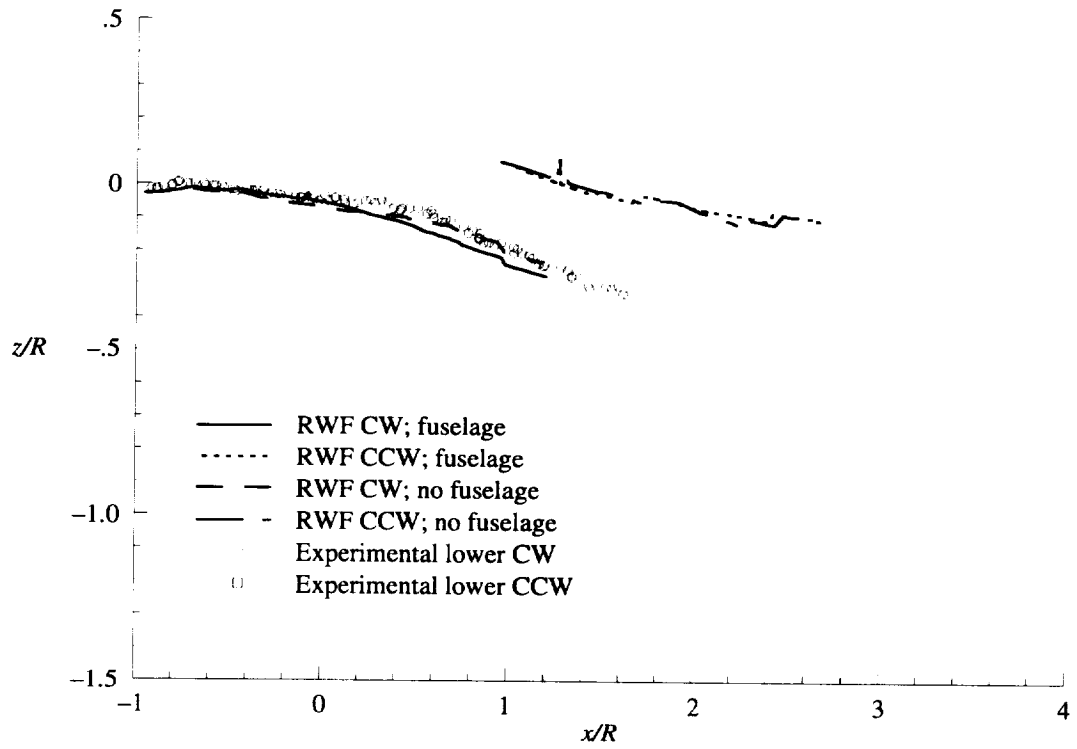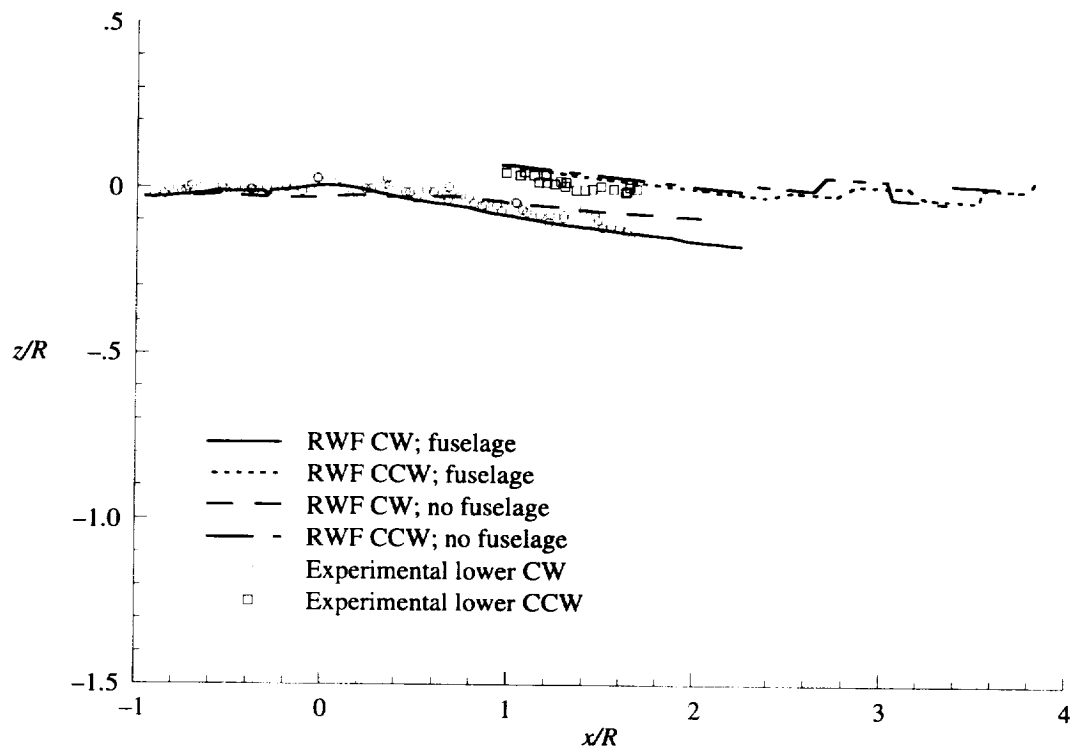
(a) $\mu = 0.15$.



(b) $\mu = 0.23$.

Figure 25. Tip vortex core locations at $y/R = -0.3$ plotted with RWF data with and without fuselage.

(a) μ = 0.15.
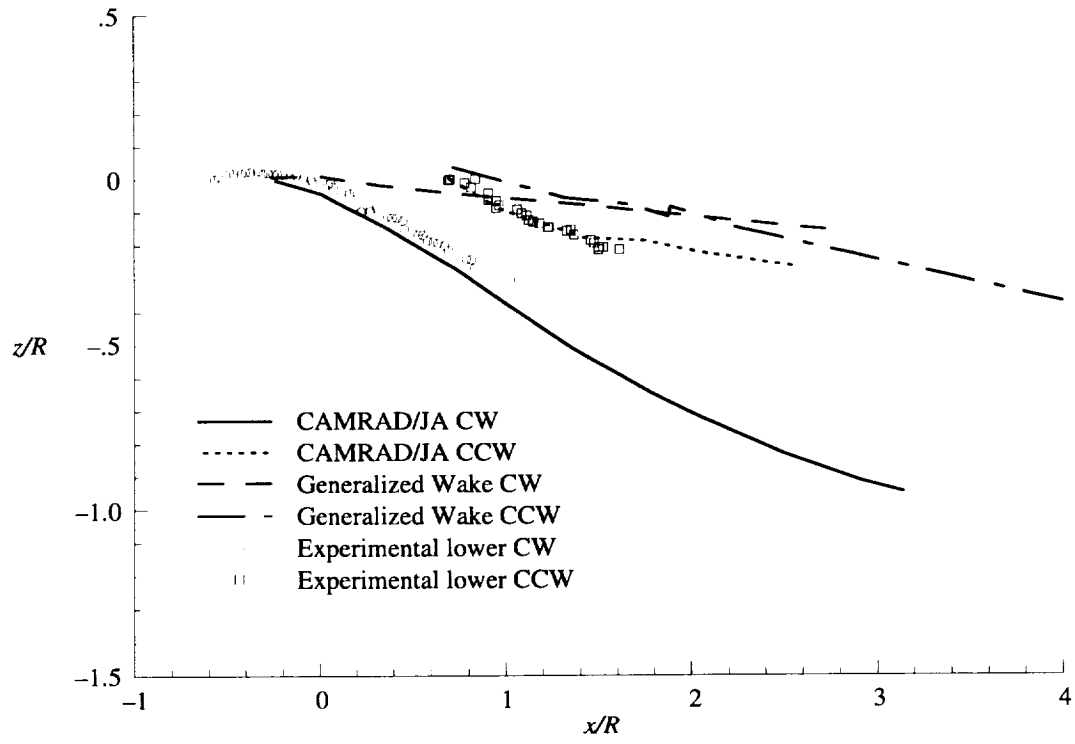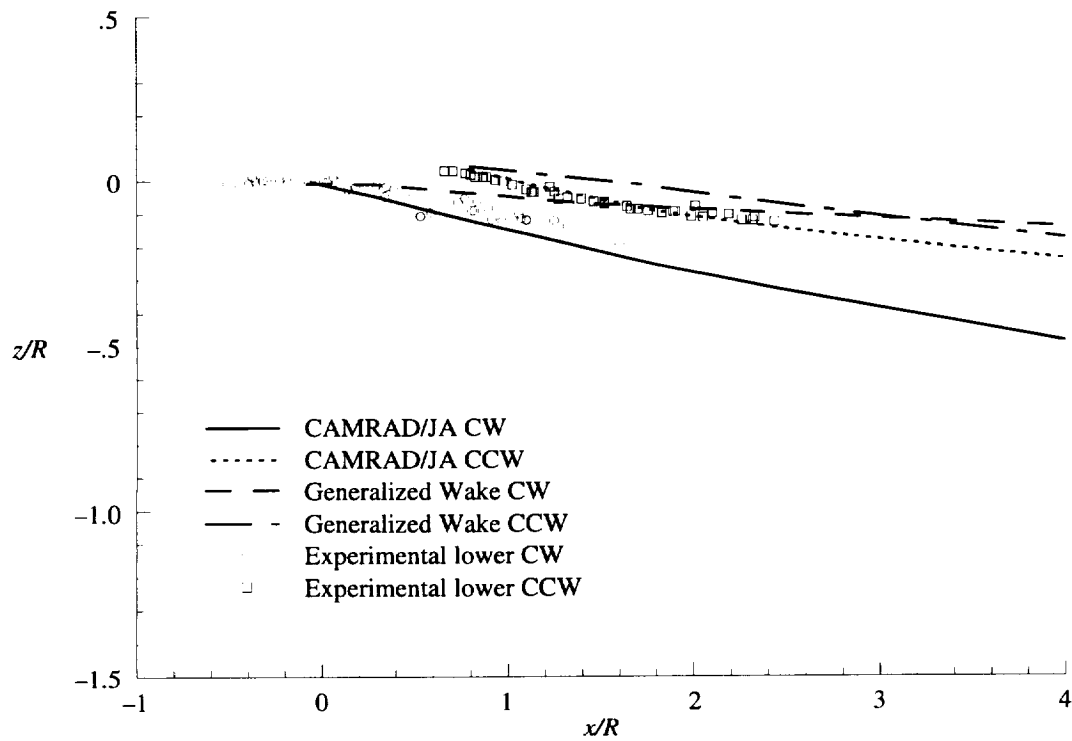


(b) μ = 0.23.

Figure 26. Tip vortex core locations at $y/R = -0.8$ plotted with CAMRAD/JA and Generalized Wake data.
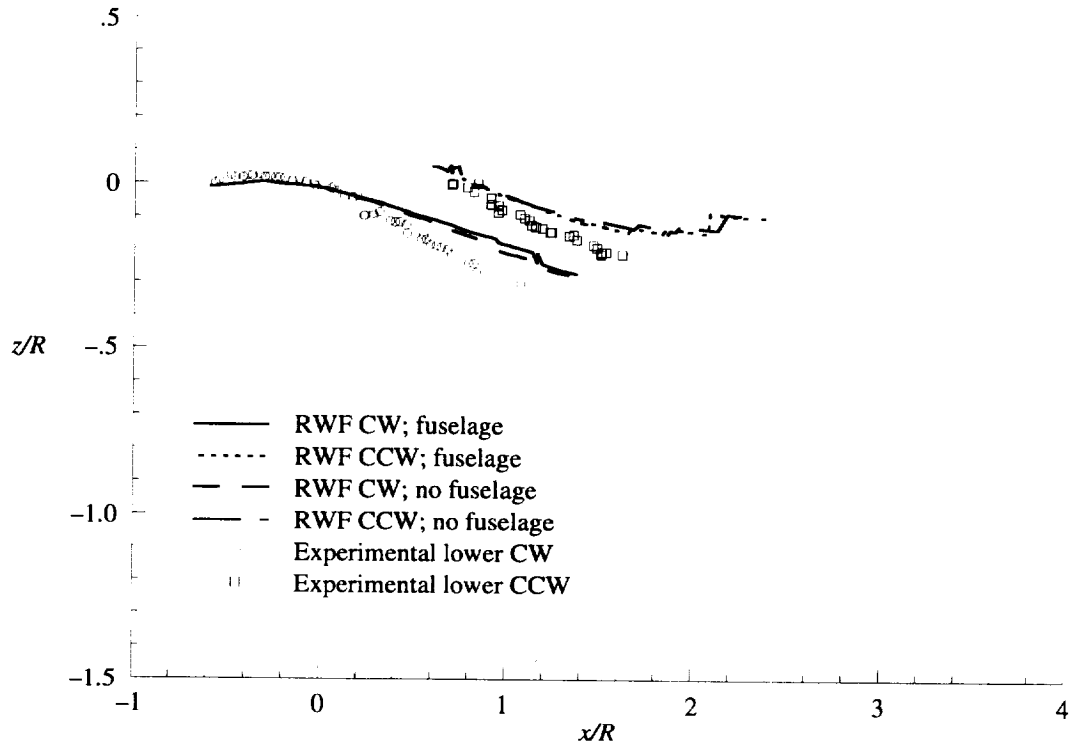
(a) $\mu = 0.15$.
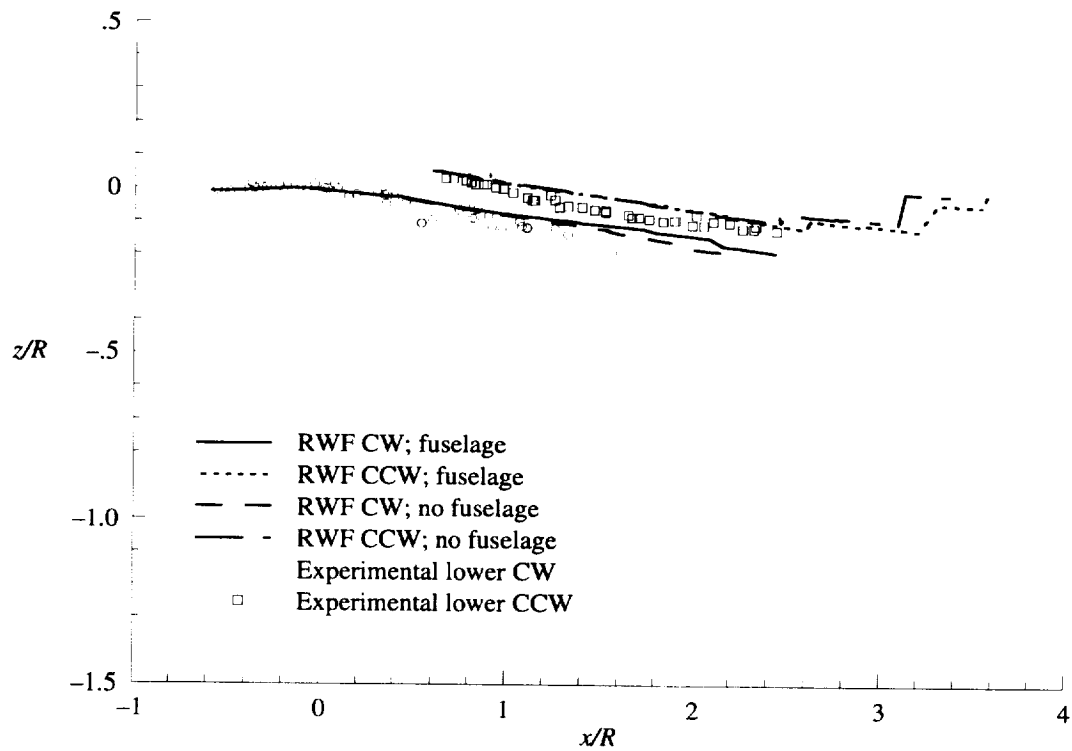


(b) $\mu = 0.23$.

Figure 27. Tip vortex core locations at $y/R = -0.8$ plotted with RWF data with and without fuselage.
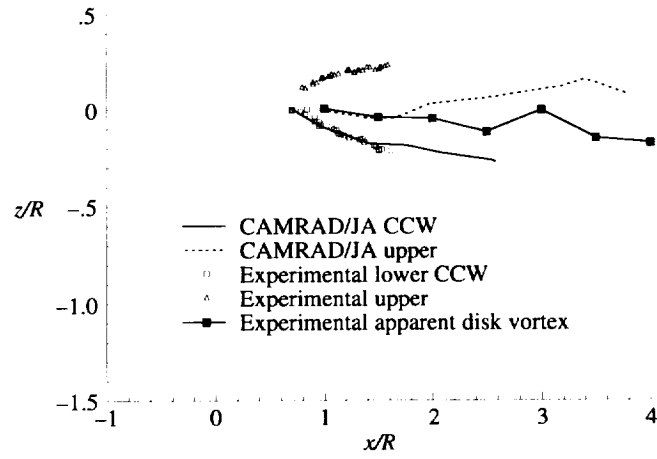
(a) $y/R = -0.8$; $\mu = 0.15$.
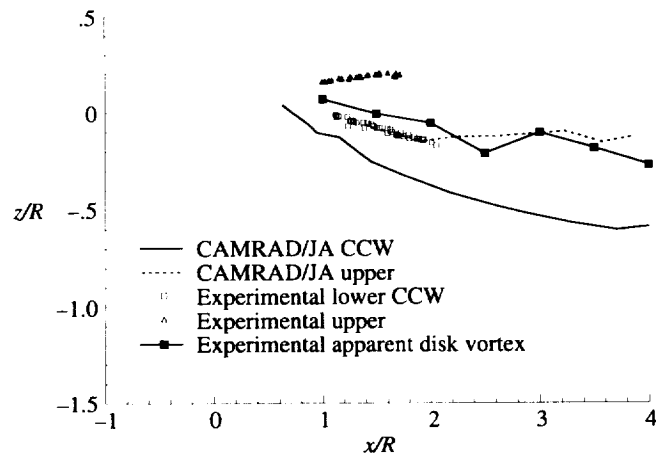


(b) $y/R = 0.8$; $\mu = 0.15$.
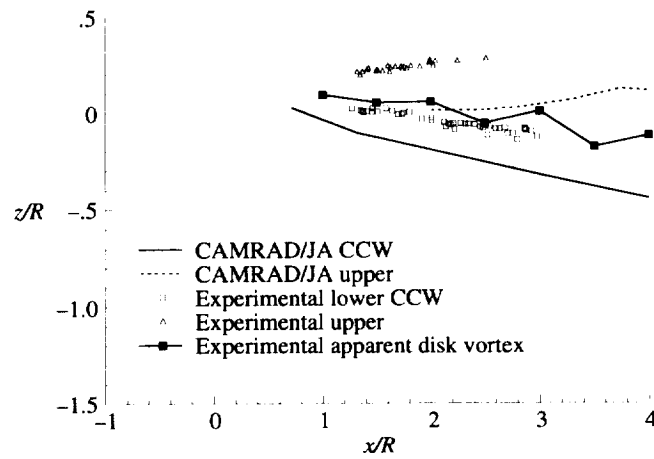


(c) $y/R = 0.8$; $\mu = 0.23$.

Figure 28. Vortex wrap-up.
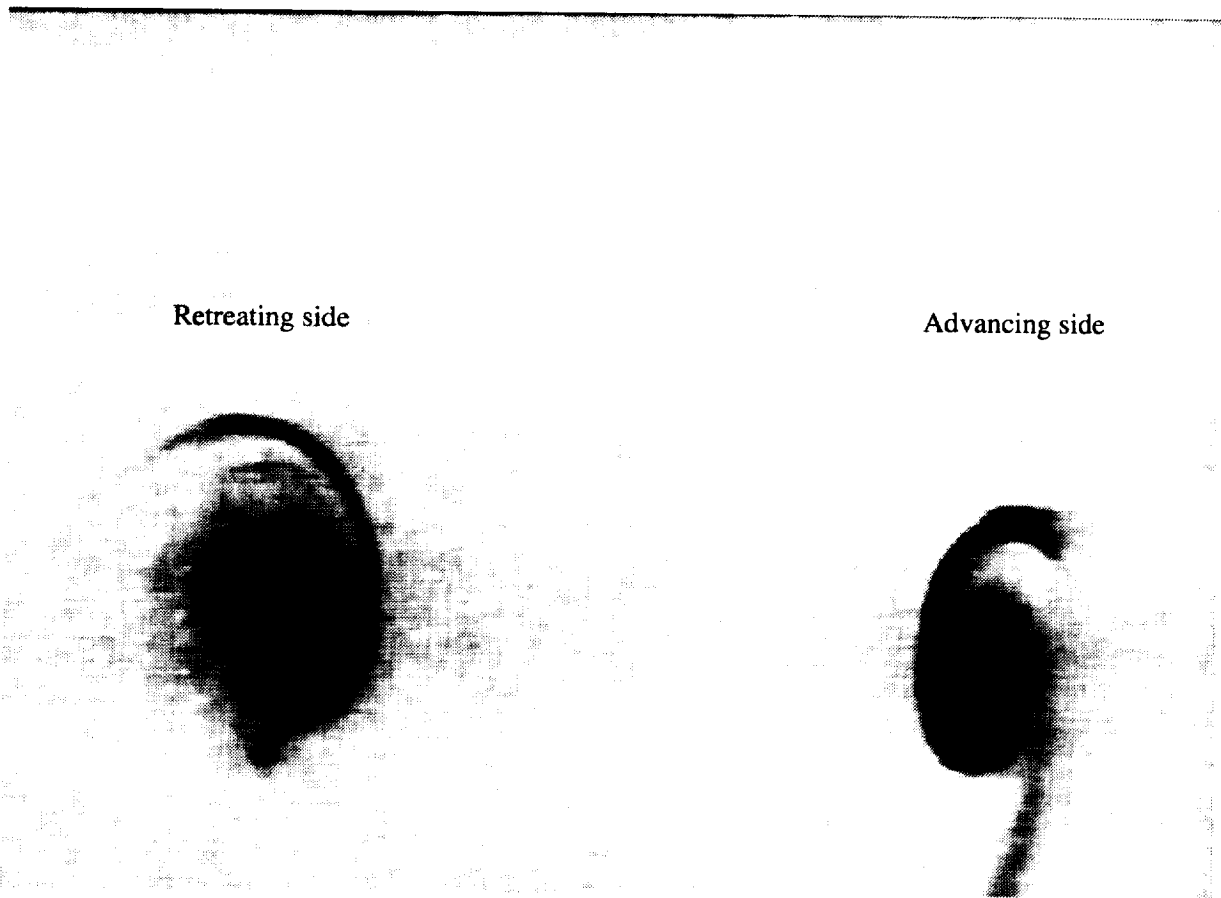
Figure 29. Enhanced image of disk vortices depicting tighter roll-up on advancing side of disk. $x/R = 2.0$; $\mu = 0.15$.
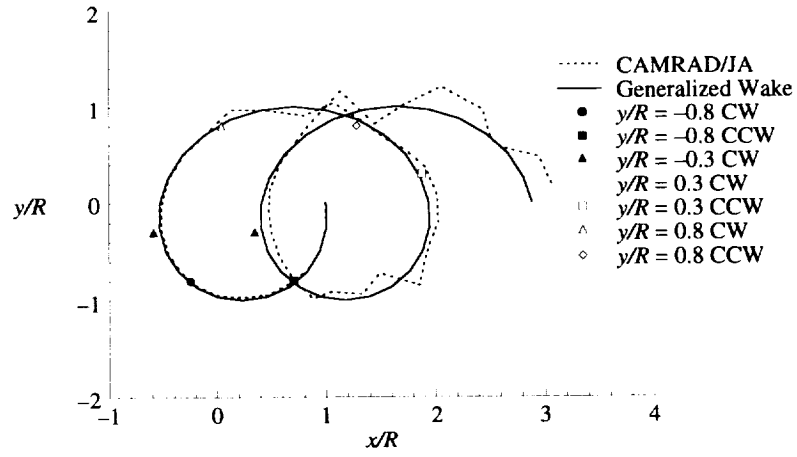
(a) From above.
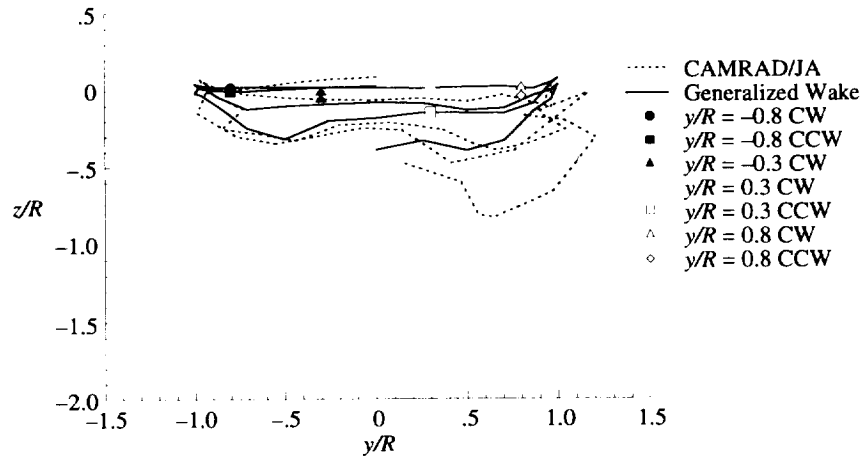


(b) From behind.
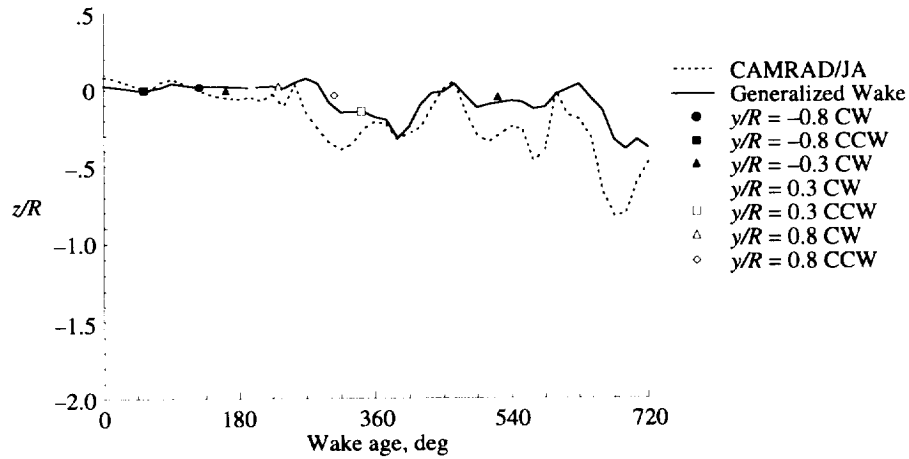


(c) Height of single vortex filament versus wake age.

Figure 30. Tip vortex location versus CAMRAD/JA and Generalized Wake predictions for $\mu = 0.15$ and $\psi_b = 0°$.

51
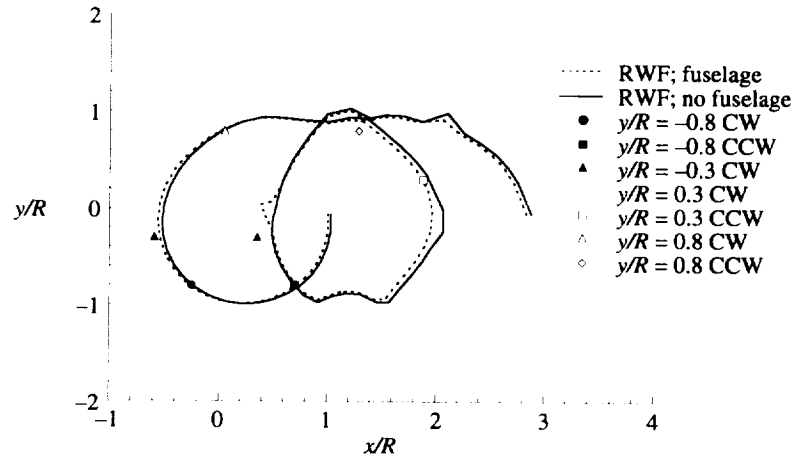
(a) From above.



(b) From behind.



(c) Height of single vortex filament versus wake age.

Figure 31. Tip vortex location versus RWF with and without fuselage predictions for $\mu = 0.15$ and $\psi_b = 0°$.

(a) From above.
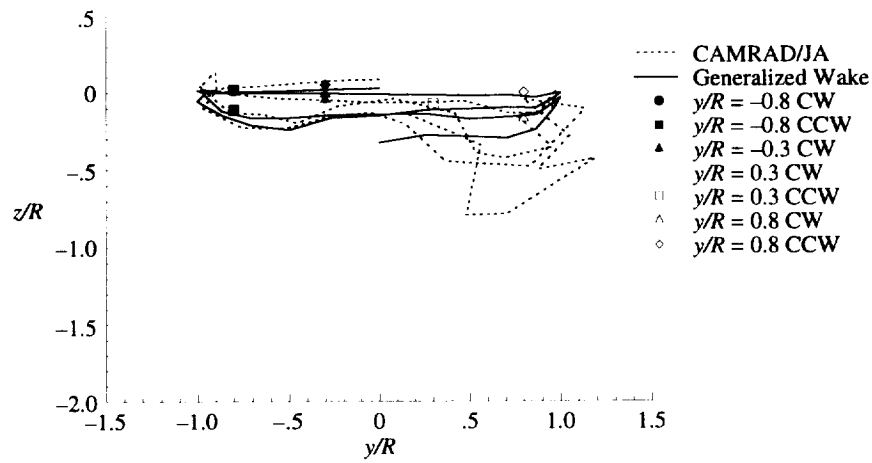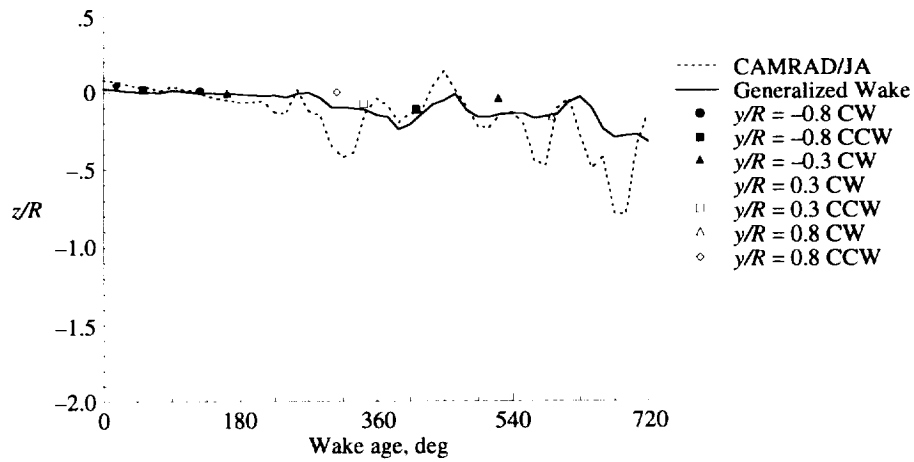


(b) From behind.



(c) Height of single vortex filament versus wake age.

Figure 32. Tip vortex location versus CAMRAD/JA and Generalized Wake predictions for $\mu = 0.23$ and $\psi_b = 0°$.
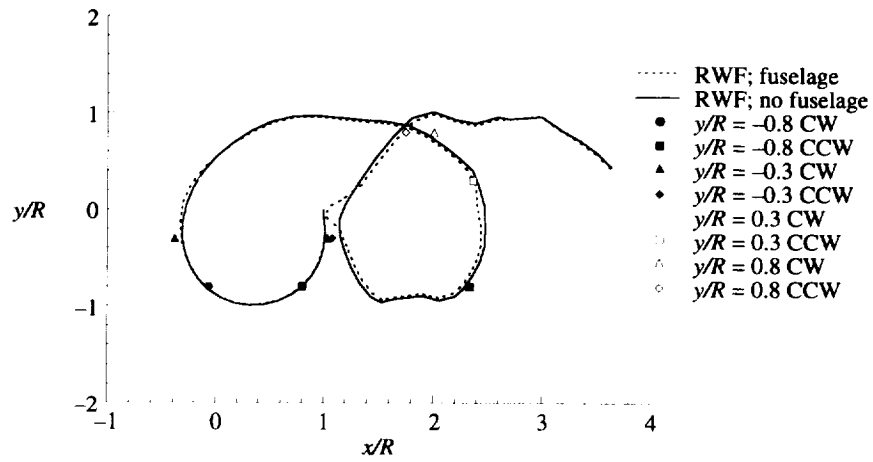
(a) From above.
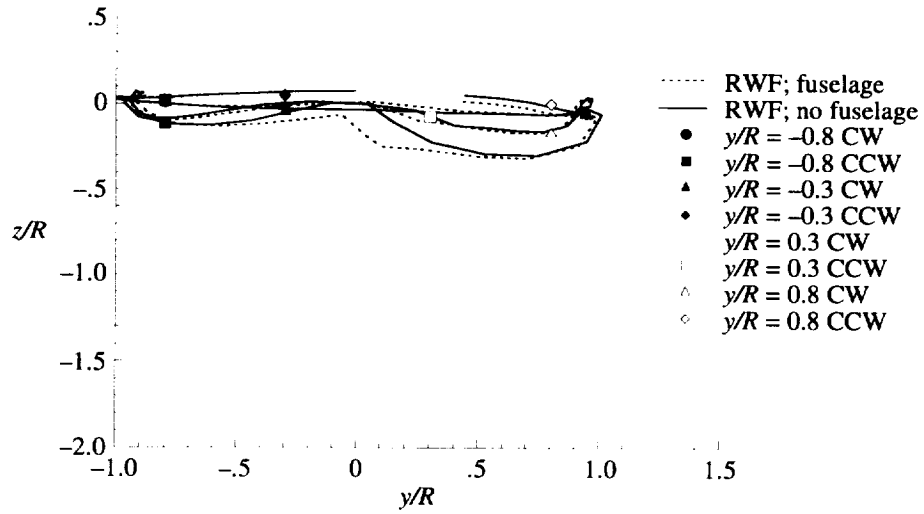


(b) From behind.
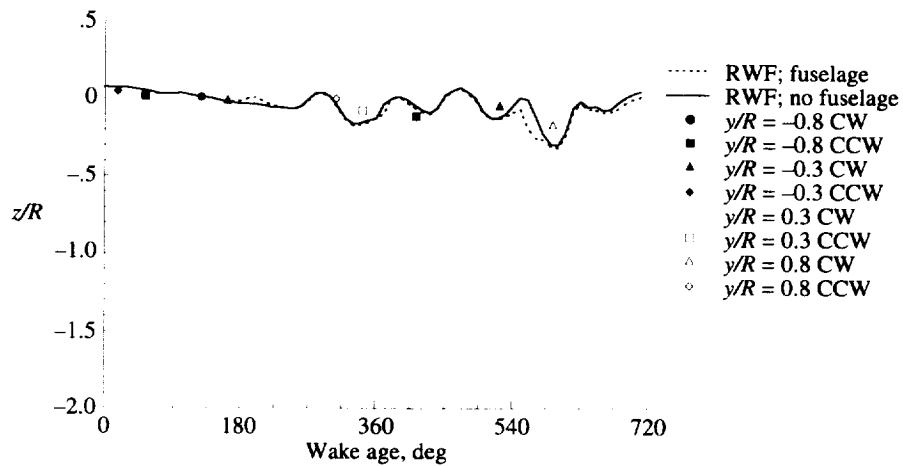


(c) Height of single vortex filament versus wake age.

Figure 33. Tip vortex location versus RWF with and without fuselage predictions for $\mu = 0.23$ and $\psi_b = 0°$.
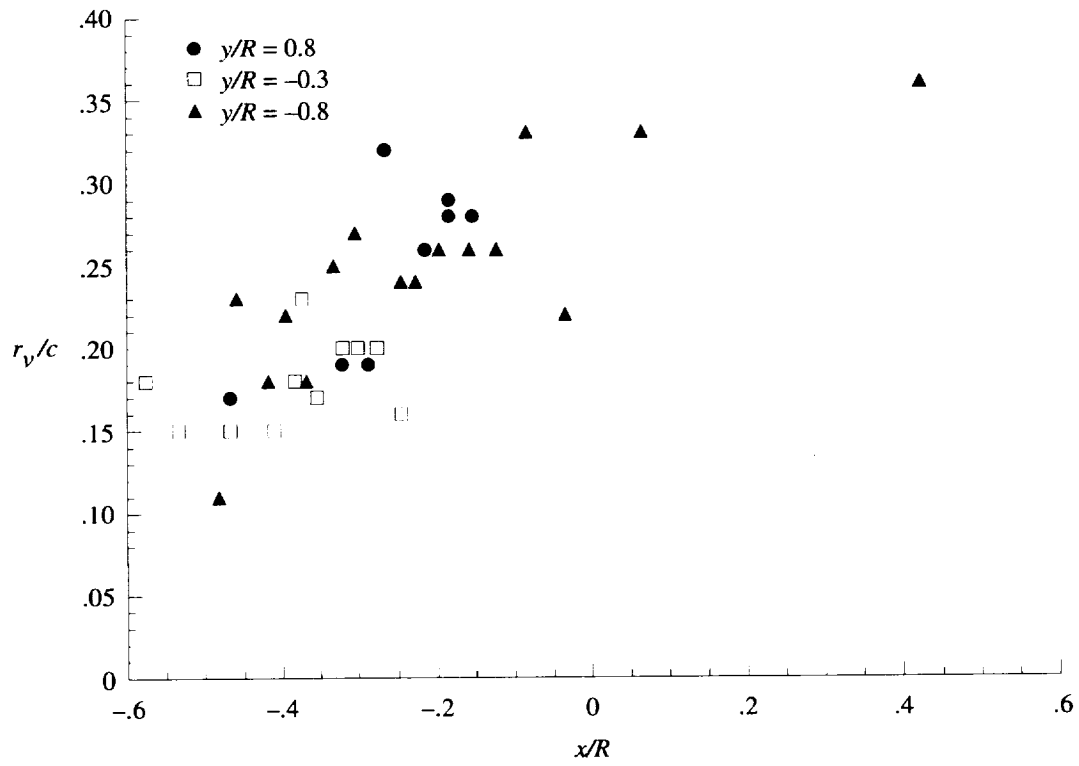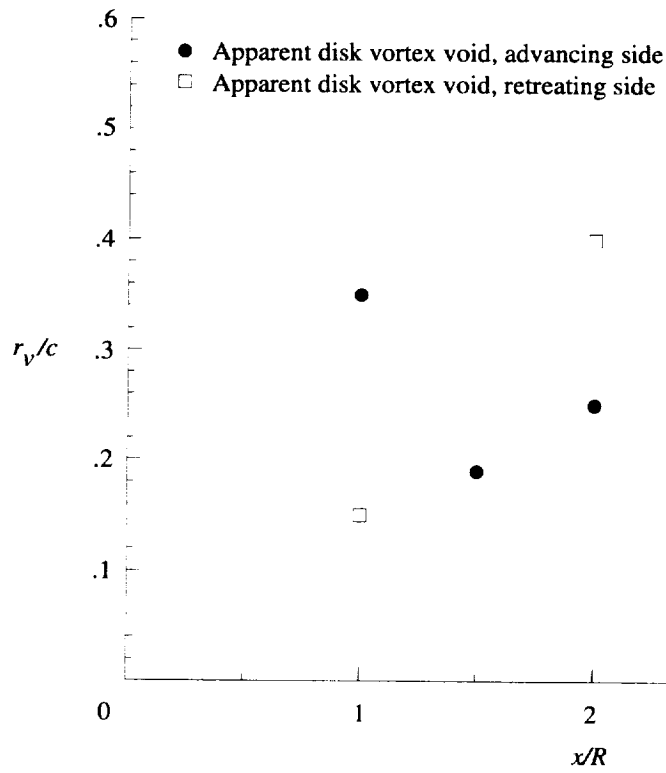
(a) $\mu = 0.15$.
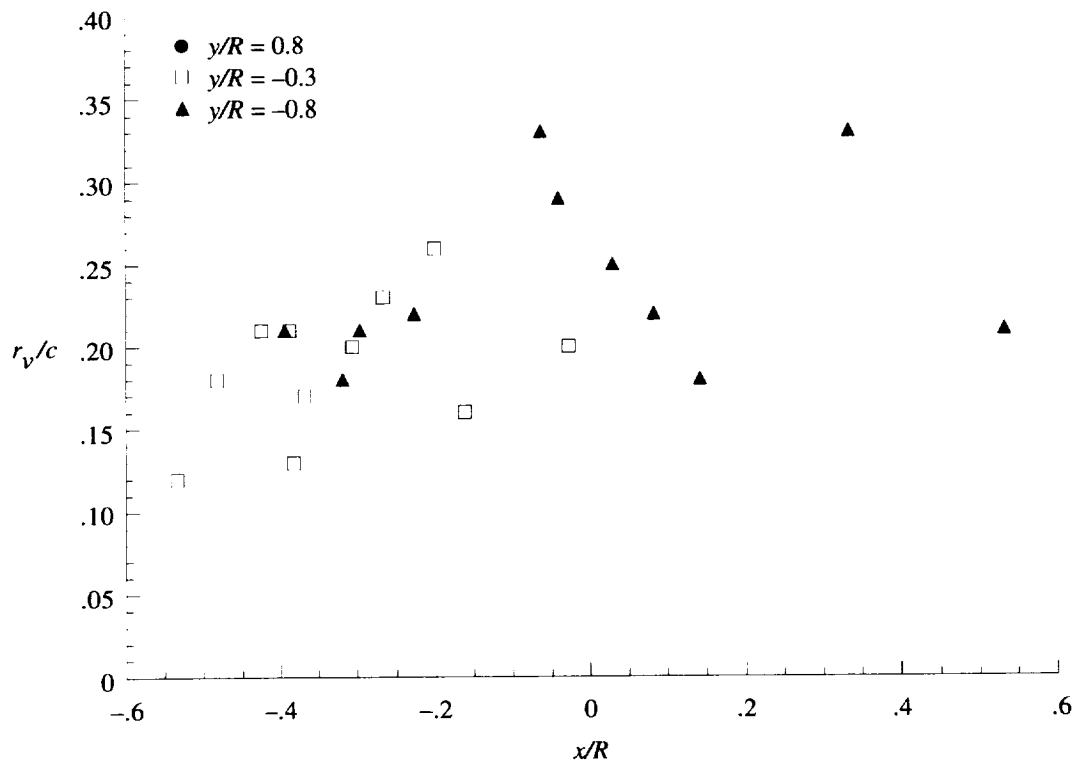


(b) $\mu = 0.23$

Figure 34. Tip vortex particle void size.
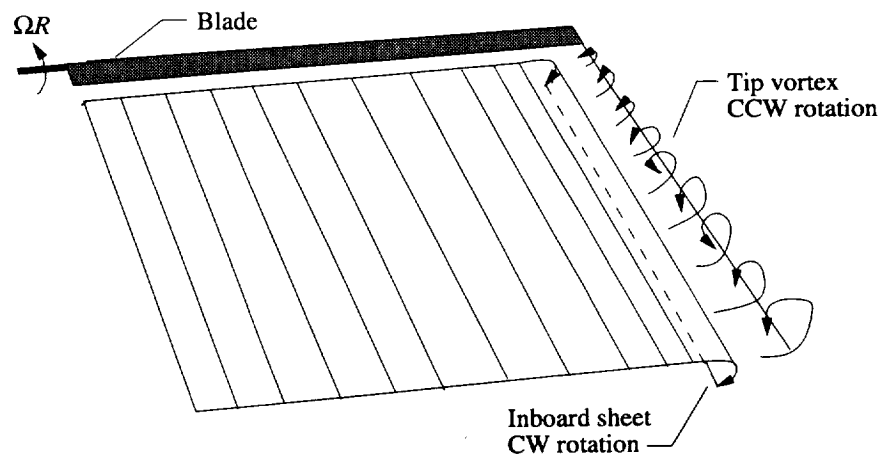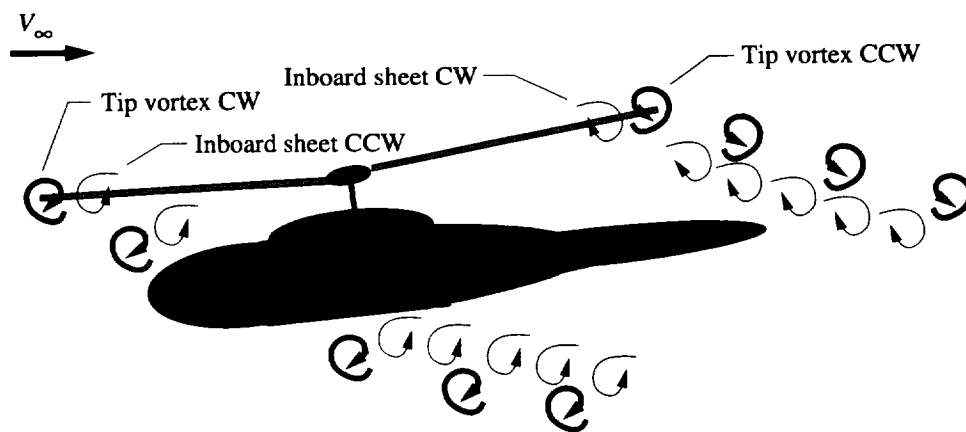
(a) μ = 0.15.
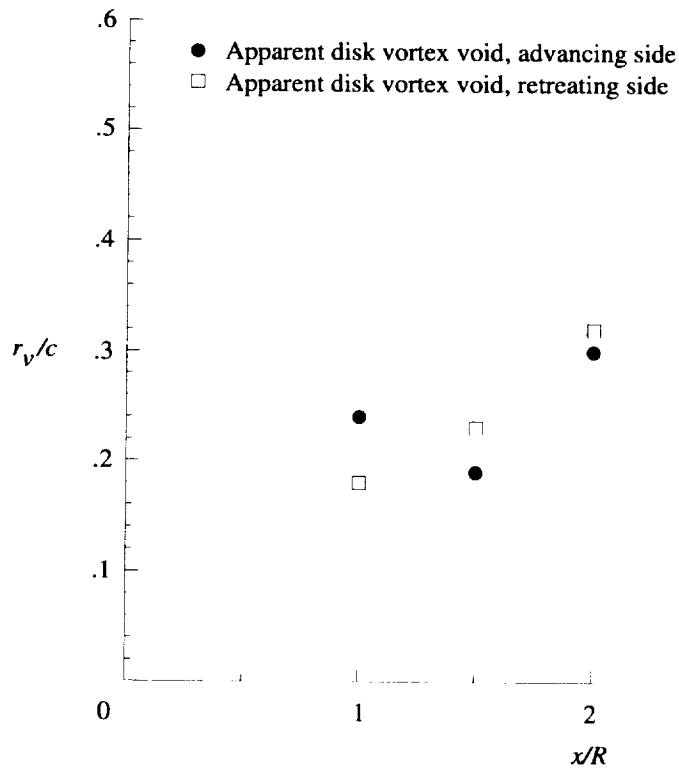


(b) μ = 0.23

Figure 35. Apparent disk vortex particle void size.

(a) Simplified depiction of inboard sheet roll-up.



(b) Tip vortex and inboard sheet vortex orientation.

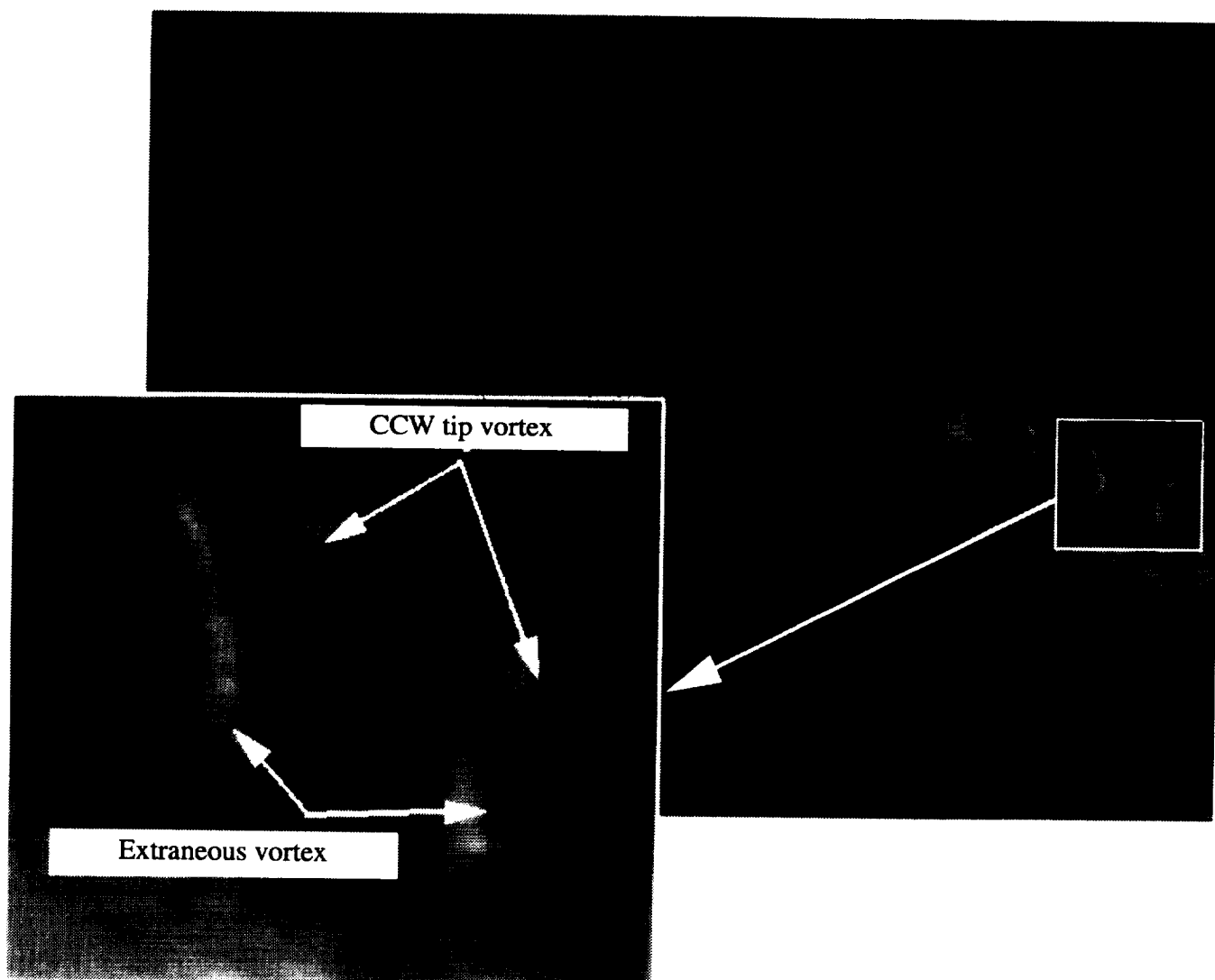Figure 36. Tip vortices and inboard sheet roll-up.

Figure 37. Roll-up of outer edge of trailing vortex sheet. $y/R = 0.3$; $\mu = 0.15$.
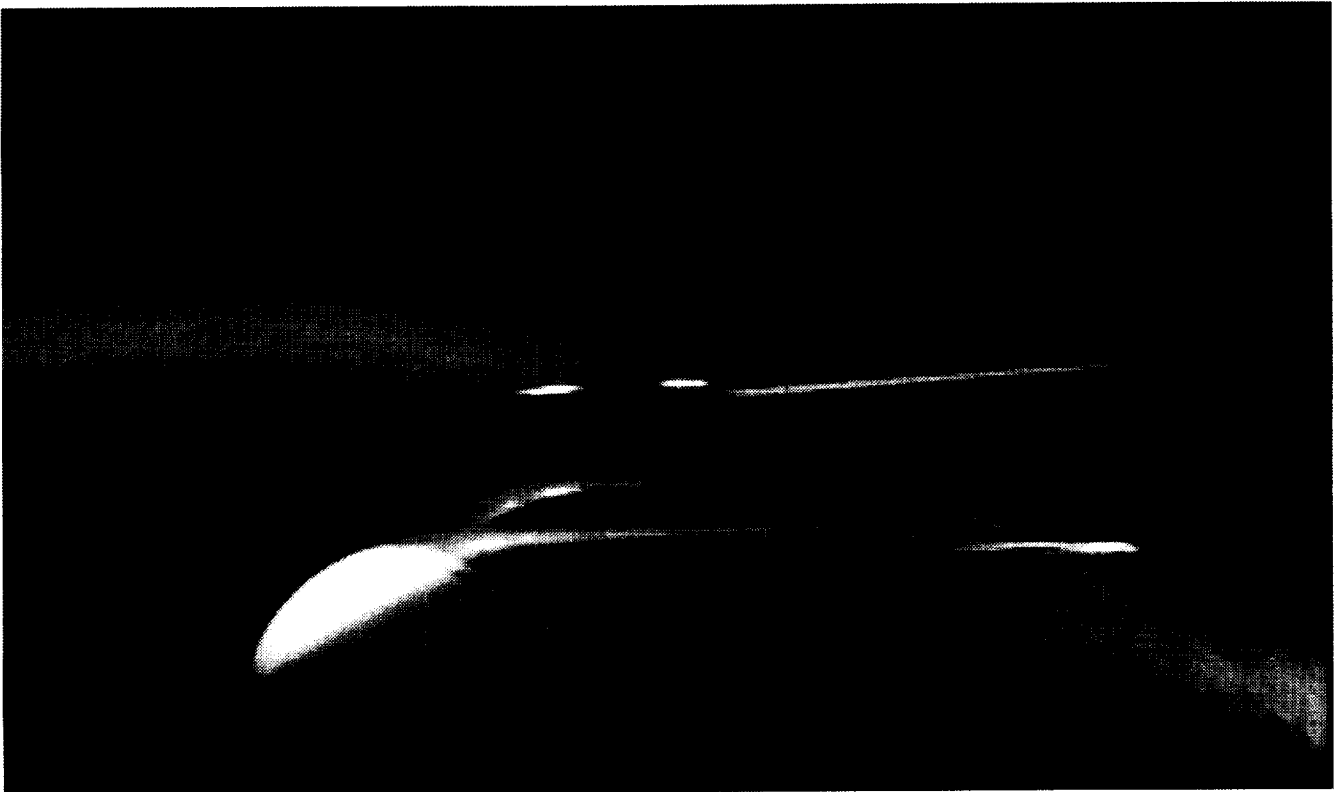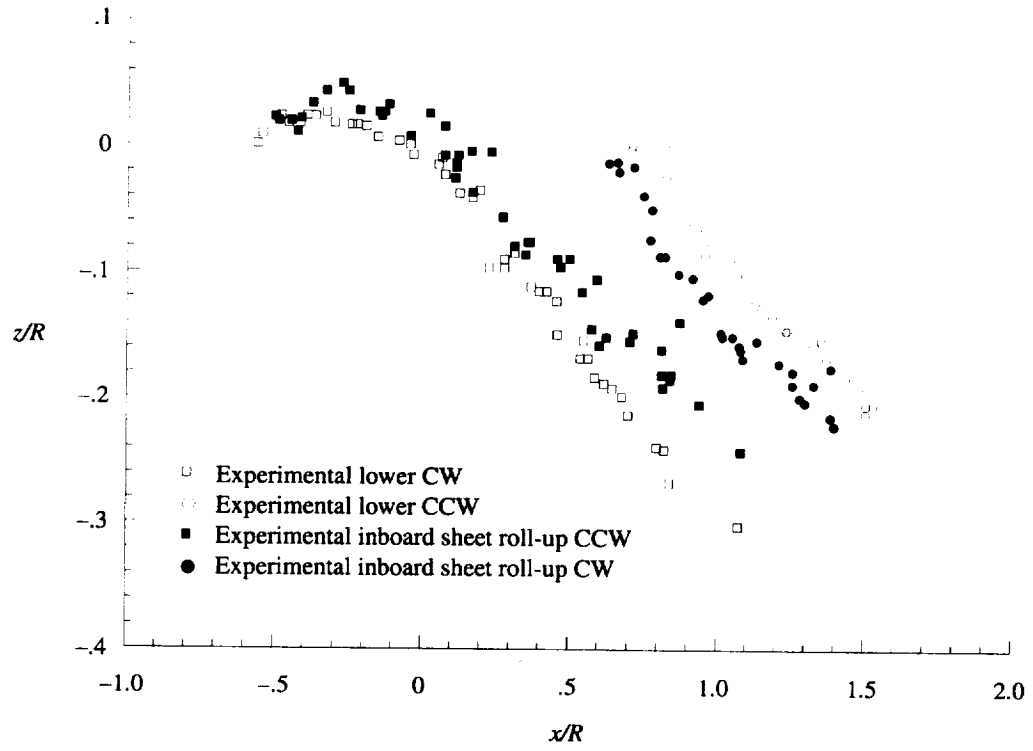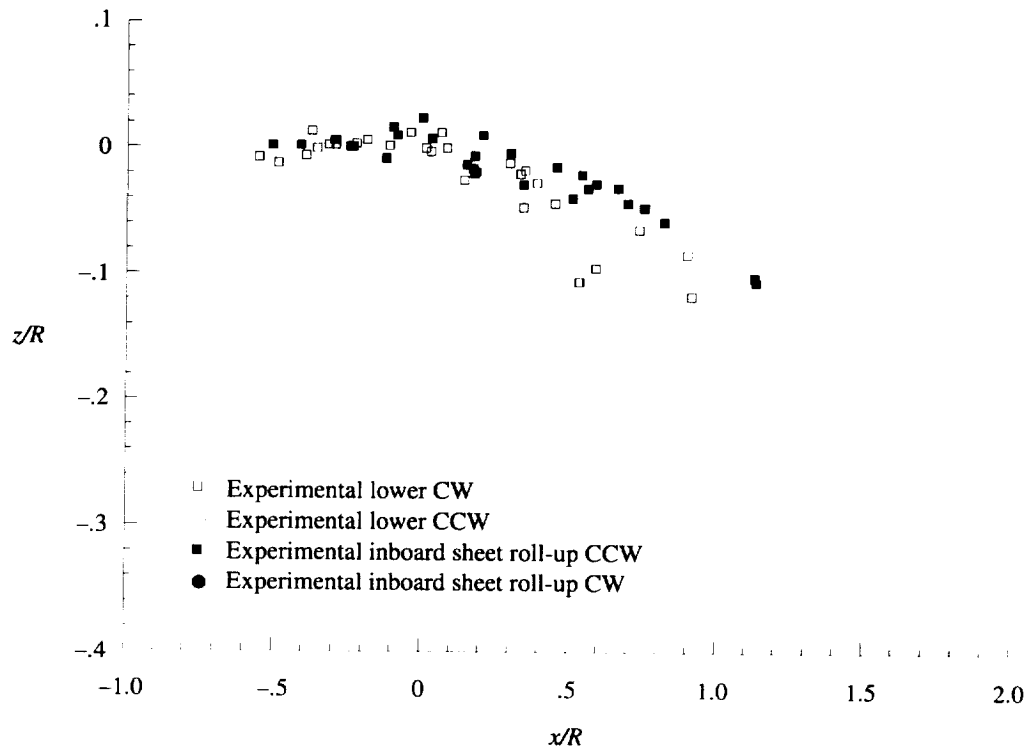
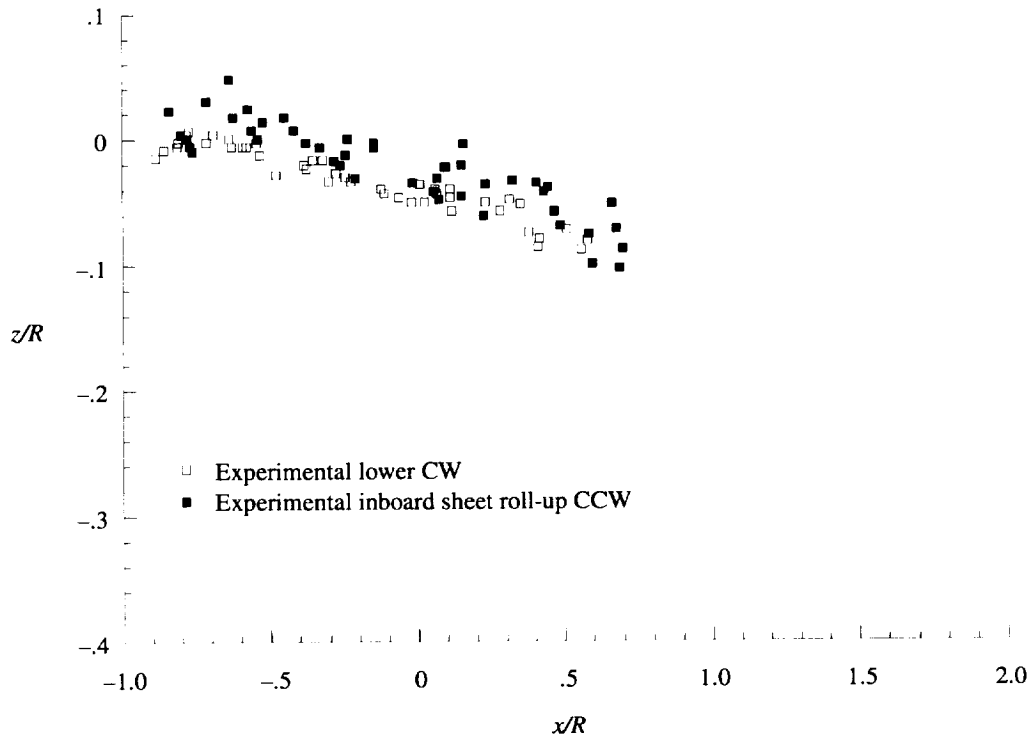Figure 38. The 2MRTS in wind tunnel with lights on. $y/R = 0.3$; $\mu = 0.15$.
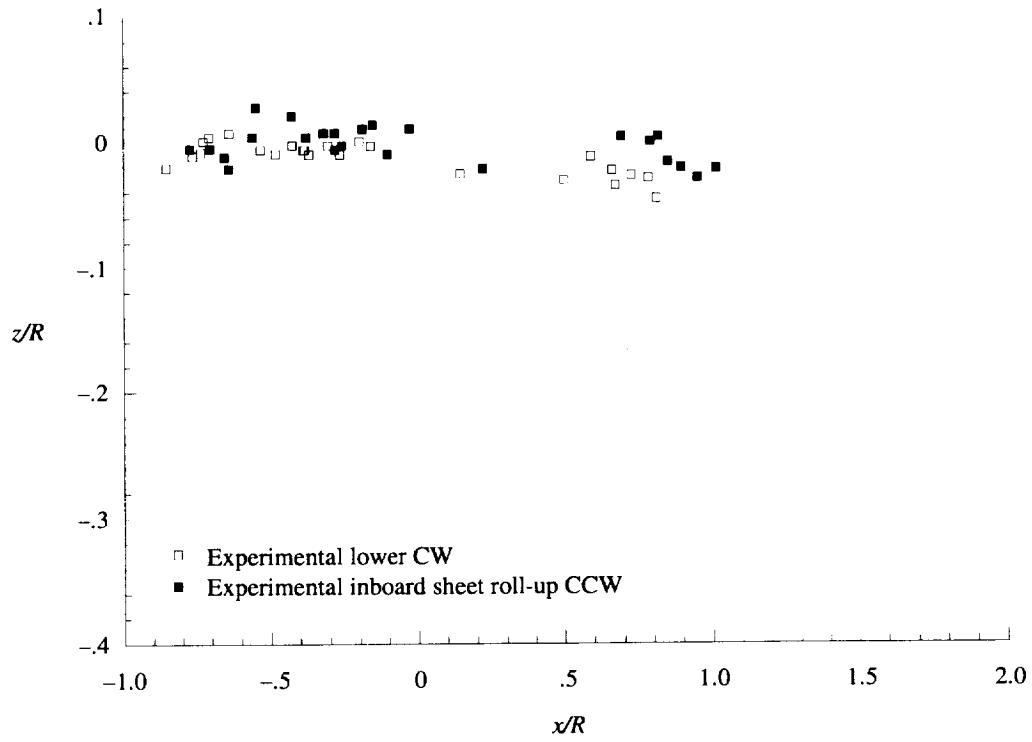
(a) μ = 0.15.



(b) μ = 0.23.

Figure 39. Quantified roll-up of outer edge of trailing vortex sheet at $y/R = -0.8$.

(a) $\mu = 0.15$.



(b) $\mu = 0.23$.

Figure 40. Quantified roll-up of outer edge of trailing vortex sheet at $y/R = -0.3$.

$$r_1 = \frac{\left(\frac{x}{R}\right)_{\text{tip vortex}} - \left(\frac{x}{R}\right)_{\text{ISV}}}{\cos \phi}$$

$(x/R)_{\text{tip vortex}}$

$(x/R)_{\text{ISV}}$

Rotor hub

Laser light sheet

$\phi$

$r_1$

Top view

$$r = \frac{\left(\frac{x}{R}\right)_{\text{tip vortex}} - \left(\frac{x}{R}\right)_{\text{ISV}}}{\cos \theta \cos \phi}$$

$r_1$

$\theta$

$r$

$\theta = a_0 + \alpha_s$

Side view

Rotor hub

(a) Difference between tip vortex and ISV locations.

$$r = \left[\left(\frac{x}{R}\right)_{\text{ISV}}^2 - \left(\frac{y}{R}\right)_{\text{light sheet}}^2\right]^{0.5}$$

Rotor hub

$r$

$(y/R)_{\text{light sheet}}$

$(x/R)_{\text{ISV}}$

(b) ISV $x/R$ location.
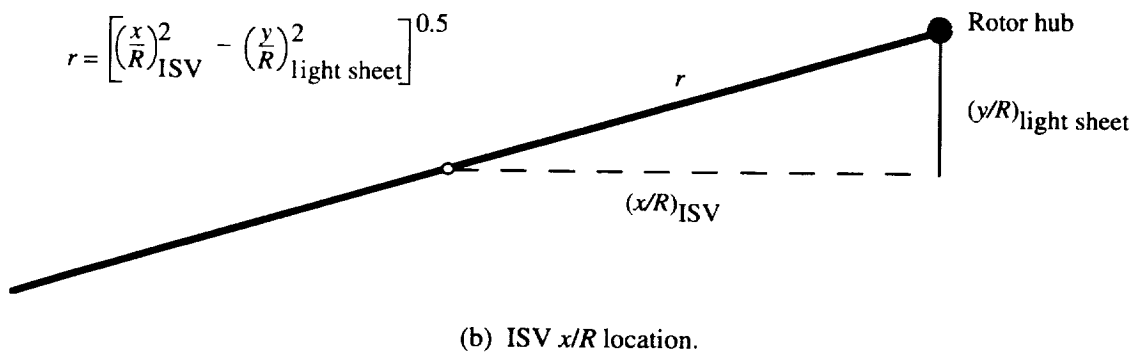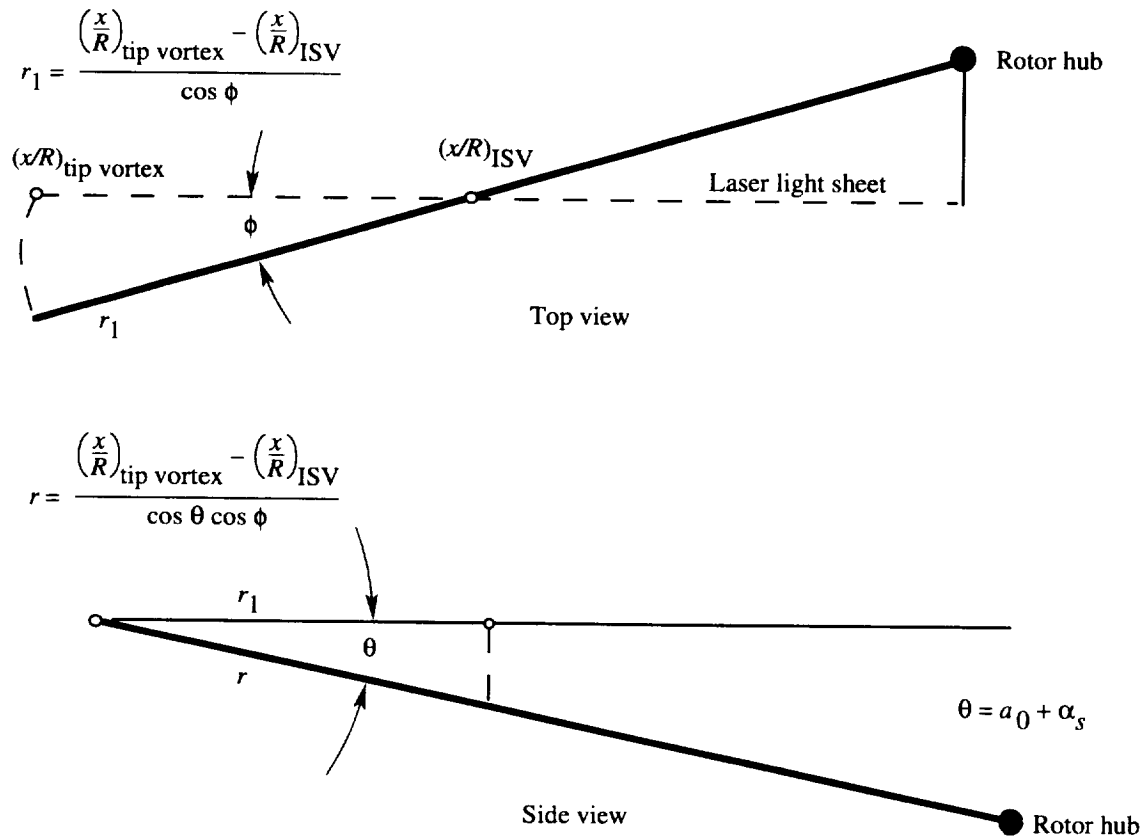
Figure 41. Methods to determine location of ISV formation.

62

# REPORT DOCUMENTATION PAGE

Public reporting burden for this collection of information is estimated to average 1 hour per response, including the time for reviewing instructions, searching existing data sources, gathering and maintaining the data needed, and completing and reviewing the collection of information. Send comments regarding this burden estimate or any other aspect of this collection of information, including suggestions for reducing this burden, to Washington Headquarters Services, Directorate for Information Operations and Reports, 1215 Jefferson Davis Highway, Suite 1204, Arlington, VA 22202-4302, and to the Office of Management and Budget, Paperwork Reduction Project (0704-0188), Washington, DC 20503.

| 1. AGENCY USE ONLY (Leave blank) | 2. REPORT DATE<br>August 1996 | 3. REPORT TYPE AND DATES COVERED<br>Technical Paper |
|---|---|---|

**4. TITLE AND SUBTITLE**
Wake Geometry Measurements and Analytical Calculations on a Small-Scale Rotor Model

**5. FUNDING NUMBERS**
WU 505-59-39-01

PR 1L162211A47A

**6. AUTHOR(S)**
Terence A. Ghee, John D. Berry, Laith A. J. Zori, and Joe W. Elliott

**7. PERFORMING ORGANIZATION NAME(S) AND ADDRESS(ES)**
NASA Langley Research Center
Hampton, VA 23681-0001

Joint Research Program Office
Aeroflightdynamics Directorate
U.S. Army Aviation and Troop Command
NASA Langley Research Center
Hampton, VA 23681-0001

**8. PERFORMING ORGANIZATION REPORT NUMBER**
L-17449

**9. SPONSORING/MONITORING AGENCY NAME(S) AND ADDRESS(ES)**
National Aeronautics and Space Administration
Washington, DC 20546-0001
and
U.S. Army Aviation and Troop Command
St. Louis, MO 63120-1798

**10. SPONSORING/MONITORING AGENCY REPORT NUMBER**
NASA TP-3584

ATCOM TR-96-A-007

**11. SUPPLEMENTARY NOTES**
Ghee: Analytical Services & Materials, Inc., Hampton, VA; Berry and Elliott: JRPO, Aeroflightdynamics Director-ate, ATCOM, Langley Research Center, Hampton, VA; Zori: Iowa State University, Ames IA.
Research supported by NASA under Contract NAS1-19831 and Grant NAG1-1267.

**12a. DISTRIBUTION/AVAILABILITY STATEMENT**

Unclassified–Unlimited
Subject Category 05
Availability: NASA CASI (301) 621-0390

**12b. DISTRIBUTION CODE**

**13. ABSTRACT** (Maximum 200 words)
An experimental investigation was conducted in the Langley 14- by 22-Foot Subsonic Tunnel to quantify the rotor wake behind a scale model helicopter rotor in forward level flight at one thrust level. The rotor system in this test consisted of a four-bladed fully articulated hub with blades of rectangular planform and an NACA 0012 airfoil sec-tion. A laser light sheet, seeded with propylene glycol smoke, was used to visualize the vortex geometry in the flow in planes parallel and perpendicular to the free-stream flow. Quantitative measurements of wake geometric proper-ties, such as vortex location, vertical skew angle, and vortex particle void radius, were obtained as well as convec-tive velocities for blade tip vortices. Comparisons were made between experimental data and four computational method predictions of experimental tip vortex locations, vortex vertical skew angles, and wake geometries. The results of these comparisons highlight difficulties of accurate wake geometry predictions.

**14. SUBJECT TERMS**
Rotor; Wake; Vortex; Flow visualization; Helicopter; Laser; Light sheet; Wind tunnel

**15. NUMBER OF PAGES**
63

**16. PRICE CODE**
A04

| 17. SECURITY CLASSIFICATION OF REPORT<br>Unclassified | 18. SECURITY CLASSIFICATION OF THIS PAGE<br>Unclassified | 19. SECURITY CLASSIFICATION OF ABSTRACT<br>Unclassified | 20. LIMITATION OF ABSTRACT |
|---|---|---|---|

NSN 7540-01-280-5500